Coupled Ocean/Sea-Ice Modelling in the Southern Ocean

by

Simon J. Marsland, B.Sc.(Hons)
(Simon James)

Submitted in fulfilment of the requirements
for the degree of
Doctor of Philosophy

University of Tasmania, July, 1999

Declaration

This thesis contains no material which has been accepted for a degree or diploma by the University of Tasmania or any other institution. To the best of my knowledge this thesis contains no material previously published or written by another person except where due acknowledgment is made in the text of the thesis.

.....

Authority of Access

This thesis may be made available for loan and limited copying in accordance with the *Copyright Act 1968.*

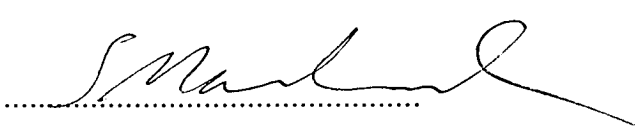

.....

Abstract

The ocean/sea-ice interaction in the Southern Ocean is investigated using the Hamburg Ocean Primitive Equation Model (HOPE). The ocean model is three dimensional and prognostically calculates velocity, temperature, salinity and sea-surface elevation on a multi-level staggered Arakawa E-grid. Coupled to this is a thermodynamic model of sea-ice growth and melt, and a dynamic model with viscous-plastic rheology. Two versions have been formulated: a high-resolution re-entrant channel model of the East Antarctic coastline; and a medium-resolution southern hemisphere model.

In the high-resolution model the mean annual oceanic heat flux (OHF) to the sea-ice (8 W m^{-2}) is dominated by convection. There is considerable seasonal variability in the OHF, with areal-averaged values approaching 20 W m^{-2} in winter, and falling below 5 W m^{-2} in summer. There is also considerable spatial variability in the OHF: near the sea-ice edge mean monthly values can be above 100 W m^{-2}; within a coastal polynya, where the maximum annual *in situ* sea-ice growth is 15 m, values approach 50 W m^{-2}; in the seasonal zone (62–64°S) an OHF in the range 5–20 W m^{-2} is common in the winter months; but for most of the year at most other locations the oceanic heat flux lies in the range of 0–5 W m^{-2}. Sensitivities to the magnitudes of sea-ice salinity and precipitation minus evaporation (P–E) are investigated. The model is found to be very sensitive to processes that affect the sea surface salinity, which determines the vertical stability of the ocean. In turn this controls the rate of convection, and consequently the sea-ice thickness. For the extreme case of zero P–E the model enters into a mode of temperature-driven deep convection, characterised by relatively warm sea surface temperature and a total collapse of the seasonal sea-ice cycle.

The medium-resolution version is used to investigate the response of the coupled ocean/sea-ice system to a number of surface fresh water flux

(SFWF) climatologies, and to changes in the mean surface air temperature in the southern hemisphere. As with the high-resolution model the sea-ice is very sensitive to the SFWF. In particular, the occurrence of a large scale polynya in the Weddell Sea is found to depend critically on there being a sufficient SFWF. The mean annual OHF for the Southern Ocean is found to be around 25 W m^{-2}, also with considerable seasonal and spatial variability. Increasing the SFWF by 10 cm a^{-1} results in a decrease of 10% in the OHF, while increasing the surface air temperature by 2°C increases the OHF by 10%. The increase in surface air temperature results in a decrease in mean annual sea-ice extent and volume of around 20%, while the increase in SFWF results in an increase in mean annual sea-ice extent of around 5%, and an increase in mean annual sea-ice thickness of around 12%.

Acknowledgments

This thesis was supported by a scholarship from the Antarctic CRC, funded from the Dedicated Greenhouse Research Grants Scheme of the National Greenhouse Advisory Committee. I would like to thank Dr Jörg-Olaf Wolff and Prof. Bill Budd for the excellent supervision that they have provided throughout the course of my candidature as a research higher degree student, and for the many conversations that aided in the progress of this work. I would like to thank the two anonymous examiners for their many helpful comments and suggested revisions that improved the thesis. I would also like to thank Dr Xingren Wu and Mr Phil Reid for provision of the atmospheric forcing fields from the CSIRO 9 model, Mr Phil Reid for the GASP and ECMWF precipitation and evaporation data, Dr Nathan Bindoff for the bathymetry and thermohaline initialization used in the Southern Ocean Sector Model, and Dr Rob Massom for the SSM/I data. Finally I thank my partner Elizabeth and daughter Madeleine for their patience, love and support.

CONTENTS

LIST OF TABLES

LIST OF FIGURES

1. INTRODUCTION

1.1 The Southern Ocean in Global Climate

In this study the focus is upon the interactions between ocean and sea-ice in the Southern Ocean. The seasonal sea-ice cover that advances and retreats around the coastline of Antarctica each year has a significant impact on the global climate system, through its moderation of the exchanges of heat, fresh water, and momentum between the ocean and atmosphere systems. Sea-ice is both an important climate indicator and a sensitive component of the climate system (Gordon, 1988). Our knowledge of sea-ice distribution and seasonality in the Southern Ocean has increased dramatically over the past 25 years due to the introduction of satellite-based observing systems (Zwally *et al.*, 1979; Gloerson *et al.*, 1992). The same cannot be said for sea-ice thickness or the oceanic thermohaline state in the seasonal sea-ice zone, of which only limited observations that are sparse in both space and time are available.

Sea-ice is involved in a number of important feedbacks with the climate state of the ocean and atmosphere. The high albedo of sea-ice significantly alters the surface radiation balance. This results in a positive feedback between the atmosphere and the sea-ice, whereby sea-ice growth cools the atmosphere and enhances further sea-ice growth as shown by one-dimensional energy-balance models (Budyko, 1969; Sellers, 1969). On the other hand brine rejection via the sea-ice formation process tends to create a negative feedback with the ocean (Martinson, 1990). As the density of the surface

water is increased the vertical stability of the ocean is decreased, which enhances mixing via convection. Since the ocean at depth is warmer than the freezing temperature such mixing tends to increase the oceanic heat flux to the base of the sea-ice which inhibits further sea-ice growth, and may result in sea-ice melt.

It has been known for some time that the seasonal sea-ice cover in the Southern Ocean exists in a delicate balance with the underlying waters, and can exhibit two distinct climatic modes (Gordon, 1991). In the 'stable mode' sea-ice formation is supported by the presence of a relatively thin surface mixed layer which is generally cooler and fresher than the waters below. The stability of the upper ocean is intimately related to the amount of sea-ice growth. Too much sea-ice growth, or too little fresh water input to the upper ocean, can lead to a situation where the mixed layer salinity approaches the deep water salinity. This causes continual deep convection which results in a near uniform vertical ocean temperature and salinity column. The surface water in such a 'thermal mode' system is too warm for sea-ice formation to occur. As it cools the vertical instability is enhanced, producing further convection. The oceanic heat is released as sensible and latent heat flux across the open ocean surface, and the net ocean/atmosphere heat exchange is an order of magnitude greater than in the 'stable mode'.

In recent years there has been a growing concern about human influence on the global climate, and a key question is how the earth's climate may be expected to change in the near future (IPCC, 1996). To answer such a question requires an understanding of the interactions between the various climate processes on a variety of time scales. A significant relationship exists between the Southern Ocean and the global oceanic thermohaline circulation. The water mass exchange and bottom water formation that occurs there is believed to be a major contributor to the ventilation of the global deep ocean (Deacon, 1937; Gill, 1973; Carmack, 1986). The major basins of the world ocean are only linked at depth through the Southern Ocean,

and thus the strong Antarctic Circumpolar Current (ACC) is important for the transport and mixing of properties between these basins (Gordon, 1986; Broecker, 1987). The zonal nature of the ACC acts to isolate the cold surface waters to the south from the much warmer surface waters to the north (Gordon, 1988). North-south transport across the ACC is limited to deep boundary currents supported by submarine ridges and mesoscale eddy fluxes within the ACC (Bryden, 1983).

In the absence of a spatially and temporally coherent observational data set, one way of attempting to isolate the relative importance of the various physical processes active (e. g. the role of sea-ice) is to use modelling. Due to the analytical complexity of the non-linear physical equations involved, the current state of the art in ocean simulation (as with climate prediction in general) is based on numerical approximation. Oceanic general circulation models (OGCMs) are complex, computationally intensive and in a continual state of development and improvement. They are constructed using a spatially discrete three-dimensional mesh of grid points at which model variables are defined. A model is then forward integrated from one time step to the next. When polar regions are considered, the addition of a sea-ice model greatly improves the representation of the surface boundary conditions in OGCMs. This also allows for the physical feedbacks between the ocean and sea-ice to occur within the model.

1.2 Primitive Equation Ocean Models

It should be noted that a variety of numerical formulations have been used to study the circulation of the ocean. Quasi-geostrophic models have been used to study the wind-driven barotropic circulation (Veronis, 1966a,b), in early eddy resolving baroclinic studies (Holland and Lin, 1975a,b), and in studies of the dynamical balance of the Antarctic Circumpolar Current

(McWilliams *et al.*, 1978; McWilliams and Chow, 1981; Wolff *et al.*, 1991). The Hamburg Large-Scale-Geostrophic model (LSG) (Hasselmann, 1982) has been used to study the equilibrium state of the global thermohaline circulation (Mikolajewicz and Maier-Reimer, 1990; Maier-Reimer *et al.*, 1993), and in studies of anthropogenically induced climate change (Cubasch *et al.*, 1992, 1994; Santer et al., 1994). An isopycnal coordinate model (OPYC) that solves the oceanic primitive equations has been constructed by Oberhuber (1993a,b) and used to study ENSO variability (Lunkeit *et al.*, 1996) and climate change (Hasselmann *et al.*, 1995). Here attention is restricted to the more widely used primitive equation models with fixed vertical coordinates. Development of such a model (Bryan, 1969) led to the first simulation of the global ocean with realistic bottom topography by Bryan and Cox (1972). A lack of computer power led to an interest in regional studies of the Indian Ocean (Cox, 1970), the Southern Ocean (Gill and Bryan, 1971), and the North Atlantic (Holland and Hirschman, 1972). Semtner (1974) introduced realistic bottom topography and the use of far more efficient vectorized computer code.

Advances in computing led to the use of coarse-resolution primitive equation global models (typically with a 5° horizontal resolution) by the late 1970's. Bryan and Lewis (1979) were able to run a model to equilibrium (~1000 years) under a seasonal surface climatology to investigate the role of the ocean in poleward transport of heat. Washington *et al.* (1980) coupled a coarse-resolution ocean model to a global atmosphere model, but found that the thermohaline characteristics of the modelled ocean drifted considerably with respect to the current state. A more realistic simulation of the global ocean was achieved by using the decoupled ocean model from the Washington *et al.* (1980) study with observed mean monthly atmospheric forcing. This was carried out by Meehl *et al.* (1982) who found the ocean heat transport to be most sensitive to the parameterisation of horizontal heat and salt diffusivity, and to the magnitude and seasonality of the surface wind stress.

A key problem with the coarse-resolution ocean models is the parameterisation of sub-grid scale processes. Early eddy resolving primitive equation ocean models were able to simulate oceanic synoptic scale activity for the gulf stream in the mid-latitudes of the North Atlantic Ocean (Robinson *et al.*, 1977; Semtner and Mintz, 1977). With the advance in supercomputing technology it was possible by the late 1980's for regional and even global studies at high-resolution. The Fine Resolution Antarctic Model Group (FRAM, 1991) developed a $\frac{1}{4}^\circ$ latitude by $\frac{1}{2}^\circ$ longitude model of the Southern Ocean south of 25°S. The U.S./German Community Modeling Effort (CME) used a $\frac{1}{3}^\circ$ resolution model to study the circulation of the North Atlantic (Bryan and Holland, 1989; Böning *et al.*, 1991). Global studies were performed by Semtner and Chervin (1988, 1992) with a $\frac{1}{2}^\circ$ resolution model that extended to 75°S. Although results showed a rich eddy structure in many parts of the world ocean, these models were only marginally eddy resolving at high latitudes. More recently the Semtner and Chervin model has been integrated at $\frac{1}{6}^\circ$ resolution for the global ocean (Semtner, 1994) and the U.K. Ocean Circulation and Climate Advanced Modelling Project (OCCAM) Global Ocean Model has been run on a $\frac{1}{4}^\circ$ grid (Webb *et al.*, 1998), with plans for a $\frac{1}{8}^\circ$ version using massively parallel computing architecture. None of these high-resolution studies has as yet included a sea-ice model.

1.3 Sea-Ice Models

The first model to solve a full surface energy balance determining the evolution of sea-ice thickness was that of Maykut and Untersteiner (1971). It was a sophisticated one-dimensional model having 40 layers, and included heating effects due to solar penetration into the sea-ice slab and the insulating effects of a snow cover. The use of high vertical resolution was found to be largely unnecessary by Semtner (1976a). He found that three

layers were sufficient to reproduce the thermodynamic effects on sea-ice growth and melt, where the vertical resolution changed in time so that one grid point is centred within the snow layer, and two are evenly distributed within the sea-ice. He also proposed a much simpler *zero-layer* model with sea-ice thickness, snow thickness and surface temperature being the only prognostic variables. The zero-layer model was found to overestimate sea-ice thickness in the growth period and underestimate it during the melt season, while being reasonably accurate in determination of mean annual sea-ice thickness in the Arctic (Semtner, 1984). Semtner (1976a) also suggested that the sea-ice model should include the effects of open water within the sea-ice pack through a parameterisation of leads. The basic idea is to perform separate heat balance equations for open water and for sea-ice at each grid cell, and then use the sum weighted by the fraction of open water to determine the actual thermodynamic heat exchange. A zero-layer version with leads parameterisation was found to improve the seasonal cycle of sea-ice extent in the thermodynamic model of Washington *et al.* (1976). The parameterisation was improved by Parkinson and Washington (1979) by allowing ocean heat storage within the leads and by reducing the lateral melting of sea-ice in their thermodynamic/dynamic global sea-ice model.

Considerable attention has been given to the role of snow in the thermodynamics of sea-ice growth and melt, and the effects of snow on sea-ice in the climate system (e. g. Ledley, 1991; 1993). Snow has two important effects on the thermodynamic balance: it has a significantly lower thermal conductivity and so tends to insulate the sea-ice from the cold air above which leads to less sea-ice growth (Maykut, 1986); and it also has a higher albedo than sea-ice which results in reduced or delayed summer melt (Ledley, 1991). Snow salinisation due to flooding also plays a role in the sea surface salinity and sea-ice mass balances (e. g. Ackley *et al.*, 1990; Eicken *et al.*, 1994; Massom *et al.*, 1997). Fichefet and Morales Maqueda (1997a,b) used a sophisticated thermodynamic/dynamic sea-ice model coupled to a

one-dimensional mixed-layer/pycnocline ocean model to examine the sensitivity of sea-ice in both the Arctic and Southern Oceans to the inclusion of a snow layer and to the inclusion of snow-ice formation due to flooding. They show that the sensitivity is far greater in the Antarctic pack, where sea-ice is much thinner. Here a reduction of 50% in the snow accumulation rate leads to an almost complete cutoff of snow-ice formation, while an increase of 50% results in a large increase in sea-ice volume due to additional flooding.

Sea-ice dynamics alter the local mass budget of sea-ice through convergence and divergence. In turn this alters the ocean's surface fresh water and salt fluxes over time. Hence a realistic model of ocean/sea-ice interaction should include a representation of the dynamic component of sea-ice evolution. Sea-ice momentum is a resultant of both external and internal forcing. The balance of external forcing is limited to air and ocean stresses, a Coriolis term and the pressure gradient associated with ocean surface tilt. Closure of the momentum balance requires some knowledge of the internal sea-ice dynamics. The simplest approach is the free-drift model, which assumes no sea-ice/sea-ice interaction. Under free-drift sea-ice will move to the right of the mean wind direction in the Northern Hemisphere, and to the left of the mean wind direction in the Southern Hemisphere due to the presence of the Coriolis term in the momentum balance. The free-drift sea-ice velocity is linearly related to the wind velocity (Hibler and Flato, 1992). Thorndike and Colony (1982) show that around 70% of the variance in sea-ice velocity in the central Arctic can be explained by variations in the local geostrophic winds. The remainder must be accounted for by time-dependent variations in the ocean currents or internal sea-ice dynamics.

The Arctic Ice Dynamics Joint Experiment (Maykut *et al.*, 1972; Untersteiner, 1980) from 1970 to 1977 attempted direct observation of the many physical parameters affecting sea-ice. The parallel modelling study (Coon, 1980) used an elastic-plastic representation of the stress-strain re-

lationship. In the plastic rheology sea ice deformation is independent of time. That is, formation of ridges and leads is instantaneous given an internal sea-ice stress state corresponding to convergence and divergence respectively. This is in contrast to the elastic and viscous rheologies where the deformation of sea-ice is time dependent. The time (or rate) dependence is defined by a linear relationship between stress and strain for the elastic rheology, and by a linear relationship between stress and strain rate for the viscous rheology. The elastic-plastic rheology has no resistance to divergence (i.e. plastic), will exhibit elastic deformation for small negative stress states (weak convergence), and has infinite resistance for large negative stress states (strong convergence). For convergence a limiting value defines the boundary in stress/strain space between elastic and plastic behaviour, and is a parameter of the formulation. The elastic-plastic rheology is complicated both analytically (Pritchard, 1975) and numerically (Colony and Pritchard, 1975). The use of a viscous-plastic rheology for internal sea-ice behaviour was introduced by Hibler (1979) and has been used in many studies since (e. g. Hibler and Ackley, 1983; Hibler and Bryan, 1987; Lemke *et al.*, 1990; Stössel, 1997). In the viscous-plastic case sea-ice acts as a linear viscous fluid for small deformations, be they divergent or convergent. Above some cutoff strain rate the sea-ice stress state becomes infinitely resistant to both convergence and divergence.

A number of alternative sea-ice rheological formulations have been constructed. The cavitating fluid rheology of Flato and Hibler (1992) defines sea-ice to have no resistance to dilation or shearing but infinite resistance to compression. This rheology has the advantage of being computationally simple but will only produce a realistic sea-ice cover for simulations at coarse horizontal resolution with time-averaged forcing due to the absence of a shear term (Flato and Hibler, 1992). Ip *et al.* (1991) compare elliptic, square, cavitating fluid and Mohr-Coulomb formulations of plastic sea-ice rheology in simulations of the Arctic basin. The Mohr-Coulomb rheology

is similar to the cavitating fluid but includes a shear term via a nonlinear shear viscosity. The square and elliptic rheologies are named for the shape of the curve in two-dimensional stress space that defines the limiting value above which plastic deformation occurs. They find that the elliptic and square rheologies lead to similar results, as do the cavitating fluid and Mohr-Coulomb formulations. They conclude that choice of rheology is more important in determining sea-ice drift (velocity) than sea-ice thickness, and that the cavitating fluid and Mohr-Coulomb rheologies lead to excessive sea-ice drift when compared to both the other rheologies and to drifting buoy data.

1.4 Coupled Ocean/Sea-Ice Models

Sea-ice forms when the ocean surface freezes and in so doing has a considerable effect on the thermohaline structure of the ocean itself. It is therefore natural to use coupled ocean/sea-ice models as a means of investigating the complex interactions and possible feedbacks that may exist in the coupled system. One-dimensional studies including the addition of a pycnocline have been carried out for the Southern Ocean (Lemke, 1987) and the Arctic Ocean (Lemke and Manley, 1984; Fichefet and Gasper, 1988; Mellor and Kantha, 1989). The Lemke model has also been applied to the Weddell Sea (Lemke *et al.*, 1990; Owens and Lemke, 1990) using the Cartesian grid of Hibler and Ackley (1983) and the dynamic/thermodynamic sea-ice model of Hibler (1979). Stössel *et al.* (1990) extended this model to the entire Southern Ocean from 50-80°S using a spherical grid with latitudinal and longitudinal grid spacings of 2.5° and 5° respectively. That model used mean monthly atmospheric forcing and was able to reproduce the large-scale features of Antarctic sea-ice. More recently Fichefet and Morales Maqueda (1997a) have applied the model of Fichefet and Gasper (1988) with improved sea-ice thermodynamics and the inclusion of sea-ice dynamics to the

world ocean. This model has been used for the study of sensitivity of sea-ice in the Southern Ocean to the inclusion of a snow layer and to the inclusion of a snow-ice formation scheme.

The first study to use a full three-dimensional primitive equation ocean model coupled to a sea-ice model was that of Semtner (1976b). The model simulated circulation and interaction in the Arctic Ocean but did not include the dynamics of sea-ice motion. Similar models (also without sea-ice dynamics) were applied globally at coarse-resolution in transient climate change studies (Manabe and Stouffer, 1980; Washington *et al.*, 1980) and in parameter studies (e. g. Meehl *et al.*, 1982). It was found that the high magnitude of the coefficient of horizontal diffusivity required for these coarse resolution simulations led to unrealistic sea surface temperatures and the models generally performed poorly in reproducing the observed cycle of sea-ice advance and retreat, especially in the Southern Hemisphere. The first fully coupled ocean/sea-ice models to include sea-ice dynamics were those of Hibler and Bryan (1987) and Semtner (1987). These models were regional in extent, incorporating the Arctic Ocean, the Greenland Sea, and the Norwegian Sea. One finding was that the coupled system displayed complex interactions in the seasonal and marginal sea-ice zones. It was noted that a delicate balance exists there between the induced convection through brine rejection during sea-ice formation and the stabilising influence of fresh water input during sea-ice melt (Hibler and Bryan, 1987). The Arctic sea-ice was also found to be sensitive to global warming, with a 2°C increase in air temperatures leading to a total melt of Arctic sea-ice in summer (Semtner, 1987).

It is only in the last few years that the sophistication of a full three-dimensional primitive equation ocean model with a thermodynamic/dynamic sea-ice component has been applied to studies of the Southern Ocean. The model of Häkkinen (1995), using a generalised viscous rheology (Häkkinen, 1987; Häkkinen and Mellor, 1992), required the addition of 45 cm yr^{-1}

of fresh water on top of the average net precipitation minus evaporation (P-E) of 60 cm yr^{-1} to balance the salt flux at the open northern boundary. There it is pointed out that the P-E is a poorly known quantity for the Southern Ocean and that there is considerable uncertainty about the fresh water fluxes, including glacial contribution from the Antarctic ice cap. That model also demonstrated the large spatial variability in the annually averaged oceanic heat flux with values ranging from 0-100 W m^{-2}. Gordon and O'Farrell (1997) used the cavitating fluid rheology (Flato and Hibler, 1992) in studies of transient climate change with the CSIRO global coupled atmosphere/ocean/sea-ice model, and noted that the "cold-start" problem (Hasselmann *et al.*, 1993) in that model could be avoided by a longer integration commencing much earlier in the anthropogenic CO_2 build up.

More recently a number of studies have been carried out with the more realistic Hibler (1979) viscous-plastic rheology using the Hamburg Ocean Primitive Equation Model (HOPE) (Drijfhout *et al.*, 1996; Stössel, 1997; Legutke *et al.*, 1997; Stössel *et al.*, 1998). Drijfhout *et al.* (1996) attributed a 20 year oscillation in the thermohaline circulation of their global model to a coupled density and sea-ice thickness anomaly propagating westward around the coast of Antarctica. Stössel (1997) demonstrates that the treatment of sea-ice in the model has a considerable effect on the oceanic thermohaline circulation by considering three sensitivity simulations under mean monthly climatological surface forcing: neglecting brine release during sea-ice formation greatly reduces the Southern Ocean meridional overturning cell; removal of the sea surface salinity enhancement along the Antarctic coastline also reduces the overturning cell; and the inclusion of new-ice thickness growth in partially ice-covered grid cells increases the strength of the meridional cell. The idea of salinity enhancement (e.g. Cox, 1989) was used by England (1992, 1993) to improve the simulation of Antarctic bottom water (AABW) formation in a model that had no sea-ice, and should not be necessary in higher resolution models with sea-ice that resolve

the coastal processes responsible for AABW formation. The Stössel (1997) model was coarse resolution (3.5°) and hence there is some justification for the inclusion of salinity enhancement.

A similar study by Legutke *et al.* (1997) used daily atmospheric model surface forcing on a 2.8° model grid at mid and high latitudes. They also included an improved thermodynamic sea-ice component (Owens and Lemke, 1990; Stössel, 1992; Wolff *et al.*, 1997), with a prognostic snow model and a full heat balance equation for ice-free and ice-covered areas within each model grid cell. In the Southern Hemisphere of that model the sea-ice was too thin compared with observations, the sea-ice minimum extent was too small and large permanent polynyas persisted in the Weddell and Ross seas. All of these effects were attributed to the large oceanic heat flux dominated by the convective adjustment scheme and induced by brine rejection. They performed a number of sea surface salinity (SSS) sensitivity experiments and concluded that both the sea-ice cover and the strength and variability of the ACC are very sensitive to treatment of SSS. Stössel *et al.* (1998) have extended this line of research using mean monthly climatological forcing where the length of the integrations has been increased by an order of magnitude over the Legutke *et al.* (1997) simulations which allows the ocean to achieve quasi-equilibrium. They consider three sets of sensitivity experiments: the first focuses on the effects of the low salinity of sea-ice through the inclusion of brine release or SSS enhancement; the second looks more closely at the role of the sea-ice thermodynamic formulation and investigates the effect of a prognostic snow cover; and the third examines the system response to daily wind fluctuations. All three categories of sensitivity analysis are found to have significant long term impact on the thermohaline characteristics of the global ocean through their effects on both AABW formation and the strength of the Southern Ocean overturning cell.

1.5 Discussion

It is generally accepted that the coupled ocean/sea-ice system in the Southern Ocean is an important component of the global climate system (e. g. Gordon, 1988; van Ypersele, 1990; Budd, 1991; Olbers, 1993; Goosse *et al.*, 1997). The sea-ice exists in a delicate balance with the underlying ocean waters. Interactions and feedbacks involving sea-ice formation, brine rejection, mixed layer stability, deep convection, vertical mixing, oceanic heat flux, and sea-ice melt all play a part in determining the evolution of sea-ice thickness and compactness (Martinson and Iannuzzi, 1998). Consideration of sea-ice dynamics adds to the complexity of the system. Near surface oceanic convergence and divergence leads to sources and sinks in the surface fresh water budget, which in turn impacts on the thermohaline circulation. Currently the role of sea-ice transport associated with the underlying mesoscale oceanic fluctuations is only poorly understood.

Two types of polynya are known to occur in the Southern Ocean, namely convection-driven open ocean polynyas and wind-driven coastal latent heat polynyas (Gordon and Comiso, 1988). The coastal latent heat polynyas are quite common (Cavalieri and Martin, 1985) and their geometry and extent reasonably well understood by simple model studies of wind strength and coastline orientation (Pease, 1987; Darby *et al.*, 1995). Such polynyas are believed to be areas of large sea-ice growth and subsequently areas of large salt flux to the ocean (Cavalieri and Martin, 1985; Zwally *et al.*, 1985; Markus *et al.*, 1998). However they are not resolved by the coarse-resolution coupled ocean/sea-ice models and due to their inaccessibility have not been subjected to many *in situ* observations. One advantage of the use of high horizontal resolution in numerical modelling is the ability to resolve such small scale features. The best example of a large-scale open ocean polynya in the Southern Ocean is that of the Weddell Polynya observed in the early 1970's (Gordon, 1978; Killworth, 1979). In addition a smaller

recurring open ocean polynya has been observed in the Cosmonaut Sea (Comiso and Gordon, 1987). The deep oceanic convection that is believed to be responsible for such polynyas is an important term in the global ocean climate, helping to maintain the stable stratification of the world ocean through the creation of dense bottom waters (Killworth, 1983).

The computational capability of modern supercomputers is rising by an order of magnitude each decade (Semtner and Chervin, 1989). A result of this will be an ability to model global coupled ocean/sea-ice/atmosphere models at increasingly higher resolutions. Combined with this is the rapid growth in observational data available concerning the weather and climate state in the high southern latitudes, particularly via satellite observation. In order to prepare for this exciting new age of knowledge concerning the global climate system it is necessary first to gain an understanding of the various components of that system (Dickinson *et al.*, 1996; Gates *et al.*, 1996). The Southern Ocean coupled ocean/sea-ice system is currently one of the least well understood components of the global climate system (Gordon, 1998), yet it is known that a correct treatment of sea-ice is essential in simulations of transient change in the global climate system (e. g. Meehl and Washington, 1990; Manabe *et al.*, 1992; Rind *et al.*, 1995).

1.6 Aims of this Thesis

In this thesis use is made of the HOPE coupled ocean/sea-ice model (Wolff *et al.*, 1997), with the following aims:

1. Develop a regional high-resolution coupled ocean/sea-ice model for use in the Southern Ocean.

2. Use this model to calculate the magnitude and seasonality of oceanic heat flux beneath a seasonal sea-ice cover.

3. Examine the sensitivity of the modelled ocean/sea-ice system to changes in horizontal resolution and sea-ice model formulation.

4. Develop a medium-resolution full Southern Ocean version for comparison with the high-resolution study.

5. Investigate the sensitivity of both models to the surface fresh water flux.

6. Compare the sensitivity of sea-ice to the surface fresh water flux with the sensitivity of sea-ice to the surface air temperature in the Southern Ocean.

1.7 Overview of this Thesis

Chapter 2 describes the components of the coupled model used in this study. An ocean primitive equation model is coupled to a viscous-plastic sea-ice dynamic model, along with a thermodynamic model of sea-ice growth and melt. The ocean model uses finite differencing to forward integrate equations governing momentum balance of the ocean's three-dimensional velocity field, conservation of temperature and salinity, and evolution of the free surface elevation. The sea-ice dynamic model consists of a momentum balance which is closed by assuming a viscous-plastic rheology for internal sea-ice stress, along with equations for continuity of sea-ice thickness and compactness. The thermodynamic sea-ice model calculates sea-ice growth and melt rates according to fluxes of latent and sensible heat, incoming and outgoing longwave radiation, and incoming shortwave radiation modified by surface reflectivity (albedo), and includes the insulating effects of snow accumulation. The ocean model provides a time and space variable oceanic heat flux which causes melting of sea-ice from below.

The coupled model has been applied at high-resolution to a region of the

South-East Indian Basin of the Southern Ocean, along the East Antarctic coastline. Section 3.1 describes the formulation of the model as a re-entrant (periodic) channel with artificially closed northern boundary. The availability of mean monthly surface forcing data sets from the CSIRO 9 level coupled atmosphere/sea-ice/ocean model (Gordon and O'Farrell, 1997), although coarse in horizontal resolution (R21 spectral truncation), allows for the modelling of the basic physical processes governing ocean/sea-ice interaction and seasonality. The behaviour of the ocean and sea-ice models for a 60 year reference simulation is examined in Sections 3.2 and 3.3 respectively. In Section 3.4 the magnitude, seasonality, and spatial variablity of the oceanic heat flux to the base of the sea-ice is determined, along with the relative importance of convective, diffusive and advective oceanic processes in providing this heat.

A variety of sensitivities of the high-resolution coupled ocean/sea-ice model are investigated in Chapter 4. The reference simulation is repeated with a doubling of horizontal resolution in Section 4.1. A number of variations in the sea-ice model formulation are investigated in Section 4.2. The sensitivity of the model to the magnitude of a constant surface fresh water flux is considered in Section 4.3. It turns out that a sufficient fresh water flux at the surface is necessary for maintaining mixed layer stability. In the absence of a sufficient surface fresh water flux, the relatively low salinity of the mixed layer increases due to the brine rejection associated with sea-ice formation. This results in enhanced deep convection and a corresponding rise in ocean surface temperatures. The formation of a seasonal sea-ice cover is greatly reduced in this scenario. On the other hand if the surface fresh water flux is very high then the model evolves towards an increasingly stable state in which sea-ice formation does not induce deep (sub-mixed-layer) convection and the deep water becomes cut off from atmospheric processes.

In Chapter 5 a full Southern Hemisphere coupled ocean/sea-ice model known as the Southern Ocean Sector Model is introduced. Section 5.1

describes the telescoped grid of the model which has a fine-resolution sector that includes the region of interest in the model of Chapters 3 and 4 and a medium-resolution elsewhere in the Southern Ocean. Sensitivity of the sea-ice distribution to a variety of applied surface fresh water flux scenarios is investigated in Section 5.3. It is demonstrated that the region of most marginal stability in the Southern Ocean coupled ocean/sea-ice system is in the Weddell Sea. There a large scale polynya forms for two of the three precipitation minus evaporation climatologies considered. The occurrence of the large scale polynya is dramatically reduced when a contribution from glacial meltwater is included in the prescribed surface fresh water flux, and so it is postulated that an anomalously low precipitation rate in the vicinity of Maud Rise combined with the pre-existing weak vertical stratification in this region is sufficient to explain the observed Weddell Polynya in the early 1970's. The sensitivity of the model to changes in surface air temperature is investigated in Section 5.4, and it is found that both a cooling and a warming of the surface air temperature can result in enhancement of the polynya activity in the Weddell Sea.

For convenience and reference the full set of simulations discussed in this thesis is set out in Tables 1.1 and 1.2.

East Antarctic Model Experiments			
Name	Years	Description	Section
REF	00-60	Reference	3.1–3.4
VHR	00-49	Double horizontal resolution	4.1
ND	50-60	No sea-ice dynamics	4.2
NS	50-60	No snow model	4.2
NS2I	50-60	No snow-ice conversion	4.2
S10	50-60	S_{ice} = 10 psu	4.2
S15	50-60	S_{ice} = 15 psu	4.2
S20	50-60	S_{ice} = 20 psu	4.2
S25	50-60	S_{ice} = 25 psu	4.2
S30	50-60	S_{ice} = 30 psu	4.2
P0	50-90	P–E = 0 cm a^{-1}	4.3
P25	50-90	P–E = 25 cm a^{-1}	4.3
P50	50-60	P–E = 50 cm a^{-1}	4.3
P75	50-60	P–E = 75 cm a^{-1}	4.3
P100	50-60	P–E = 100 cm a^{-1}	4.3

Tab. 1.1: Simulations with the high-resolution East Antarctic Model that are discussed in this thesis. P–E refers to the precipitation minus evaporation and S_{ice} to the salinity of sea-ice. All of the sensitivity experiments were initialised at Year 50 of the reference simulation (REF). Details are given in the section indicated.

Southern Hemisphere Model Experiments			
Name	P–E	T_{air}	Section
C9	CSIRO 9		5.2
GA	GASP		5.3
EC	ECMWF		5.3
C9P10	CSIRO 9 + 10 cm a^{-1}		5.3
GAP10	GASP + 10 cm a^{-1}		5.3
ECP10	ECMWF + 10 cm a^{-1}		5.3
ECM20	ECMWF – 20 cm a^{-1}		5.3
ECM10	ECMWF – 10 cm a^{-1}		5.3
ECP20	ECMWF + 20 cm a^{-1}		5.3
ECP30	ECMWF + 30 cm a^{-1}		5.3
ECM2	ECMWF	– 2°C	5.4
ECP2	ECMWF	+ 2°C	5.4
ECP10M2	ECMWF + 10 cm a^{-1}	– 2°C	5.4
ECP10P2	ECMWF + 10 cm a^{-1}	+ 2°C	5.4

Tab. 1.2: Simulations with the Southern Ocean Sector Model that are discussed in this thesis. P–E refers to the precipitation minus evaporation climatology used and T_{air} to the surface air temperature. All simulations were initialised from rest and integrated for 5 model years. Details are given in the section indicated.

2. THE HOPE COUPLED OCEAN/SEA-ICE MODEL

2.1 Primitive Equation Ocean Model

The ocean model used in this study is based on the Hamburg Ocean Primitive Equation model (hereafter HOPE). HOPE was developed by E. Maier-Reimer at the Max Planck Institute for Meteorology in Hamburg, Germany. HOPE is an Ocean General Circulation Model (OGCM), based on forward integration of the so called 'primitive equations'. It is a multi-level finite difference formulation on an Arakawa E-grid (Arakawa and Lamb, 1977). The model features a free surface and variable bottom depth within each grid cell. The HOPE model is described in some detail elsewhere (Wolff *et al.*, 1997). It solves a system of physical equations that govern the evolution of ocean circulation, subject to atmospheric forcing at the surface. The main equations are a nonlinear momentum balance equation for horizontal velocities, conservation and diffusivity equations for potential temperature and salinity, and the linearised kinematic boundary condition for sea surface elevation. The hydrostatic and Boussinesq approximations are assumed to be valid.

2.1.1 Ocean Model Equations

The horizontal momentum balance equation is:

$$\frac{d\vec{v}_o}{dt} + f(\vec{k} \times \vec{v}_o) = -\frac{1}{\rho_0}\left[\vec{\nabla}_H(p + \rho_0 g\zeta)\right] + \vec{F}_H + \vec{F}_V \tag{2.1}$$

where $\vec{v}_o = (u_o, v_o)$ is the oceanic horizontal velocity vector in spherical coordinates, t is the time, f the Coriolis parameter, $\vec{k}$ a unit vector directed away from the earth's centre, ρ_0 a constant reference density, $\vec{\nabla}_H$ the horizontal gradient operator, p the internal pressure, g is gravity and ζ is the sea surface elevation. The total derivative is given by $\frac{d}{dt} = \frac{\partial}{\partial t} + \vec{v}_o \cdot \vec{\nabla}_H + w_o \cdot \frac{\partial}{\partial z}$, with w_o being the vertical component of ocean velocity, and $\frac{\partial}{\partial z}$ the vertical partial derivative. Horizontal viscosity, $\vec{F}_H$, is parameterised as the sum of harmonic (Laplacian) and biharmonic terms.

$$\vec{F}_H = A_H \vec{\nabla}_H^2 \vec{v}_o - B_H \vec{\nabla}_H^4 \vec{v}_o \tag{2.2}$$

Here A_H and B_H are constant coefficients, $\vec{\nabla}_H^2 = \vec{\nabla}_H \cdot \vec{\nabla}_H$ is the horizontal Laplacian operator, and $\vec{\nabla}_H^4 = \vec{\nabla}_H^2 \cdot \vec{\nabla}_H^2$ is the horizontal biharmonic operator. Vertical eddy viscosity is parameterised as

$$\vec{F}_V = A_V \frac{\partial}{\partial z}\left(\frac{\partial}{\partial z}\vec{v}_o\right) \tag{2.3}$$

where the eddy coefficient A_V is constant.

Diagnostic treatment of pressure and density is used to close the momentum balance. Density, ρ, is taken to be a function of model pressure, temperature and salinity according to the equation of state polynomial defined by the Joint Panel on Oceanographic Tables and Standards (UNESCO, 1981). Potential temperatures are converted to *in situ* temperatures for the density calculation. The pressure is calculated using the hydrostatic equation.

$$\frac{\partial p}{\partial z} = -g\rho \tag{2.4}$$

Forward integration of the ocean model surface elevation is based on a linearised kinematic boundary condition, which states that the time rate

of change of surface elevation is equal to the vertical component of oceanic velocity at the surface.

$$\frac{\partial \zeta}{\partial t} = w_o|_{z=0} \tag{2.5}$$

The vertical velocity is calculated from the horizontal velocity field using the incompressibility condition

$$\frac{\partial w_o}{\partial z} = -\vec{\nabla}_H \vec{v}_o \tag{2.6}$$

Integrating over the entire depth then gives the vertical velocity at the sea surface

$$w_o|_{z=0} = -\vec{\nabla}_H \int_{-H}^{0} \vec{v}_o \, dz \tag{2.7}$$

Potential temperature, Θ, and salinity, S, obey the continuity equations

$$\frac{d\Theta}{dt} = D_V \frac{\partial}{\partial z}\left(\frac{\partial \Theta}{\partial z}\right) + D_H \vec{\nabla}_H^2 \Theta \tag{2.8}$$

$$\frac{dS}{dt} = D_V \frac{\partial}{\partial z}\left(\frac{\partial S}{\partial z}\right) + D_H \vec{\nabla}_H^2 S \tag{2.9}$$

The horizontal and vertical diffusivity coefficients, D_H and D_V, are assumed to be constant, and $\vec{\nabla}_H^2$ is the horizontal Laplacian.

2.1.2 Finite Difference Grid

The HOPE model is formulated on an Arakawa E-grid, (Arakawa and Lamb, 1977), as shown in Figure 2.1. In this spatial discretisation vector variables are defined at the corners and centre of a grid square, with scalar quantities defined at the mid-points of the sides. The effective grid spacing is shown as D, and is the distance between like points. The model grid is split into two horizontally staggered sub-grids allowing for more efficient usage of available vector computing hardware in the solution of equations. Alternate rows along lines of equal latitude are denoted as 'odd' and 'even' and form the two sub-grids. The resulting horizontal model grid is shown in Figure 2.2. The ocean model is further discretised over a number of vertical

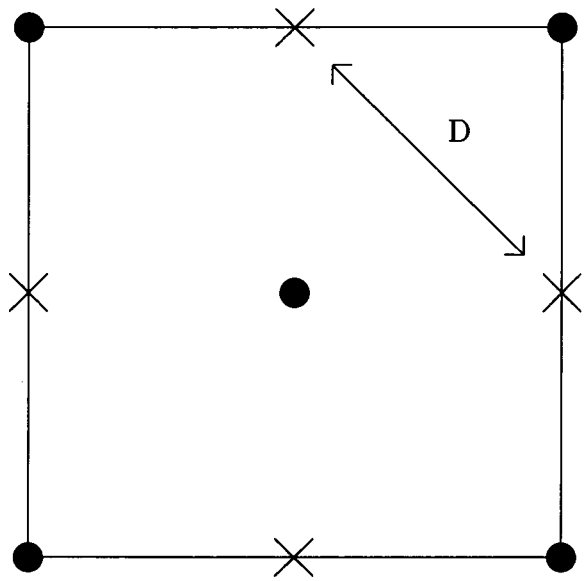

Fig. 2.1: Positioning of scalar and vector quantities on an Arakawa E-grid. Filled circles represent vector points and crosses represent scalar points. The effective distance between like grid points is shown as D.

levels (Figure 2.3). In each level the model has the horizontal grid shown in Figure 2.2. The vertical grid is defined by a set of model layer thicknesses. Vertical velocity, vertical viscosity and vertical eddy diffusivity are defined to correspond with horizontal grid scalar points, but are offset vertically so as to lie on the surfaces between layers. This allows for the calculation of sea surface elevation in Equation 2.5. All other vector and scalar points lie at the mid-depth within each layer. A feature of the HOPE model is that it fully resolves the bottom topography, and so the layer thickness of the deepest wet cell at each point in the horizontal grid is adjusted according to the local topography.

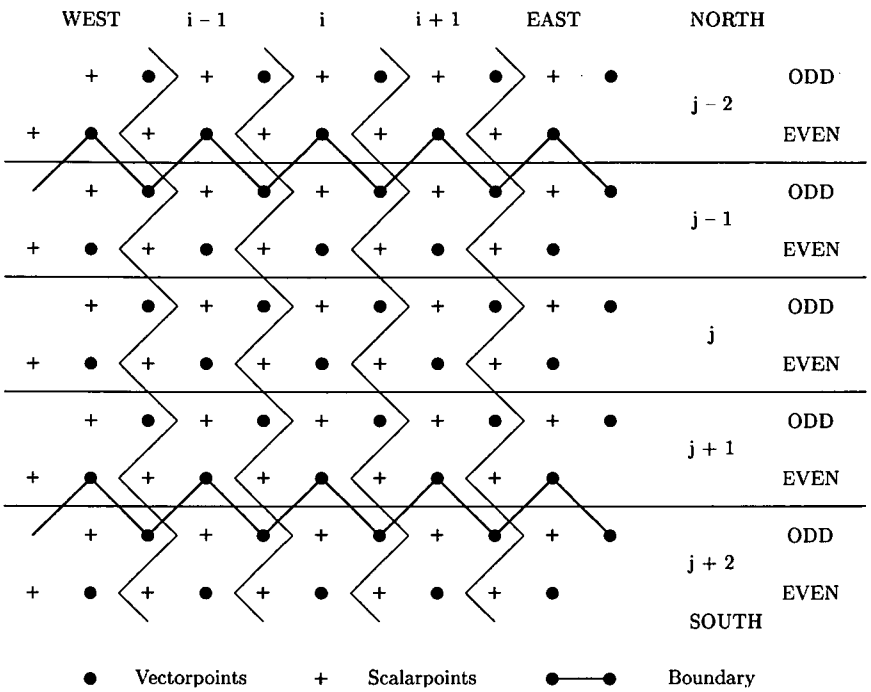

Fig. 2.2: The horizontal grid of the HOPE ocean model is a staggered Arakawa E-grid with odd/even ordering of the meridional index j (from Wolff *et al.*, 1997).

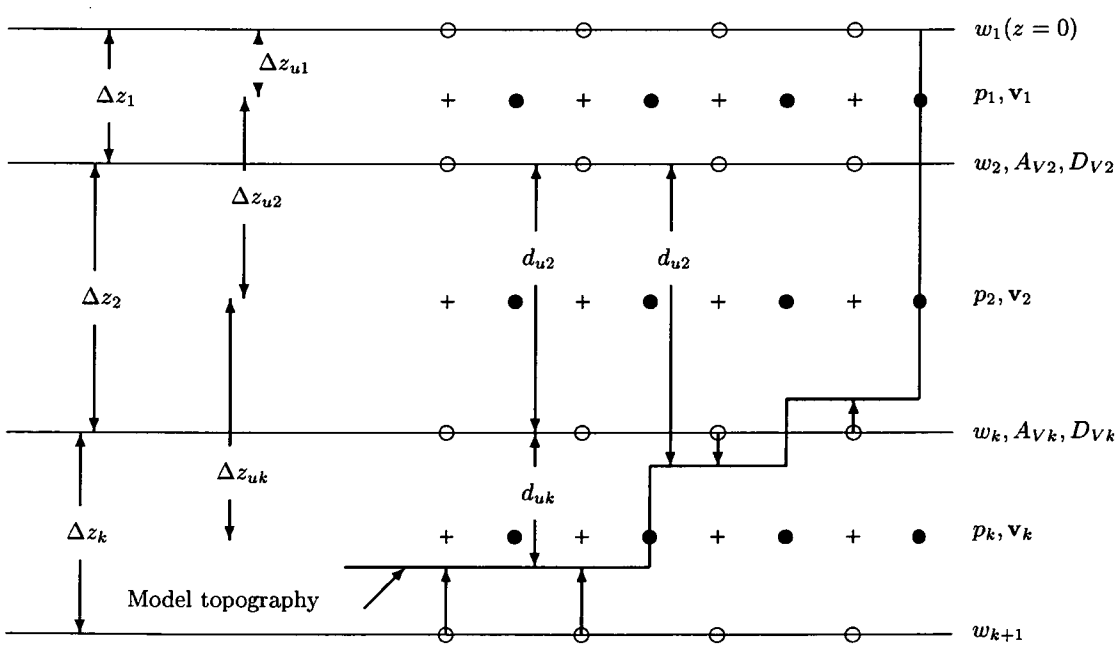

Fig. 2.3: Vertical structure of the HOPE model grid (from Wolff *et al.*, 1997). Layer thicknesses, Δz_k, are used to define the positions of all points as described in the text.

2.1.3 Time Stepping

Time stepping in the HOPE model employs the method of operator splitting (e.g. Press *et al.*, 1988). The operation of updating the set of model variables from one time step to the next is broken up into a series of nonlinear operations, as follows.

At the beginning of each time step the sea-ice model is solved for changes in sea-ice thickness, concentration and velocity. The solution of the sea-ice model also involves changes to sea surface temperature and salinity. This is followed by convective adjustment throughout the water column, the addition of wind stress, and solving for the effect of vertical advection on horizontal velocity via an upstream method. Frictional terms are then calculated, namely vertical and horizontal (Laplacian) friction, bottom friction, and biharmonic friction. Horizontal momentum advection is then solved using an energy and enstrophy conserving scheme following Arakawa and Lamb (1977). The horizontal velocity field is then resolved into barotropic and baroclinic components, and these subsystems are solved separately for new velocities. Given the new velocities, the thermohaline fields are then computed in the following order. Initially the three-dimensional thermohaline advection is calculated using a predictor/corrector scheme, and then horizontal and vertical thermohaline diffusion are calculated. A complete description of the sequence of operations for a full model time step is given by Wolff *et al.* (1997).

2.2 Dynamic/Thermodynamic Sea-Ice Model

Coupled to the HOPE model is a sea-ice model which allows prognostic calculation of sea-ice thickness, compactness and velocity. The sea-ice model was developed at the German Climate Computer Center (DKRZ), and the thermodynamic code is based on that of the Hamburg Sea Ice Model (Stössel, 1992). Sea-ice dynamics describe the motion of sea-ice subject to various external and internal forces. The external physical dynamical forcing combines atmospheric wind stress, oceanic current stress, pressure gradient forcing due to ocean surface tilt and an inertial (Coriolis) force associated with the earth's rotation. Internal forcing is characterised by a stress-strain relationship describing sea-ice response to its own motion. The thermodynamics deal with sea-ice growth and melt due to the exchange of heat between ocean and atmosphere. The inclusion of a snow layer on top of the sea-ice allows for consideration of the significant insulating effect of snow relative to sea-ice on the conduction of heat across the sea-ice/snow layer, the greater albedo of snow relative to sea-ice, and snow-ice conversion when the sea-ice becomes submerged via snow accumulation.

2.2.1 Dynamic Sea-Ice Model

Sea-ice motion is determined by a two-dimensional momentum balance equation. For sea-ice having velocity $\vec{v_i} = (u_i, v_i)$ the momentum balance is given by:

$$\frac{\partial \vec{v_i}}{\partial t} + f(\vec{k} \times \vec{v_i}) = -g\vec{\nabla}\zeta + \frac{\vec{\tau_a}}{\rho_i h_i} + \frac{\vec{\tau_o}}{\rho_i h_i} + \vec{\nabla} \cdot \sigma_{mn} \qquad (2.10)$$

with f the Coriolis parameter, $\vec{k}$ a unit vector directed away from the earth's centre, ζ the sea surface elevation, $\vec{\tau_a}$ the wind stress, $\vec{\tau_o}$ the ocean current stress, h_i the sea-ice thickness, ρ_i the ice density, g the earth's gravity, t

the time, and σ_{mn} a two-dimensional stress tensor associated with internal sea-ice stress.

The choice of σ_{mn}, or sea-ice rheology, is an important component of the momentum balance, determining the way in which ice flows, cracks, ridges, rafts and deforms. Following Hibler (1979), internal sea-ice stress is modelled in analogy to a nonlinear viscous compressible fluid obeying the constitutive law

$$\sigma_{mn} = 2\eta\dot{\epsilon}_{mn} + \left\{(\xi - \eta)(\dot{\epsilon}_{11} + \dot{\epsilon}_{22}) - \frac{P_i}{2}\right\}\delta_{mn} \tag{2.11}$$

where δ_{mn} is the Kronecker delta, with $m, n \in \{1, 2\}$, and $\dot{\epsilon}_{mn}$ is the strain rate tensor.

$$\dot{\epsilon}_{mn} = \begin{bmatrix} \dot{\epsilon}_{11} & \dot{\epsilon}_{12} \\ \dot{\epsilon}_{21} & \dot{\epsilon}_{22} \end{bmatrix} = \begin{bmatrix} \frac{\partial u}{\partial x} & \frac{1}{2}\left(\frac{\partial v}{\partial x} + \frac{\partial u}{\partial y}\right) \\ \frac{1}{2}\left(\frac{\partial v}{\partial x} + \frac{\partial u}{\partial y}\right) & \frac{\partial v}{\partial y} \end{bmatrix} \tag{2.12}$$

P_i is an internal sea-ice pressure term, ξ a nonlinear bulk viscosity, and η a nonlinear shear viscosity, defined as

$$\xi = \frac{P_i}{2\Delta} \tag{2.13}$$

$$\eta = \frac{\xi}{e^2} \tag{2.14}$$

$$\Delta = \left[\left(\dot{\epsilon}_{11}^2 + \dot{\epsilon}_{22}^2\right)\left(1 + \frac{1}{e^2}\right) + 4\frac{\dot{\epsilon}_{12}^2}{e^2} + 2\dot{\epsilon}_{11}\dot{\epsilon}_{22}\left(1 - \frac{1}{e^2}\right)\right]^{\frac{1}{2}} \tag{2.15}$$

Here e is the ratio of the principal axes of the yield ellipse. The yield ellipse is the curve in two-dimensional stress space defining the boundary between viscous and plastic behaviour. Within the ellipse sea-ice deforms as a linear viscous fluid, on the ellipse sea-ice deforms as a plastic, and points outside of the ellipse cannot be reached. The sea-ice pressure (P_i) is a function of compactness (A) and thickness (h_i), given by

$$P_i = P^* h_i \cdot e^{-C(1-A)} \tag{2.16}$$

where P^* and C are empirically derived constants with values taken from Hibler (1979). When the strain rates are small Δ in Equation 2.15 becomes

very small and the viscosities in Equations 2.13 and 2.14 become very large. To avoid numerical complications when the strain rate approaches zero the nonlinear shear (η) and bulk (ξ) viscosities are chosen to be the minimum of their actual values according to Equations 2.13 and 2.14 and an empirically chosen maximum value corresponding to the function value given in Equations 2.13 and 2.14 when

$$\Delta = \Delta_{min} = 2.0 \times 10^{-9} \tag{2.17}$$

2.2.2 Thermodynamic Sea-Ice Model

Thermodynamics of sea-ice involves the determination of the local growth rate at the base of the sea-ice, along with the local melt rate at both the surface and the base of the sea-ice. In the presence of a fractional sea-ice cover, i. e. one containing areas of open water, the surface heat balance is solved separately for the ice covered and ice free areas. Denoting the open water heat flux by Q_w and the heat flux over sea-ice by Q_i, the net surface atmospheric heat flux (Q_a) is given by

$$Q_a = (1 - A)Q_w + AQ_i \tag{2.18}$$

where A is the sea-ice compactness.

Over open water the surface heat balance is given by:

$$Q_w = Q_w^{sw} + Q_w^{lw}\downarrow + Q_w^{lw}\uparrow + Q_w^{se} + Q_w^{la} \tag{2.19}$$

In this study the incoming longwave ($Q_w^{lw}\downarrow$) and latent (Q_w^{la}) heat fluxes are prescribed as part of the surface forcing, as is the incident shortwave radiation heat flux (Q_w^{incsw}). The actual shortwave (Q_w^{sw}), outgoing longwave ($Q_w^{lw}\uparrow$) and sensible (Q_w^{se}) heat fluxes are parameterised as:

$$Q_w^{sw} = (1 - \alpha_w)Q_w^{incsw} \tag{2.20}$$

$$Q_w^{lw}\uparrow = \varepsilon_w \sigma \Theta_1^4 \tag{2.21}$$

$$Q_w^{se} = \rho_a c_a C_H V_w (T_a - \Theta_1) \tag{2.22}$$

Here α_w is the albedo (reflectivity) of sea water, σ is the Stefan-Boltzmann constant, and T_a is the surface air temperature two meters above sea level (sometimes referred to as screen temperature). The emissivity of sea water is denoted by ε_w, and Θ_1 is the potential temperature of the upper layer of the ocean model. Air density, ρ_a, is taken to be constant, c_a is the specific heat capacity of air, C_H a constant coefficient of sensible heat transfer and V_w is the wind speed.

In regions where a sea-ice cover exists, the associated atmospheric heat flux (Q_i) is given by:

$$Q_i = Q_i^{sw} + Q_i^{lw}\downarrow + Q_i^{lw}\uparrow + Q_i^{se} + Q_i^{la} \tag{2.23}$$

As for over open water the incident shortwave (Q_i^{incsw}), downward longwave ($Q_i^{lw}\uparrow$) and latent (Q_i^{la}) heat fluxes are prescribed. The radiative flux parameterisations are similar to the ones over open water, but surface values are appropriate for a sea-ice or snow cover.

$$Q_i^{sw} = (1-\alpha_{srf})Q_i^{incsw} \tag{2.24}$$

$$Q_i^{lw}\uparrow = \varepsilon_{srf}\sigma T_{srf}^4 \tag{2.25}$$

$$Q_i^{se} = \rho_a c_a C_H V_w (T_a - T_{srf}) \tag{2.26}$$

$$\tag{2.27}$$

Here T_{srf} is the surface temperature of the sea-ice or snow (where a snow layer exists), ε_{srf} is the emissivity of sea-ice or snow and the surface reflectivity (α_{srf}) in Equation 2.24 takes one of four possible values determined by the absence or presence of snow, and by whether the surface temperature of the sea-ice or snow is below 0°C (freezing) or equal to 0°C (melting).

$$\alpha_{srf} = \begin{cases} \alpha_{im} & \text{for sea-ice surface and melting} \\ \alpha_{if} & \text{for sea-ice surface and freezing} \\ \alpha_{sm} & \text{for snow surface and melting} \\ \alpha_{sf} & \text{for snow surface and freezing} \end{cases} \tag{2.28}$$

The full surface heat exchange process for an arbitrary grid cell in the upper layer of the HOPE model is shown in Figure 2.4. At the upper surface are the fluxes defined by Equations 2.19 and 2.23. The other heat fluxes shown are a conductive heat flux (Q_{cond}) through the sea-ice/snow layer and an oceanic heat flux (Q_{ohf}) from the ocean model surface layer into the base of the sea-ice. The oceanic heat flux is the sum of heat transport to the surface layer by oceanic processes, being convection (Q_{con}), advection (Q_{adv}) and diffusion (Q_{dif}). It is described in more detail in Section 3.4. All fluxes are defined to be positive upwards.

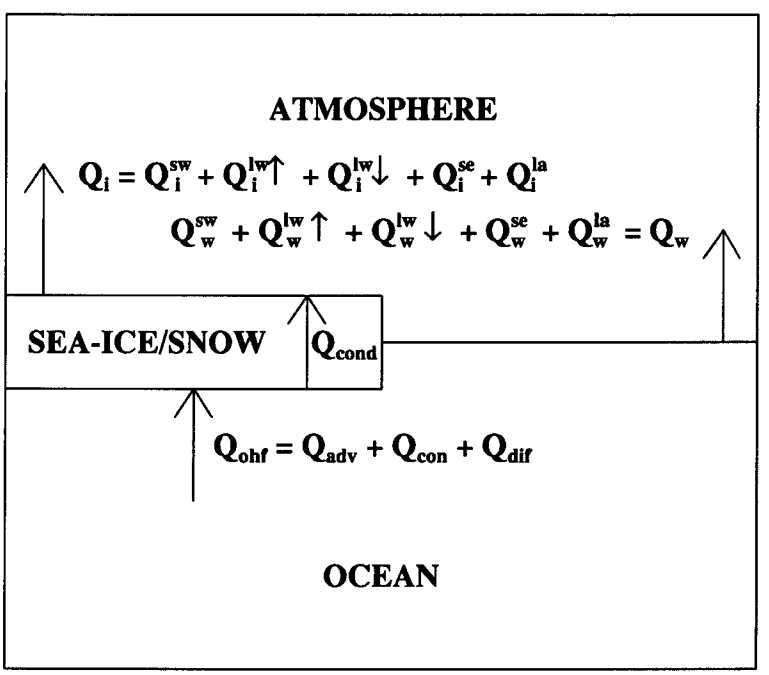

Fig. 2.4: Exchanges of heat in the thermodynamic sea-ice model for an arbitrary ocean surface grid cell. Sea-ice/atmosphere exchange is denoted by Q_i, ocean/atmosphere exchange by Q_w, the conductive flux through the sea-ice/snow layer by Q_{cond}, and the oceanic heat flux by Q_{ohf}.

The conductive heat flux within the sea-ice/snow layer is assumed to be directly proportional to the temperature gradient across the sea-ice/snow

layer and inversely proportional to the thickness of that layer.

$$Q_{cond} = k_i \frac{(T_{freeze} - T_{srf})}{\tilde{h}_i} \tag{2.29}$$

Here k_i is the thermal conductivity of sea-ice, T_{freeze} the freezing temperature of sea water, T_{srf} the upper surface temperature of the sea-ice/snow layer and $\tilde{h}_i$ the effective thermodynamic sea-ice thickness of the sea-ice/snow layer. This effective thickness is defined to be

$$\tilde{h}_i = \frac{1}{A}\left(h_i + h_{sn}\frac{k_i}{k_{sn}}\right) \tag{2.30}$$

where h_{sn} is the snow layer thickness and k_{sn} is the thermal conductivity of the snow. The ratio of the thermal conductivity of sea-ice with respect to that of snow, $\frac{k_i}{k_{sn}}$, is approximately 7. This means that snow is seven times more effective as an insulator against oceanic heat loss to the atmosphere than sea-ice. Hence, even a relatively thin snow cover will result in a much increased effective sea-ice thickness. Atmospheric precipitation is converted to snow fall when the surface air temperature, T_a, is below 0°C. Snow loading on the sea-ice may result in the submerging of the sea-ice/snow interface. In such cases the thickness of the snow draft is converted to sea-ice. Since the heat of fusion of snow is slightly greater than the heat of fusion of sea-ice, this process results in a net heat gain to the sea-ice/snow layer. To close the heat balance of the conversion process a small additional amount of snow is also melted.

A thermodynamic equilibrium is sought at the interface between the atmosphere and the sea-ice/snow layer. From above there is an atmospheric heat flux (Q_a) defined in Equation 2.23, and from below the conductive heat flux (Q_{cond}) through the sea-ice/snow layer. An iterative solution, T^*_{srf}, is then found for the sea-ice/snow layer surface temperature, T_{srf}, from the energy balance equation

$$Q_i + Q_{cond} = 0 \tag{2.31}$$

When the iterated solution, T^*_{srf}, is greater than 0°C, the left-hand side of Equation 2.31 is re-calculated with T_{srf} replaced by 0°C and the resultant,

Q_{res}, is used to melt snow and then sea-ice from above. In the case where the entire sea-ice/snow layer is melted from above, any remaining heat is added to Q_w in Equation 2.19.

To complete the sea-ice thermodynamic evolution a heat balance equation must also be applied at the ocean/sea-ice and ocean/atmosphere interfaces. The balance equation takes the form

$$\rho_0 c_w \Delta z_1' \frac{\partial \hat{\Theta}_1}{\partial t} = Q_w + Q_{cond} - h_i \rho_i L_f \tag{2.32}$$

and is solved for the upper layer oceanic temperature, $\hat{\Theta}_1$. Here c_w is the specific heat capacity of sea water, L_f is the latent heat of fusion of sea-ice, and $\Delta z_1'$ is the thickness of the upper ocean layer, given by

$$\Delta z_1' = \Delta z_1 + \zeta - h_{draft} \tag{2.33}$$

where Δz_1 is the defined thickness of the upper layer (see Section 2.1.2), ζ the sea surface elevation and h_{draft} the draft of the sea-ice/snow layer, given by:

$$h_{draft} = \frac{1}{\rho_w}(\rho_i h_i + \rho_s h_s) \tag{2.34}$$

Here h_i, h_s are the thicknesses, and ρ_i, ρ_s are the densities of the sea-ice and snow layers respectively. For the sea-ice under-surface to be in thermal equilibrium with the upper ocean it is required that $T_{melt} \leq \Theta_1 \leq T_{freeze}$. To maintain this equilibrium sea-ice/snow is melted when the solution for $\hat{\Theta}_1$ from Equation 2.32 is above T_{melt}, and new sea-ice is formed when $\hat{\Theta}_1$ is below T_{freeze}. For the purposes of this study the effect of salinity on the freezing and melting temperatures is ignored, and constant values of $T_{freeze} = -1.89°C$ and $T_{melt} = 0°C$ are used. The model upper layer ocean temperature, Θ_1, is only allowed to rise above T_{melt} when all of the sea-ice/snow layer has been melted within a grid cell. In the case of freezing from below the new upper ocean temperature, Θ_1, and the change in sea-ice thickness, Δh_i are:

$$\Theta_1 = T_{freeze} \tag{2.35}$$

$$\Delta h_i = \frac{\hat{\Theta}_1 - T_{freeze}}{\rho_i L_f} \cdot \rho_0 c_w \Delta z_1' \tag{2.36}$$

For melting conditions the new ocean surface layer temperature and the change in sea-ice thickness are given by:

$$\Theta_1 = \hat{\Theta}_1 - \min\left\{\frac{h_i \rho_i L_f}{\rho_0 c_w \Delta z_1'}, \hat{\Theta}_1 - T_{freeze}\right\} \tag{2.37}$$

$$\Delta h_i = \max\left\{(T_{freeze} - \hat{\Theta}_1)\frac{\rho_0 c_w \Delta z_1'}{\rho_i L_f}, 0\right\} \tag{2.38}$$

The thermodynamic processes of sea-ice growth and melt are assumed to affect the sea-ice compactness within a grid cell in the following ways. When freezing occurs over open water areas the sea-ice compactness increases (i. e. leads concentration decreases) at a rate given by

$$\Delta A^{thin} = \max\left\{\frac{\Delta h_i^{thin}(1 - A)}{h_o \Delta t}, 0\right\} \tag{2.39}$$

where $\Delta h_i^{thin} = \Delta t Q_w/(\rho_i L_f)$ is the thickness of new sea-ice formed and h_o is an arbitrary demarcation thickness (taken to be 0.5 m following Hibler (1979)). When melting of thick sea-ice occurs the sea-ice compactness decreases (i. e. leads concentration increases) at a rate given by

$$\Delta A^{thick} = \min\left\{\frac{\Delta h_i^{thick} A}{2 h_i \Delta t}, 0\right\} \tag{2.40}$$

where Δh_i^{thick} is the change in sea-ice thickness due to the melting. This formulation is based on the assumption that sea-ice thickness within a grid cell has a uniform distribution between 0 and $2h_i$. The change in compactness of sea-ice due to thermodynamic lead opening and closing is then calculated as the sum of both these terms, i. e.

$$\frac{\partial A}{\partial t} = \Delta A^{thin} + \Delta A^{thick} \tag{2.41}$$

Completion of the sea-ice thermohaline coupling to the ocean model requires consideration of salt and fresh water exchanges during sea-ice growth and melt. Sea-ice is assumed to have a constant salinity independent of

it's age and denoted by S_{ice}. The ocean model's upper layer salinity, S_1, is modified by an amount ΔS due to the surface fresh water flux (modified by snow fall which accumulates on top of the sea-ice) and due to sea-ice growth or melt, according to:

$$(S_1 + \Delta S)\,\Delta z'^{old} + \frac{\rho_i h_i^{old}}{\rho_w} S_{ice} = S_1 \Delta z'^{new} + \frac{\rho_i h_i^{new}}{\rho_w} S_{ice} \qquad (2.42)$$

Here $\Delta z'^{old}$ is the upper ocean layer thickness modified by sea surface elevation and sea-ice draft as in Equation 2.33, and also modified by the atmospheric precipitation minus evaporation. $\Delta z'^{new}$ is $\Delta z'^{old}$ modified by the new sea-ice draft due to melt or growth, and $h_i^{new} - h_i^{old}$ is the amount of sea-ice growth (if positive) or melt (if negative).

Snow loading on the sea-ice may result in the submerging of the sea-ice/snow interface. In such cases the thickness of the snow draft is converted to sea-ice, and in terms of heat an equivalent amount of snow is melted (i. e. heat of fusion of the sea-ice formation equals the heat of fusion of the snow melting).

3. THE EAST ANTARCTIC HIGH-RESOLUTION COUPLED OCEAN/SEA-ICE MODEL

3.1 Location, Topography, Initialisation and Forcing

In order to better understand the complex interactions of the many physical processes involved in the Southern Ocean coupled ocean/sea-ice system in an area of seasonal sea-ice advance and retreat, the coupled ocean/sea-ice model has been formulated to simulate these interactions over a region covering approximately one million square kilometers of the South-East Indian Basin (see Figure 3.1). The area modelled is south of Australia and adjoins the Wilkes, Banzare and Sabrina coastlines of East Antarctica. Major coastal features are Porpoise Bay (128°E) and the Dibble Ice Tongue Glacier (135°E). The northern boundary is artificially closed with a solid wall at 57°S. To avoid the complexities of open boundaries at the east and west edges of the model, while maintaining the zonal nature of the Antarctic Circumpolar Current (ACC) and coastal counter current through the modelled region, the east-west boundary is re-entrant (periodic). Model topography is obtained using bicubic spline interpolation applied to the ETOP05 data set (NOAA, 1988). The bottom topography is smoothed using linear interpolation across a band extending $\frac{1}{2}^{\circ}$ in longitude towards

the model interior from either side of the periodic boundary. The resulting model topography is shown in Figure 3.2. The major bathymetric features are the continental shelf, steep continental slope, and abyssal plain.

High-resolution in the horizontal allows for the explicit inclusion of the effects of the ocean's eddy dynamics on the sea-ice. In this study the resolution used is $\frac{1}{4}^\circ$ in latitude and $\frac{1}{2}^\circ$ in longitude in each of the subgrids (odd/even) of the Arakawa E-grid. This gives an effective spacing (D in Figure 2.1) of 19.6 km at 60°S. Due to the computational intensity of the model, the use of such high-resolution limits the study to being regional in extent. The vertical resolution of the model is made up of twelve layers having thicknesses of 10, 10, 30, 50, 100, 200, 500, 600, 750, 750, 750, and 1250 meters from surface to bottom respectively. The model time step, Δt, is half an hour, and a model year is made up of 12 months each of 30 days.

A 60 year reference simulation was initialised with the ocean at rest and no sea-ice present. The ocean and sea-ice model constants used are shown in Tables 3.1 and 3.2 respectively. Mean annual potential temperature and

Ocean model constants			
Symbol	Description	Value	Eqn
α_w	Sea water albedo	0.10	2.20
ρ_O	Density of sea water	1023.5 kg m^{-3}	2.1
A_H	Harmonic horizontal viscosity coefficient	500 m^2 s^{-2}	2.2
A_V	Vertical coefficient of eddy viscosity	4.0×10^{-3} m^2 s^{-2}	2.3
B_H	Biharmonic horizontal viscosity coefficient	0 m^4 s^{-2}	2.2
D_H	Coefficient of horizontal diffusivity	200 m^2 s^{-2}	2.8
D_V	Coefficient of vertical diffusivity	2.0×10^{-4} m^2 s^{-2}	2.8
c_w	Specific heat capacity of sea water	4.0×10^3 J kg^{-1} K^{-1}	2.32
g	Acceleration due to gravity	9.81 m s^{-2}	2.1

Tab. 3.1: Values of constants and parameters in the high-resolution ocean model.

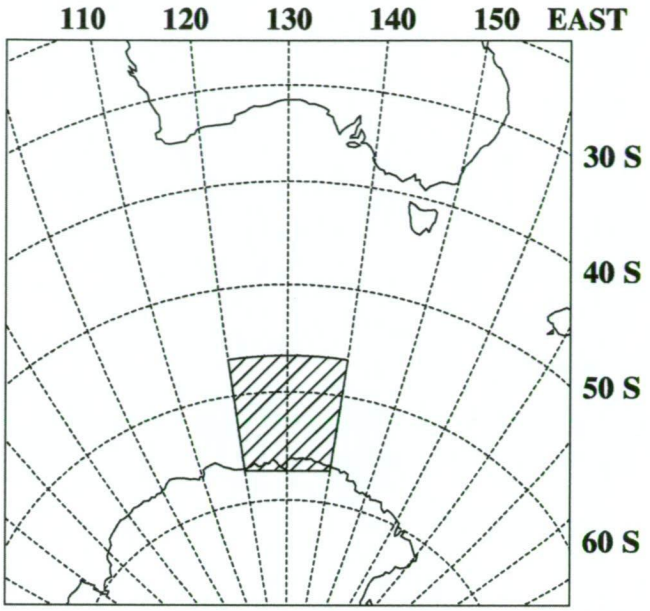

Fig. 3.1: Hatched area shows the location of the re-entrant channel model with respect to the Australian and Antarctic continental landmasses.

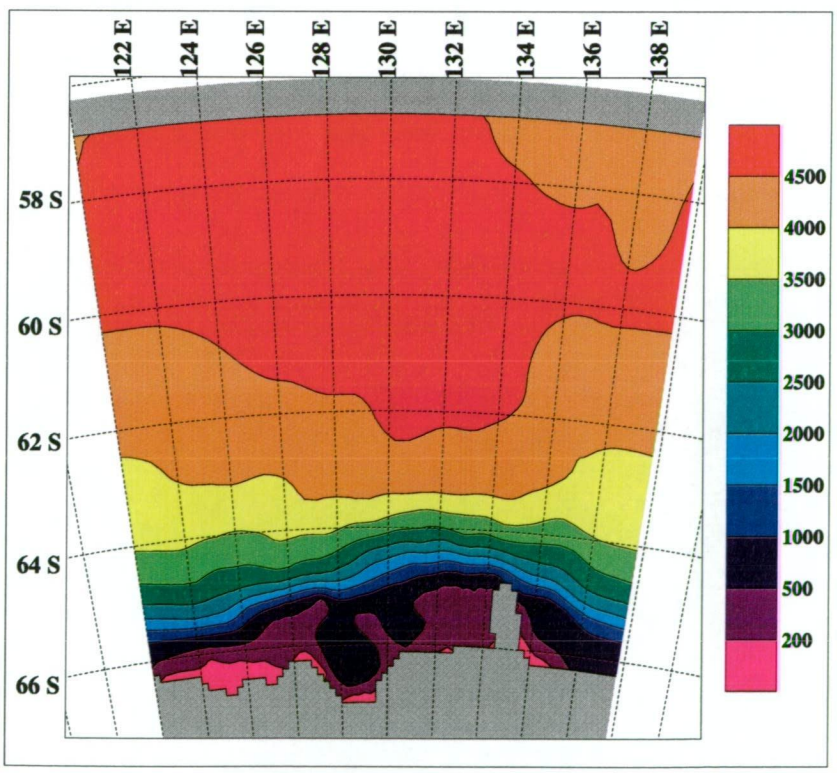

Fig. 3.2: Bathymetry of the high-resolution re-entrant channel model. Depths are in meters. The protrusion at 135°E is the Dibble Ice Tongue.

Sea-ice model constants			
Symbol	Description	Value	Eqn
α_{if}	Freezing sea-ice albedo	0.75	2.28
α_{im}	Melting sea-ice albedo	0.66	2.28
α_{sf}	Freezing snow albedo	0.85	2.28
α_{sm}	Melting snow albedo	0.75	2.28
ε_i	Emissivity of sea-ice	0.97	2.25
ε_s	Emissivity of snow	0.97	2.25
ε_w	Emissivity of sea water	0.97	2.21
ρ_a	Density of air	1.3 kg m^{-3}	2.22
ρ_i	Density of sea-ice	910 kg m^{-3}	2.10
ρ_s	Density of snow	330 kg m^{-3}	2.34
σ	Stefan-Boltzmann constant	5.67×10^{-8} W m^{-2} K^{-4}	2.21
C	Constant for internal sea-ice pressure	20	2.16
C_H	Coefficient of sensible heat transfer	1.75×10^{-3}	2.22
L_f	Latent heat of fusion of sea-ice	2.7×10^{8} J m^{-3}	2.32
P^*	Constant for internal sea-ice pressure	5000 N m^{-1}	2.16
S_{ice}	Salinity of sea-ice	5 psu	2.42
T_{freeze}	Freezing temperature of sea water	-1.9°C	2.29
c_a	Specific heat capacity of air	1004 J kg^{-1} K^{-1}	2.22
e	Ratio of principle axes of yield ellipse	2.0	2.14

Tab. 3.2: Values of constants and parameters in the high-resolution sea-ice model.

salinity data corresponding to the modelled region was extracted from the Levitus (1994a,b) Atlas. The temperature and salinity data were linearly interpolated onto model depths (there are 33 levels in the atlas data and only 12 in the model). This data was then zonally averaged, and finally linearly interpolated along lines of equal longitude to produce temperature and salinity initialisation fields corresponding to the model grid (Figures 3.3, 3.4).

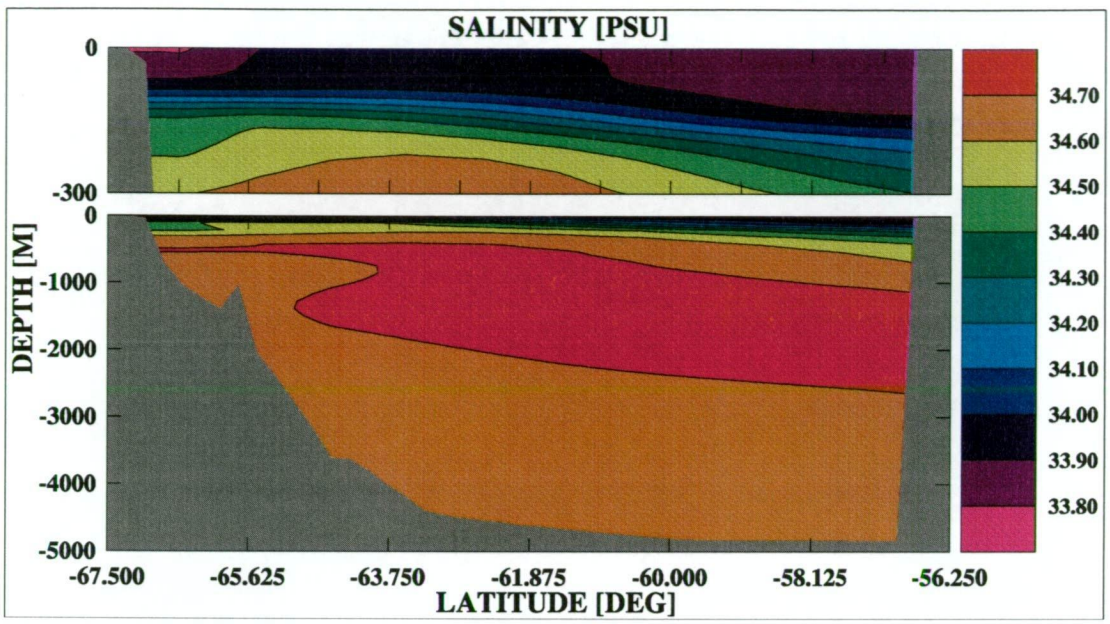

Fig. 3.3: Meridional cross-section of model salinity initialisation, obtained from Levitus (1994a) as described in the text.

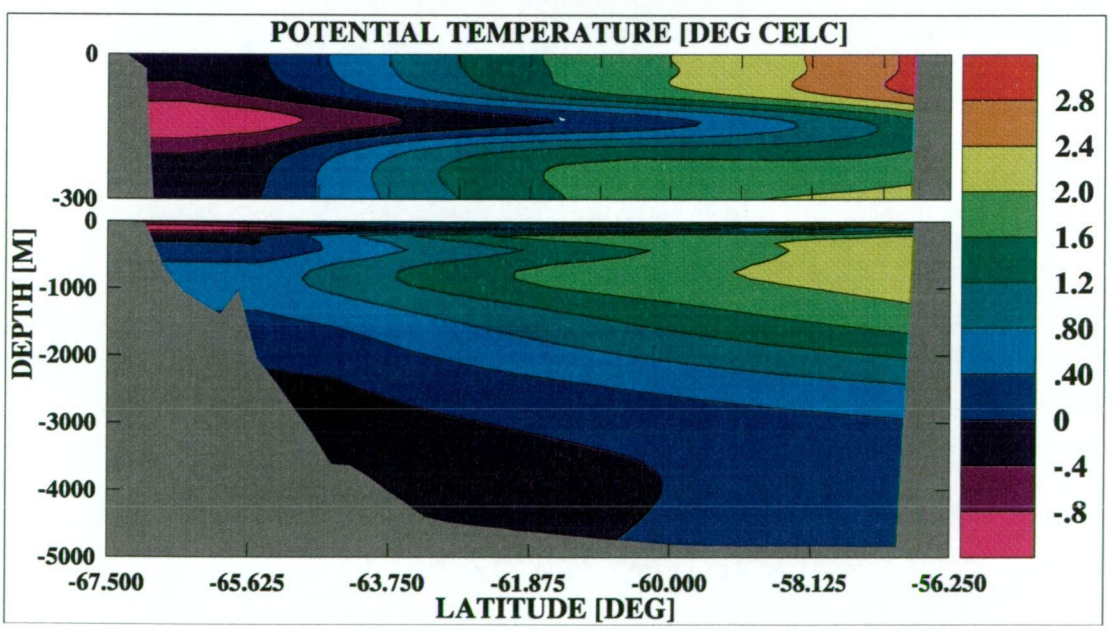

Fig. 3.4: Meridional cross-section of model temperature initialisation, obtained from Levitus (1994b) as described in the text.

Forward integration of the model initial value problem requires the specification of surface heat and fresh water fluxes. Surface forcing fields are prescribed as mean monthly data sets. Linear interpolation in time is then used to provide instantaneous forcing fields each model time step. The mean monthly data is used to represent the actual forcing at the midpoint of the month, and so the reference simulation begins on January 16^{th}. The mean monthly fields of surface air temperature, northward and eastward wind stress, precipitation and evaporation, and incident shortwave and longwave radiation were generated from 10 years of output from the CSIRO 9 coupled atmosphere/sea-ice/ocean model (Gordon and O'Farrell, 1997, as modified by Hirst *et al.*, 1999) corresponding to the years 1981–1990 of the transient CO_2 integration described by Hirst (1999). This decade of forcing data was then averaged onto an annual mean monthly repeat cycle which was used to force the model's upper surface. Due to a lack of available humidity data, monthly mean zonally averaged values of latent heat flux for the Southern Hemisphere are used to close the surface heat balance. The effects of atmospheric cloud cover are implicitly included in the radiation forcing, as cloud parameterisations are used in the CSIRO 9 atmospheric component. The full set of surface forcing used is shown in Appendix A.

Boundary forcing of temperature and salinity is applied at the northern wall to avoid excessive drift of the model's thermohaline characteristics with time. Such drift would otherwise result due to the regional nature of the model, the positive surface fresh water flux to the ocean within that region, and the continual surface heat loss to the atmosphere. Model temperature is relaxed to the initialisation field at all depths within a 'sponge layer' (e. g. Bryan and Lewis, 1979) extending 1.25° south from the northern boundary. The relaxation time constant linearly decreases from 60 days at the boundary to 180 days at the southernmost point in the 'sponge layer'. In some sense this artificial supply of heat to the model is representative of the poleward heat transport in the real ocean. The model mass is adjusted

during each time step to avoid unbounded growth due to the excess of precipitation over evaporation. This is done after the input of precipitative mass by firstly calculating the integral of relative surface elevation over the entire modelled region, and secondly by subtracting this integral uniformly from the surface elevation at each grid cell. This results in the integrated surface elevation over the model domain being reset to zero each time step. The salt content of any removed mass is then added back uniformly at the northern wall to prevent any trend towards decreasing salinity with time. Preliminary experiments showed that this process led to unrealistically high deep water salinity in the long term, and so it was decided that the salt would only be added back to the upper 7 model layers (900 m).

3.2 Ocean Model Response

The mass transport in Sverdrups (1 Sv = 10^6 m^3 s^{-1}) across the periodic boundary of the ocean model is shown in Figure 3.5. Initially the flow is eastward due to the density gradient associated with the Levitus (1994a,b) initialisation data. With time the direction of flow in the channel is determined by the applied wind stress. After approximately 20 years the mass flux settles into a quasi-stable equilibrium where the net flow is westward. The mean mass flux over the final 20 years is -31.3 Sv, with variation of 35–40 Sv within each year. Figure 3.6 shows the mass transport for the last 5 years of the reference simulation. The periodicity of the mass transport from year to year indicates a strong barotropic response of the modelled ocean to the mean monthly wind stress cycle with some small modulation due to the baroclinic processes.

For comparison, the integrated mass transport along the World Ocean Circulation Experiment (WOCE) transect SR3 from Tasmania to Antarctica is shown in Figure 3.7. The WOCE estimates were obtained using CTD data from 6 cruises of the Australian research and supply ice-breaker, *RSV Aurora Australis*. The observational transect was at approximately 140°E in the latitude band 57–66°S, which matches the eastern boundary of the ocean model. The WOCE data indicates that this region is responsible for about 50 Sv of the approximately 150 Sv transport from west to east in the Southern Ocean south of Tasmania.

There are several possible causes for the discrepancy in the sign of the mass transport between the model and observations: the closed northern boundary of the model does not allow for the shear effects from the strong ACC to the north; the monotonically increasing nature of the WOCE data based estimate south of 60°S suggests that this data does not resolve the westward flowing coastal counter current; and the coarse resolution of the CSIRO 9 winds may produce a bias in the model towards a too strong

coastal counter current. In a preliminary study (Marsland and Wolff, 1998), the East Antarctic model has been run using the wind forcing climatology of Hellerman and Rosenstein (1983) which gives much better agreement of mass transport with the WOCE data, but has no coastal counter current at all as that data set has westerly winds everywhere in the model domain.

Figure 3.8 shows the mean horizontal stream function over the final decade of the 60 year reference simulation. The flow is strongest in the region 62–64°S. The corresponding meridional overturning streamfunction is shown in Figure 3.9. There are two cells active: the counter-clockwise cell in the southern part of the model produces around 0.3 Sv of overturning; and the clockwise cell in the northern part of the model produces over 0.5 Sv. The southern cell is driven by buoyancy forcing at the surface, where cold temperatures and brine rejection combine to increase the ocean density. The northern cell is driven by the surface wind stress. In the northern part of the model the predominantly westerly winds generate a northward flowing Eckman component in the ocean's surface layer, which drives a strong downwelling at the closed northern boundary. The strong dependence of the model's surface layer on the applied wind stress, with respect to lower layers, is shown by plots of horizontal velocity streamlines in Figure 3.10. The winds generate a divergence zone at the surface, with strong equatorward flow north of 60°S and a weaker poleward flow south of 60°S.

The terms in the zonally integrated momentum balance of the modelled channel flow are shown in Figure 3.11. Momentum input to the system is via the wind stress, which for sea-ice covered regions appears as a modified ocean/sea-ice stress. The baroclinic form stress is associated with the internal pressure gradient and is roughly in balance with the stress induced by the gradient in the model's free surface elevation (i. e. the barotropic form stress). The Reynold's stress is relatively small, as are the frictional terms. The zig-zag nature of the Laplacian friction term is indicative of

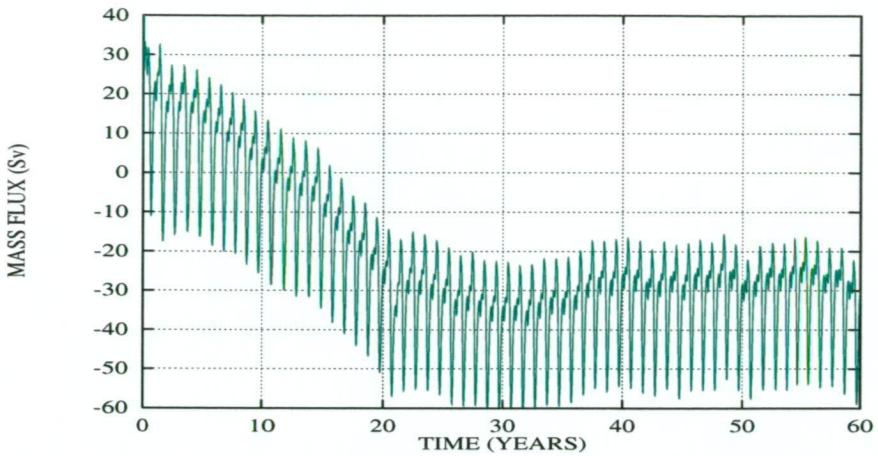

Fig. 3.5: Mass transport (Sv) across the periodic east-west boundary of the ocean model for the full 60 years of the reference simulation.

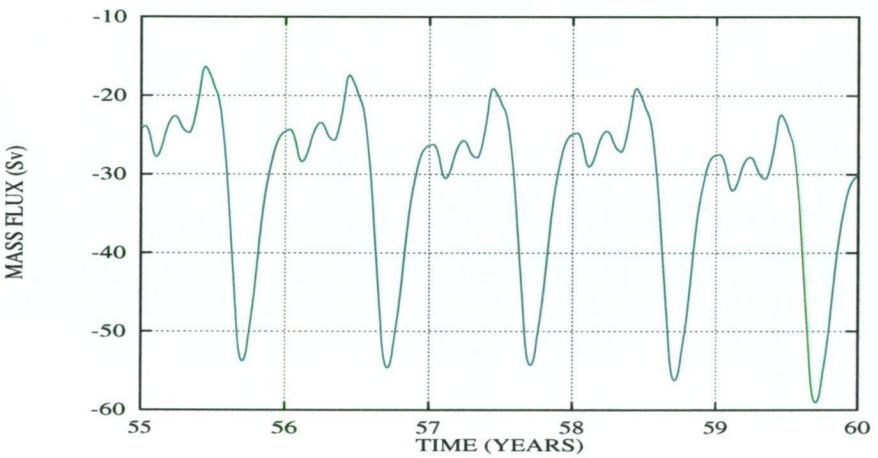

Fig. 3.6: Mass transport (Sv) across the periodic east-west boundary of the ocean model for the last 5 years of the reference simulation.

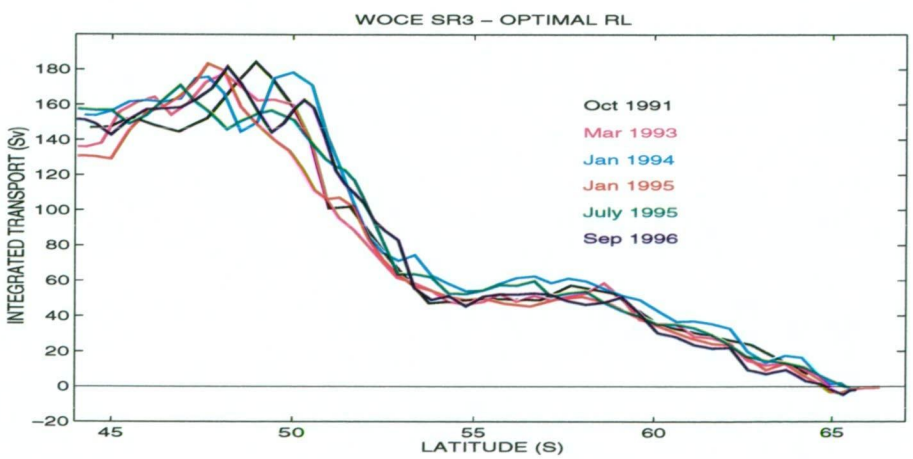

Fig. 3.7: Integrated mass transport along 6 repeats of the WOCE transect SR3 (bottom) from Tasmania to Antarctica during the period October 1991 to September 1996 (S. R. Rintoul, pers. comm.).

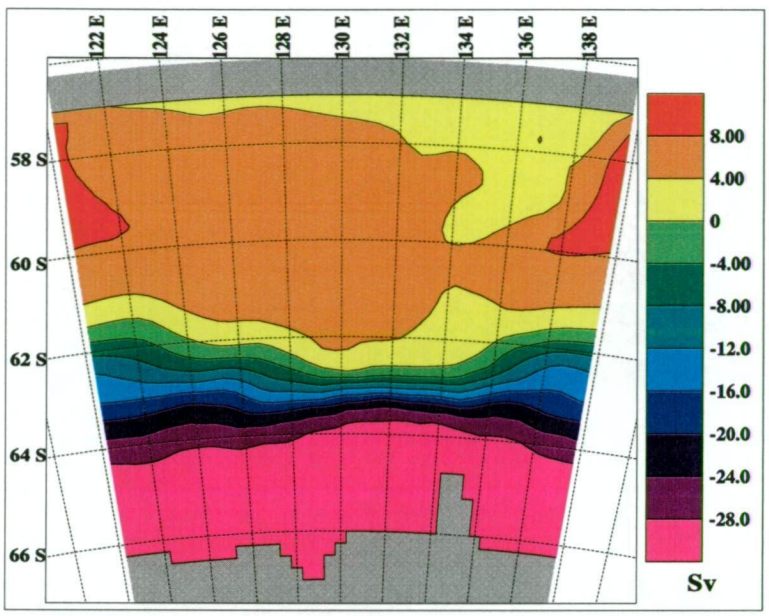

Fig. 3.8: Horizontal stream function (Sv) averaged over the last 10 years of the 60 year reference simulation.

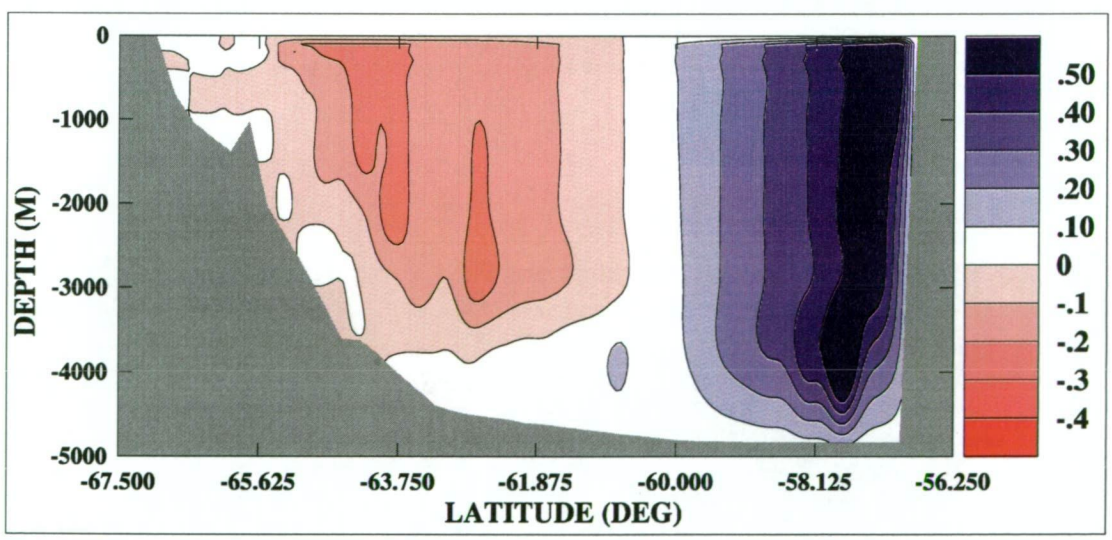

Fig. 3.9: Meridional overturning stream function (Sv) averaged over the last 10 years of the 60 year reference simulation.

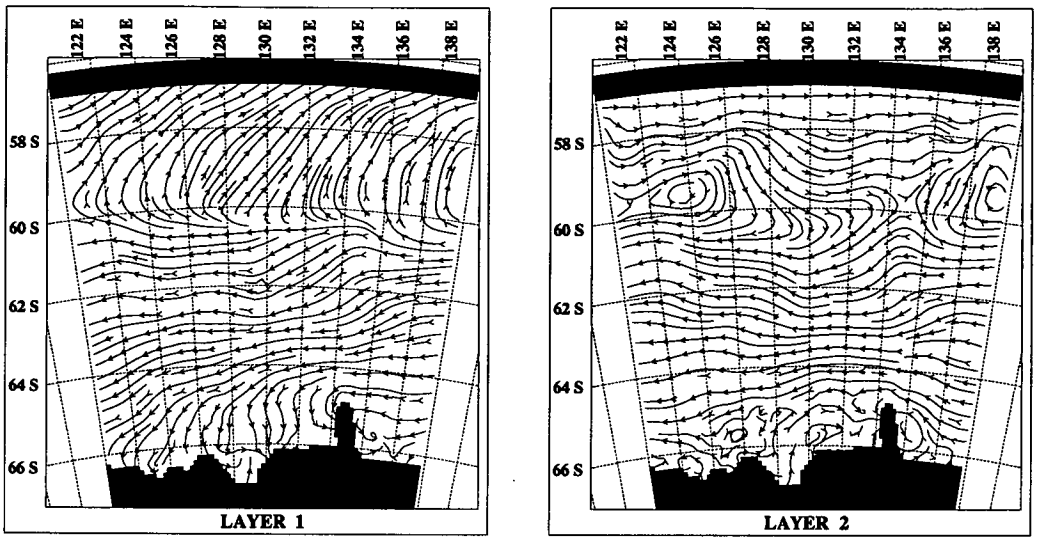

Fig. 3.10: Streamlines of horizontal flow averaged over the last 10 years of the reference simulation for the surface layer (0–10 m; left), and for layer 2 (10–20 m; right).

grid-splitting or *chequer-boarding* between the odd and even subgrids of the Arakawa E-grid. Ideally ocean models should require no such artificial numerical friction, but the removal of the small Laplacian friction term altogether was found to result in *chequer-boarding* problems elsewhere in the model. The grid-splitting was also found to be both qualitatively and quantitatively more severe when using a higher-order biharmonic formulation of numerical friction. That the overall sum is not zero is attributed to the shortness of both the length of the averaging period (10 years) and the length of the simulation (60 years).

The thermodynamic evolution of the model over the course of the reference simulation is shown in Figure 3.12 (salinity) and Figure 3.13 (temperature). In general the deep layers (e. g. layers 9 and 11) show a trend towards increasing salinity and temperature. This is at least partly due to the strong downwelling at the northern boundary, which acts to mix the relatively warm and salty intermediate waters through the model. The downwelling acts to increase the mean model temperature by approximately

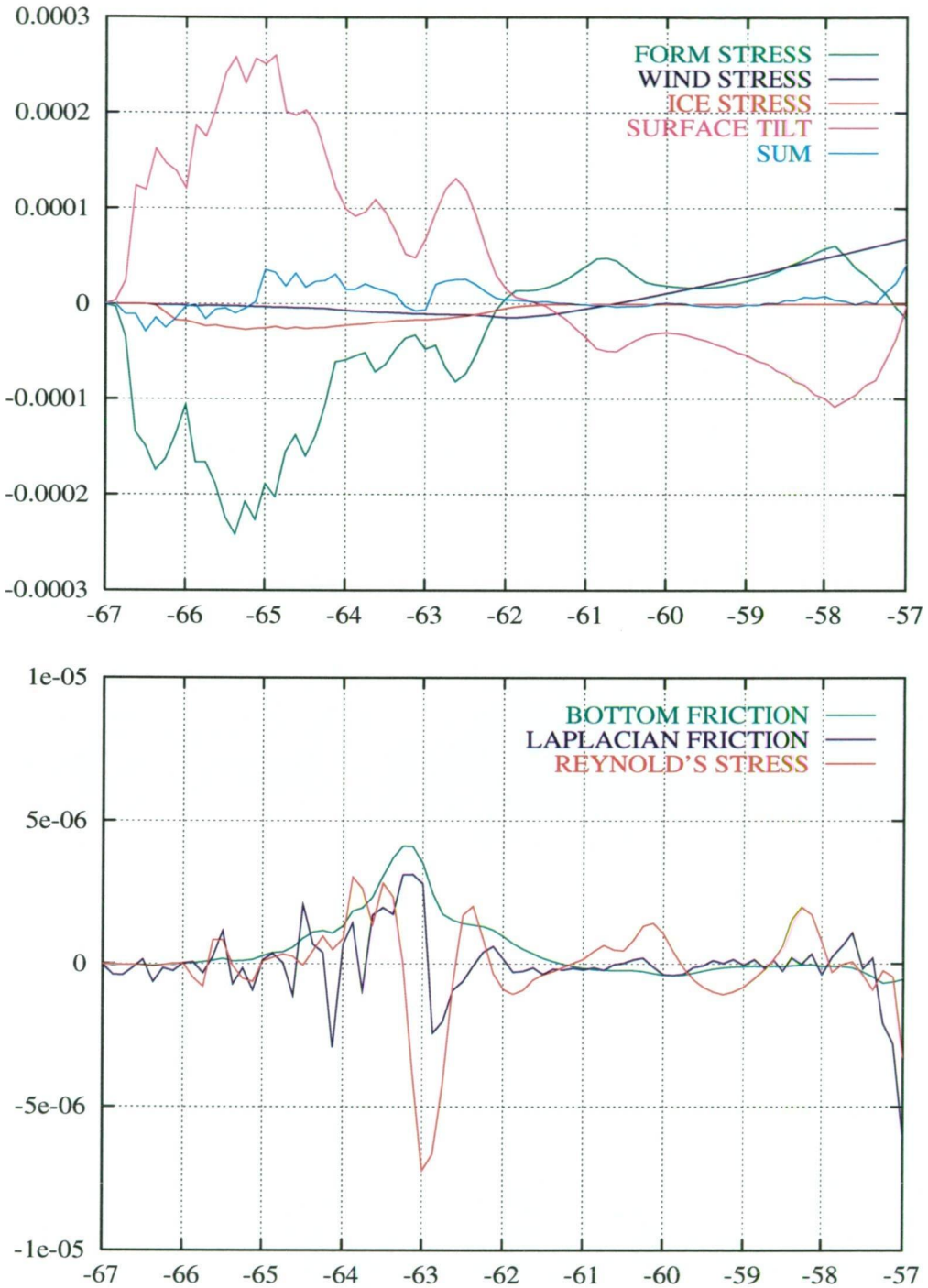

Fig. 3.11: Zonally integrated momentum balance ($m^2\ s^{-2}$) versus latitude, averaged over the last 10 years of the reference simulation. The upper plot shows the dominant terms and the overall sum. The lower plot shows the small magnitude terms (note the change in scale).

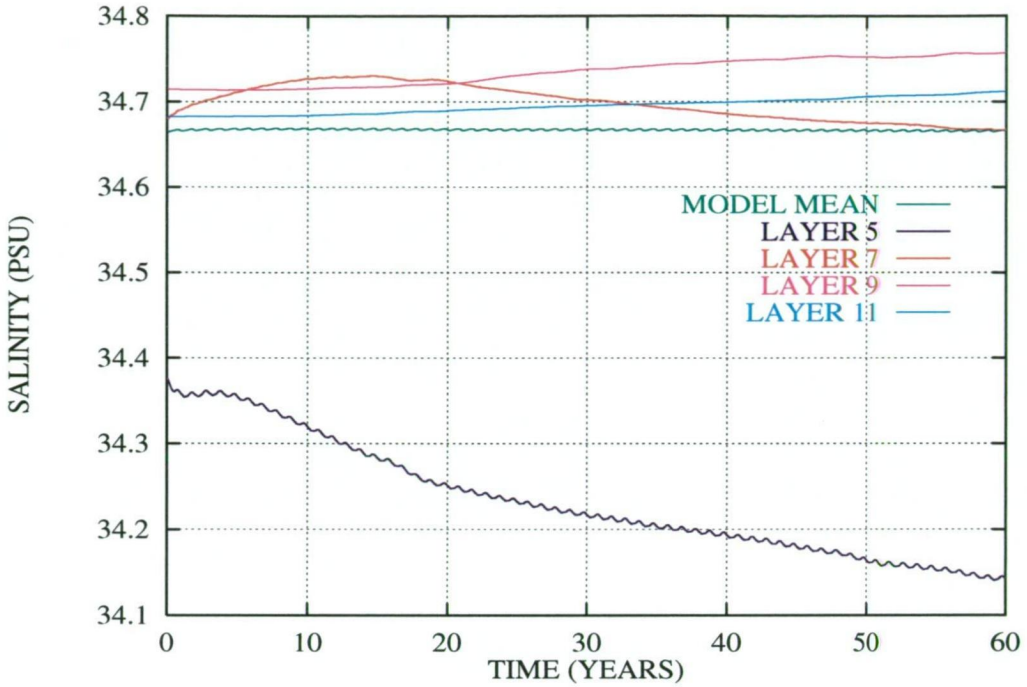

Fig. 3.12: Evolution of mean model salinity and selected layer mean salinities over the course of the reference simulation.

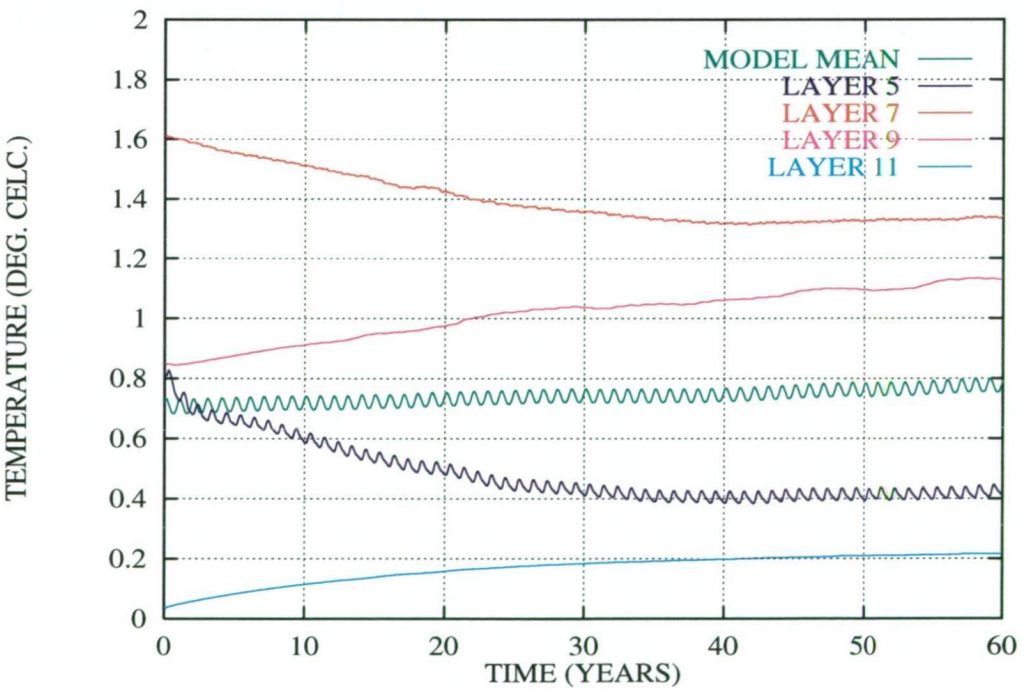

Fig. 3.13: Evolution of mean model potential temperature and selected layer mean temperatures over the course of the reference simulation.

0.01 °C/decade, which is considered to be small for the purpose of the experiments considered. A further strengthening in the trend at depth towards increased salinity is provided by the brine rejection mechanism at the surface and subsequent convection. In the pycnocline (e. g. layer 7; 400–900 m) and near the surface (e. g. layer 5; 100–200 m) it appears that the surface forcing is playing the dominant role. The trend is for these waters to cool during the first half of the integration, after which the layer mean temperatures remain relatively stable. Layer 5 freshens throughout the simulation, as does layer 7 for the last 45 years. This freshening results from the high precipitation minus evaporation over the modelled region, the effects of which are discussed in more detail in Section 4.3.

The model ocean's mean meridional thermohaline state over the final 10 years of the simulation is shown in Figure 3.14 (salinity) and Figure 3.15 (temperature). These zonally integrated sections may be compared with the initialisation states shown in Figures 3.3 and 3.4 respectively. It can be seen that there is considerable freshening and cooling in the upper 1000 m of the southern half of the model. Once again, this is related to the high surface fresh water flux and the increasing stability of the mixed layer that this implies. The isotherms have also become noticeably more level below 1000 m, suggesting that the model has become well mixed in the horizontal in the absence of any external oceanic interaction from beyond the artificial northern boundary.

Figure 3.16 shows an instantaneous picture of the model's surface layer salinity during the sea-ice growth period in the final year of the reference simulation. Generally, the sea surface salinity decreases as the latitude south increases. An exception to this pattern occurs immediately to the west of the Dibble Glacier Tongue (i. e. the topographic protrusion at 135°E, 65–66°S). Here a small source region of high sea surface salinity (above 34 psu) is found. In the next section it is shown that this is the location of a coastal polynya in the model, where the net annual sea-ice growth reaches

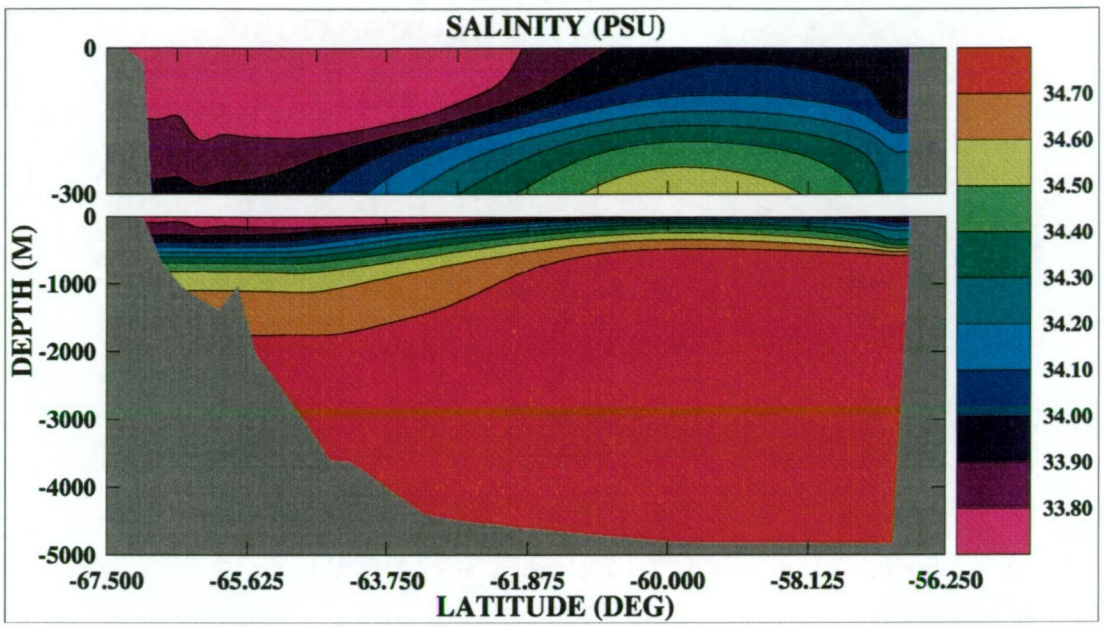

Fig. 3.14: Zonally averaged meridional section of model salinity, time averaged over the last decade of the reference simulation.

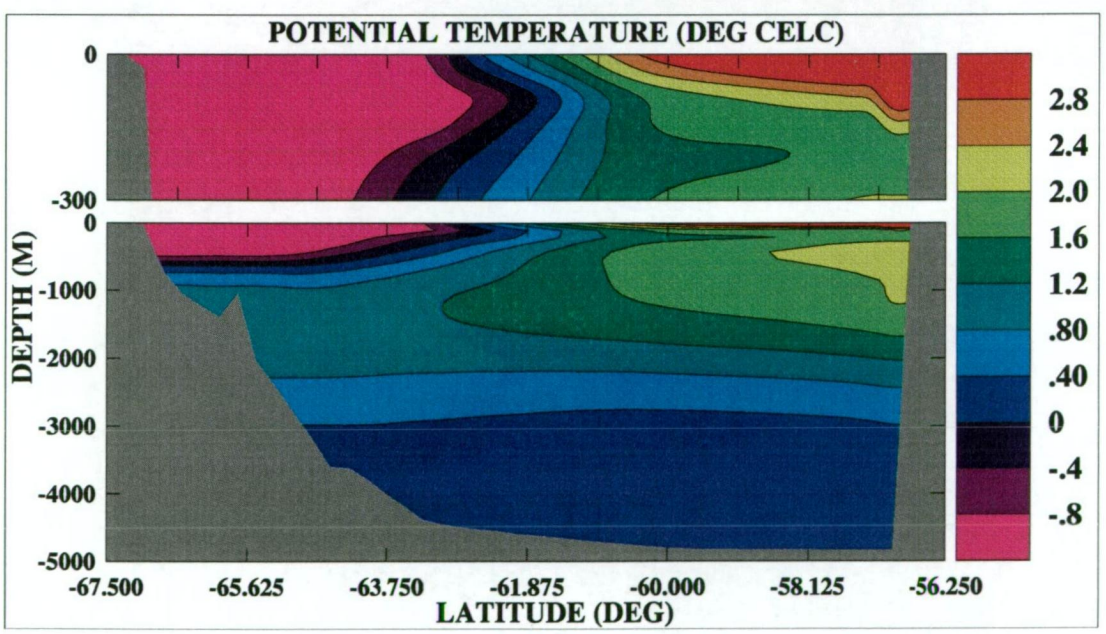

Fig. 3.15: Zonally averaged meridional section of model potential temperature, time averaged over the last decade of the reference simulation.

15 m a^{-1}. This amount of sea-ice growth results in a large salt flux to the shelf water, and the high shelf water salinity in turn contributes to the rate of intermediate and bottom water production. Rintoul (1998) suggests that waters along the coastline of East Antarctica may be the source of a significant proportion of global bottom water. He investigates the possibility that Adélie Land Bottom Water (ALBW) may account for as much as 25% of Antarctic Bottom Water in the global ocean. Such a high concentration of ALBW is attributed more to the long residence time of this water mass in the global circulation, rather than a high rate of bottom water production with respect to other regions such as the Weddell and Ross Seas.

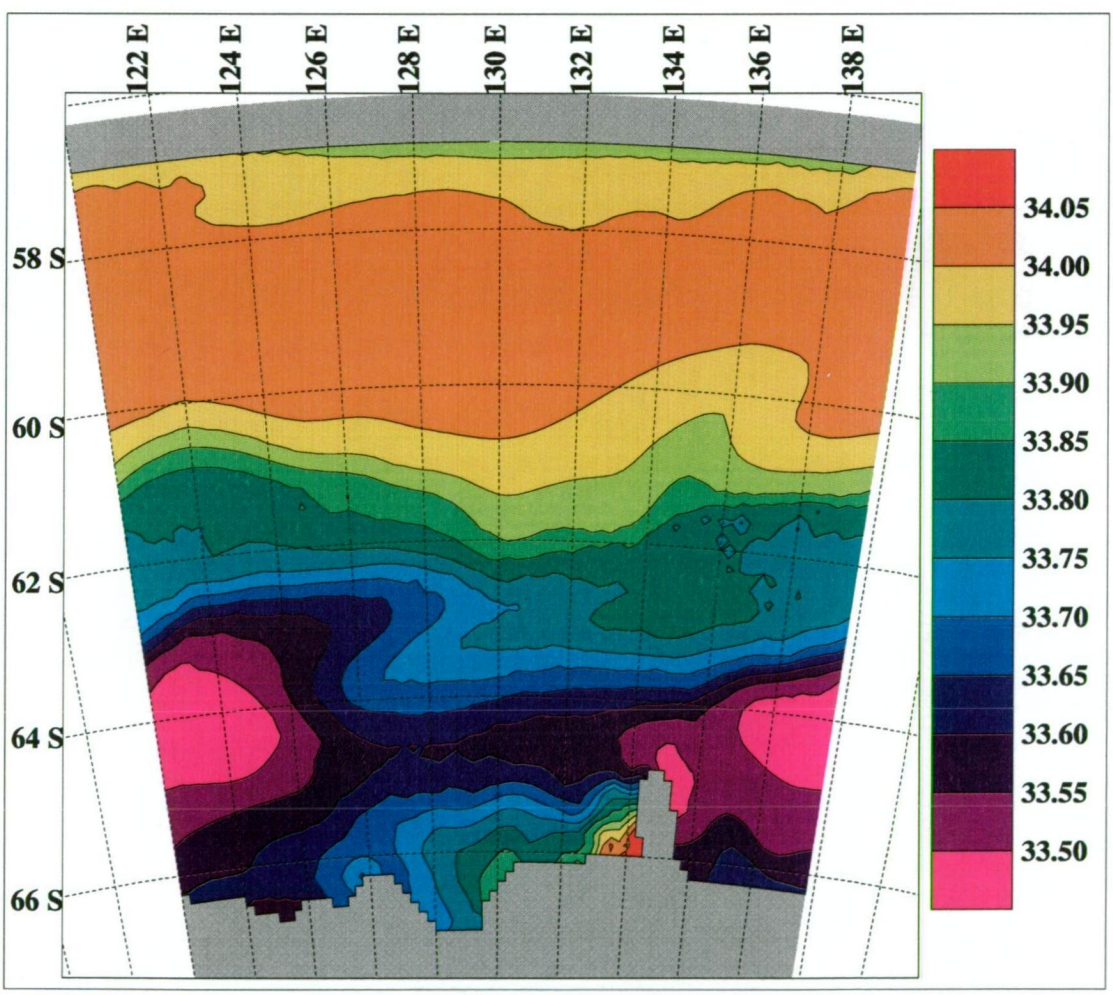

Fig. 3.16: Instantaneous sea surface salinity (psu) on June 15^{th} in Year 59 of the reference simulation.

3.3 Sea-Ice Model Response

Figure 3.17 shows the total sea-ice extent in square kilometres for the last 10 years of the 60 year reference simulation, and for comparison sea-ice extent from SSM/I satellite derived data corresponding to the model domain from January 1988 to April 1994. For the model output sea-ice extent is defined as the sum of the areas of grid cells containing sea-ice with concentration greater than a minimum of 15%, and similarly for the SSM/I data as the sum of the areas of pixels containing sea-ice with concentration greater than a minimum of 15%. Interannual variability in the satellite data is large when considering the variations in maximum sea-ice extent from year to year. In contrast, there is very little interannual variation of maximum sea-ice extent in the model, due to the annual repeat cycle of mean monthly atmospheric forcing data used. The observations suggest less variability in the minimum extent, which is overestimated by about 25% each year in the model. Figure 3.18 shows the same observational data and model output as in Figure 3.17, but averaged onto a seasonal cycle. As can be seen the phase of maxima and minima in the model precedes the observations by about 1 month.

The spatial distributions of mean monthly sea-ice compactness, sea-ice thickness, and snow thickness for the final decade of the control simulation are shown in Figures 3.19, 3.20 and 3.21 respectively. The most striking feature in these pictures is the coastal polynya that occurs in the lee of the Dibble Ice Tongue that protrudes from the coastline near 135°E. Wind-induced coastal polynyas around Antarctica are believed to be major areas of sea-ice production and sites of possible bottom water formation. However, because of their remoteness and inaccessibility, little is known about them beyond their distribution as derived from satellite observation.

The modelled sea-ice compactness is very high (90–100%) almost everywhere during the months April to October inclusive, with the exception of

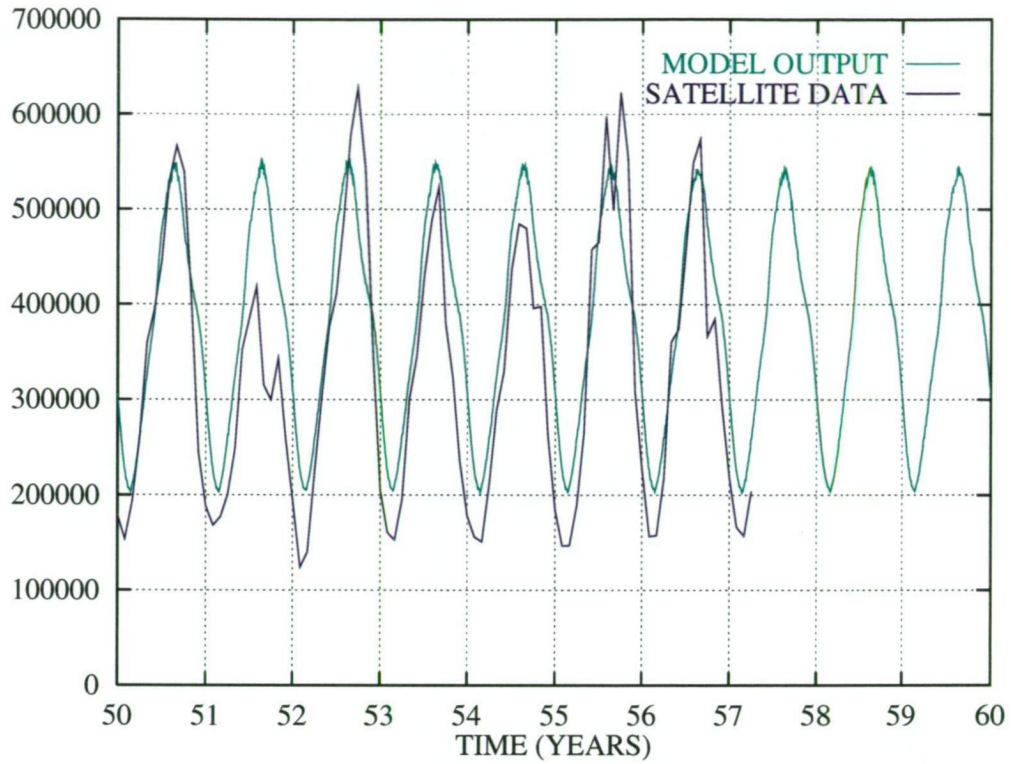

Fig. 3.17: Total sea-ice covered area (km^2) for the last 10 years of the reference simulation (green curve), compared with SSM/I data for the 7 years from 1988 to 1994 (blue curve) corresponding to the model domain.

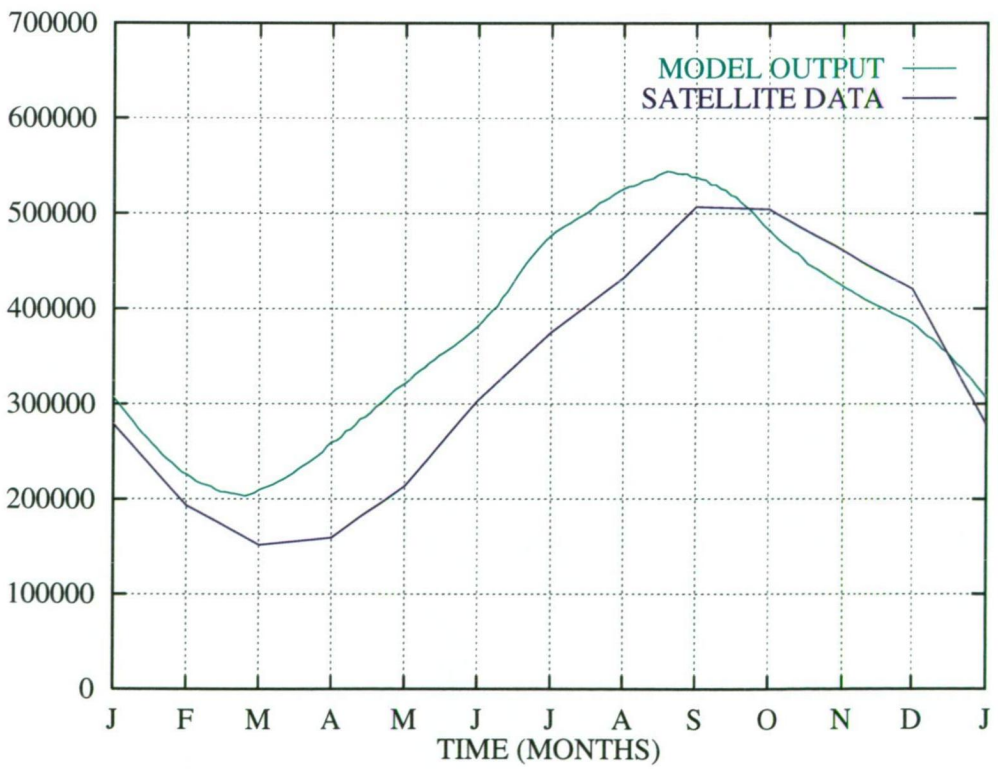

Fig. 3.18: As in Figure 3.17 but averaged onto a seasonal cycle.

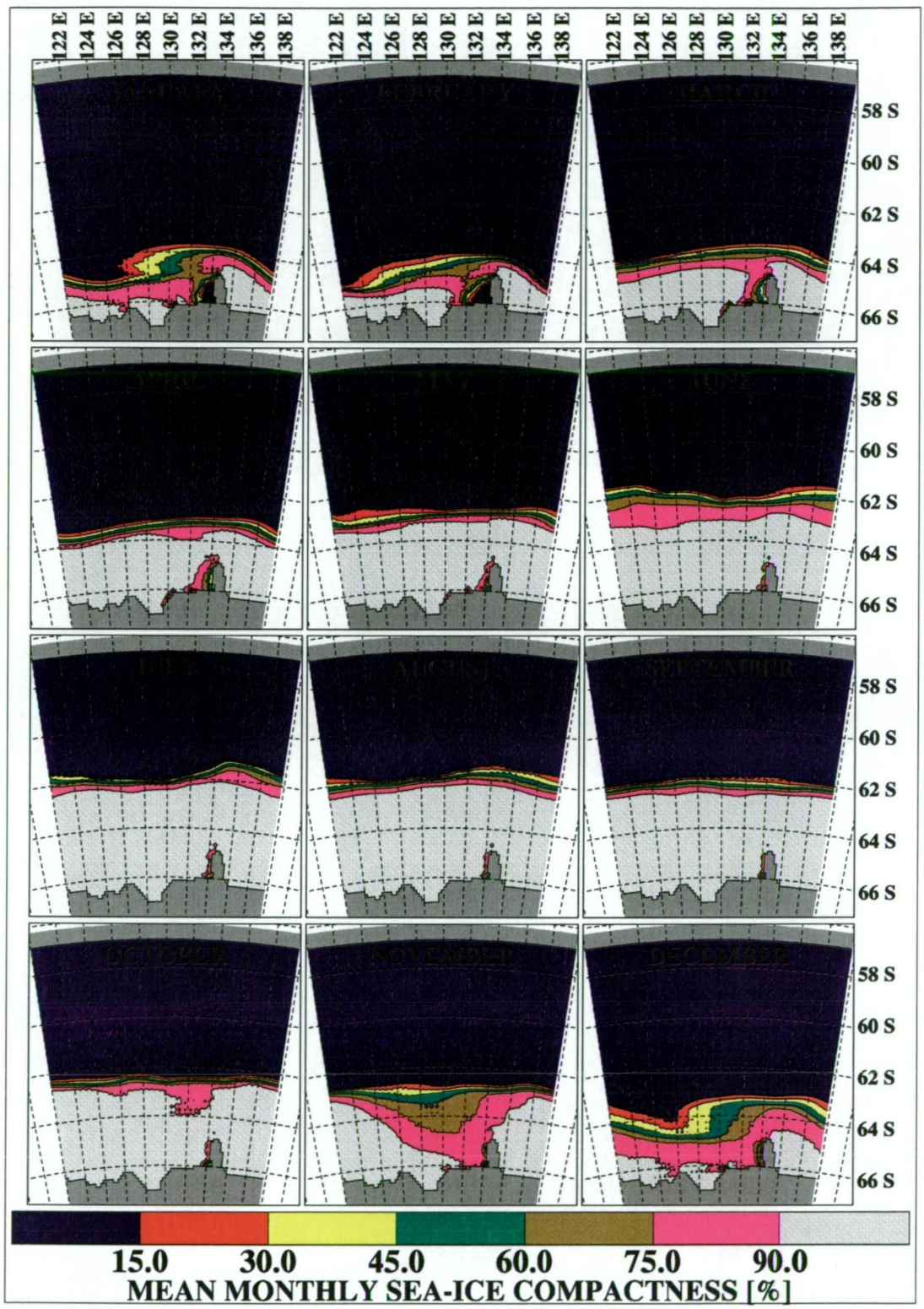

Fig. 3.19: Mean monthly sea-ice compactness averaged over the last 10 years of the reference simulation.

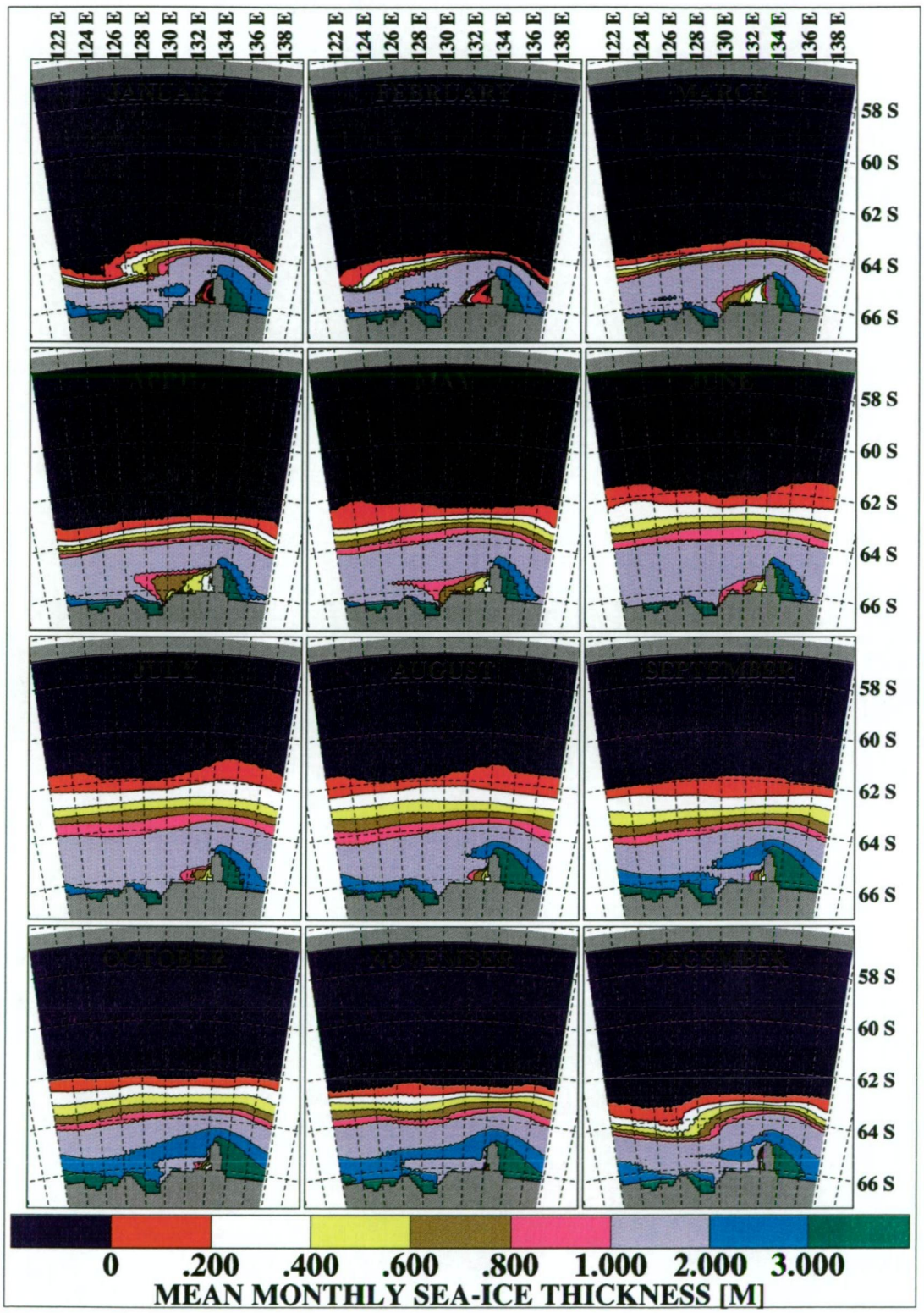

Fig. 3.20: Mean monthly sea-ice thickness averaged over the last 10 years of the reference simulation.

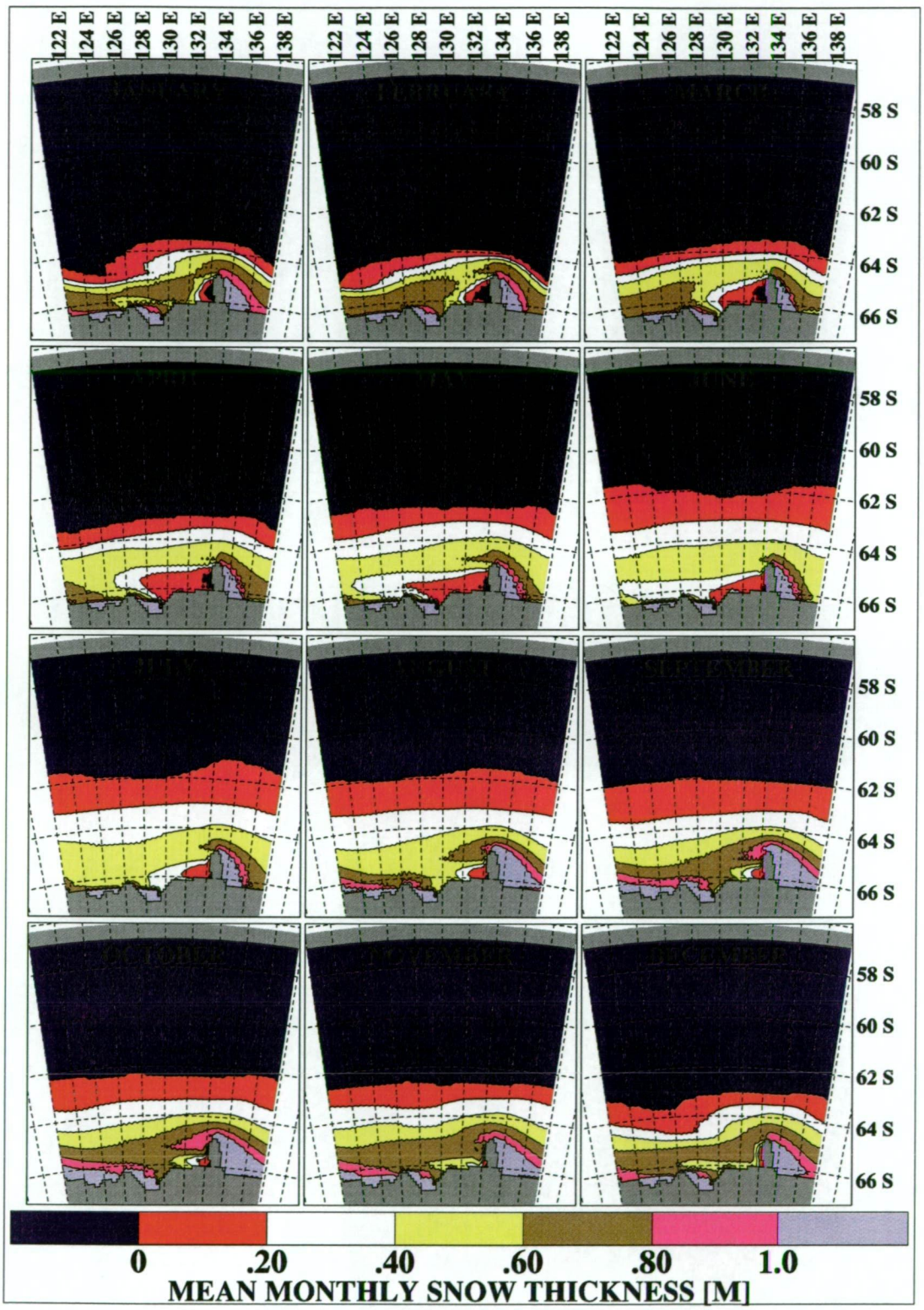

Fig. 3.21: Mean monthly snow thickness averaged over the last 10 years of the reference simulation.

the northernmost marginal sea-ice zone and in the vicinity of the coastal polynya. This is in contrast to SMMR satellite based observations which indicate a value around 80% (Gloerson *et al.*, 1992). However, there is some evidence suggesting that the standard satellite data processing algorithms do not detect much of the thin sea-ice in the Southern Ocean (Comiso *et al.*, 1997). An analysis of ship-based observations for east Antarctica shows that the mean ice concentration in August is as high as 93% (Worby *et al.*, 1998). In the atmosphere/sea-ice modelling study by Wu *et al.*, (1998), winter sea-ice concentrations for the Southern Ocean were reported to average 90%.

In general the modelled sea-ice thickness is above 1 m to the south of 64°S, except within the coastal polynya. This is somewhat thicker than the mean thickness of the sea-ice pack estimated from the limited observations available (e.g. Worby and Wu, 1998; Worby et al., 1998). These observations suggest that the large-scale mean thickness of East Antarctic sea-ice is generally below 1 m. Also the sea-ice cover persists throughout the year in this region, where the model bathymetry consists of the steep continental slope and the continental shelf (see Figure 3.2). Thicker sea-ice (above 3 m) banks up via dynamical processes on the eastern side of the Dibble Ice Tongue, and on the western coastline of Porpoise Bay. As each winter cycle progresses the embankment of sea-ice against the ice tongue extends further east, eventually crossing the model's periodic boundary for the months August through November. North of 64°S the modelled sea-ice is less than 1 m in thickness. This is the model's seasonal sea-ice zone and is situated over deep ocean. The distribution of snow thickness is similar to that of sea-ice thickness. Snow thickness above 1 m is found in regions where thick sea-ice (above 3 m) occurs. South of 64°S the snow thickness is generally above 0.4 m, and in the seasonal zone to the north of this is below 0.4 m.

Figure 3.22 shows the net annual *in situ* thermodynamic sea-ice growth, sea-ice melt, and sea-ice growth minus melt. In the coastal polynya the

maximum sea-ice growth is over 15 m, with above 3 m of growth being typical of a triangular region having sides of approximately 100 km in length, extending from 132–134°E and from 65–66°S. Sea-ice production in the coastal polynya, and sea-ice transport out of the coastal polynya, result in a region from 124–130°E and from 62.5–64.5°S where the net annual *in situ* thermodynamic response is negative, i. e. in the annual average sea-ice melts here. Over most of the remainder of the modelled region net sea-ice growth minus melt is less than 0.5 m.

Figure 3.23 shows streamlines of mean monthly sea-ice velocity also averaged over the final decade of the reference simulation. The modelled sea-ice in general moves from east to west, although this pattern is perturbed by the presence of the Dibble Ice Tongue. Sea-ice is also always advected away from the coastal polynya. The zonally averaged mean monthly zonal sea-ice velocities for the corresponding period are shown in Figure 3.24. The zonal velocity magnitude is greatest near 63.5°S for the months May to October inclusive, where it attains peak values in excess of 0.16 m s^{-1} from east to west. This corresponds to just inside the seasonal sea-ice zone, as discussed above with respect to the sea-ice thickness. The peak September value is approximately 0.2 m s^{-1}, and the channel is 990 km long at 63.5°S, so sea-ice travelling with this zonal velocity will take about 57 days to cross the model domain from east to west.

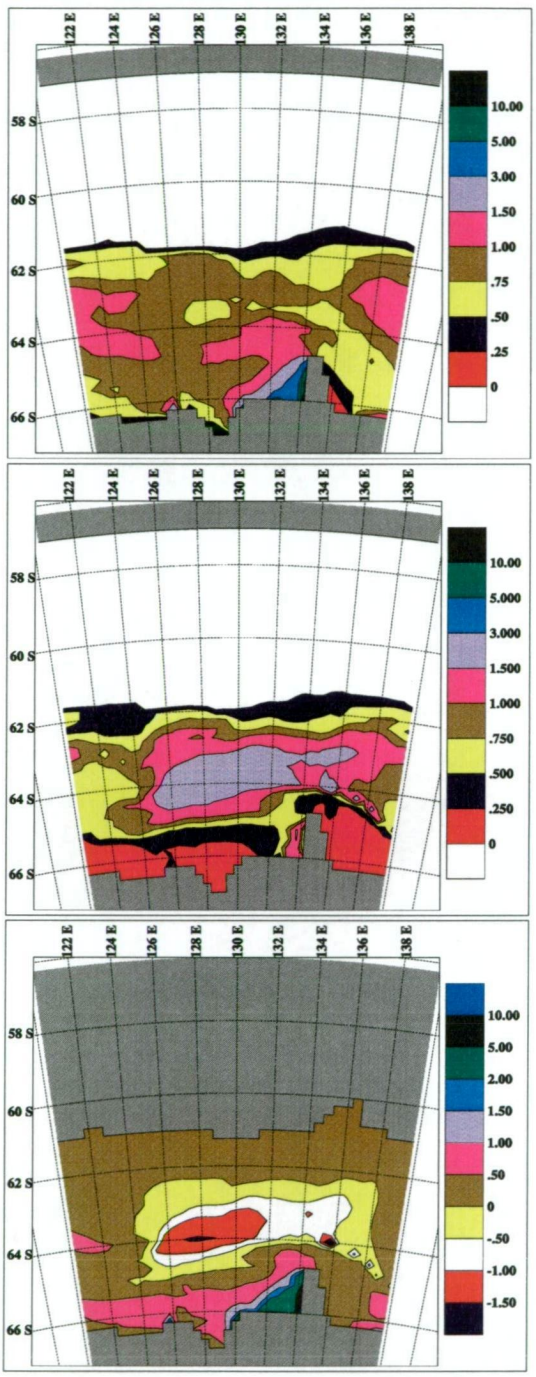

Fig. 3.22: Contours of net annual *in situ* sea-ice growth (top), net annual *in situ* sea-ice melt (middle), and net annual *in situ* growth minus melt (bottom). Values are averaged over the final decade of the reference simulation and expressed in meters.

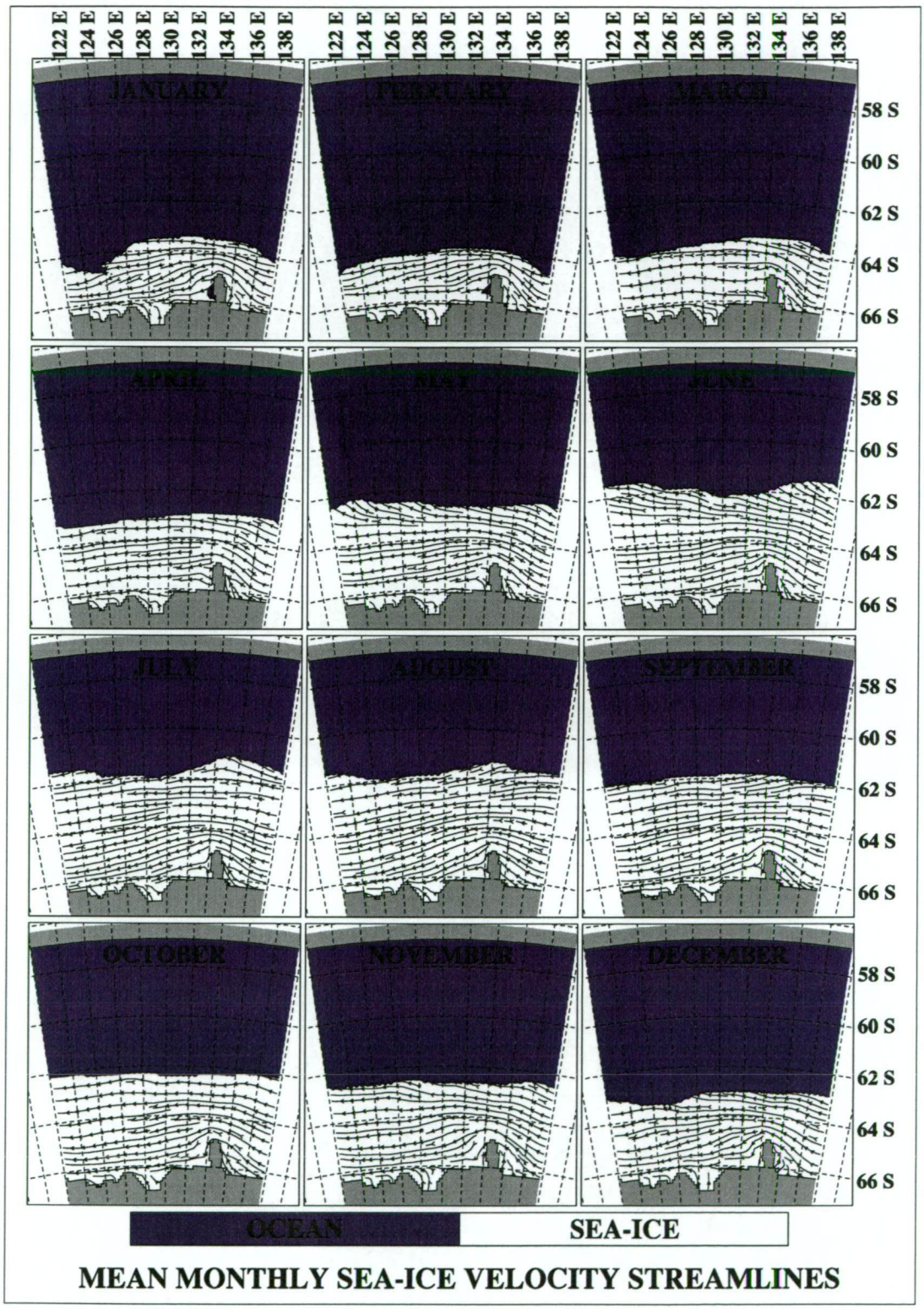

Fig. 3.23: Streamlines of mean monthly sea-ice velocity averaged over the last 10 years of the reference simulation.

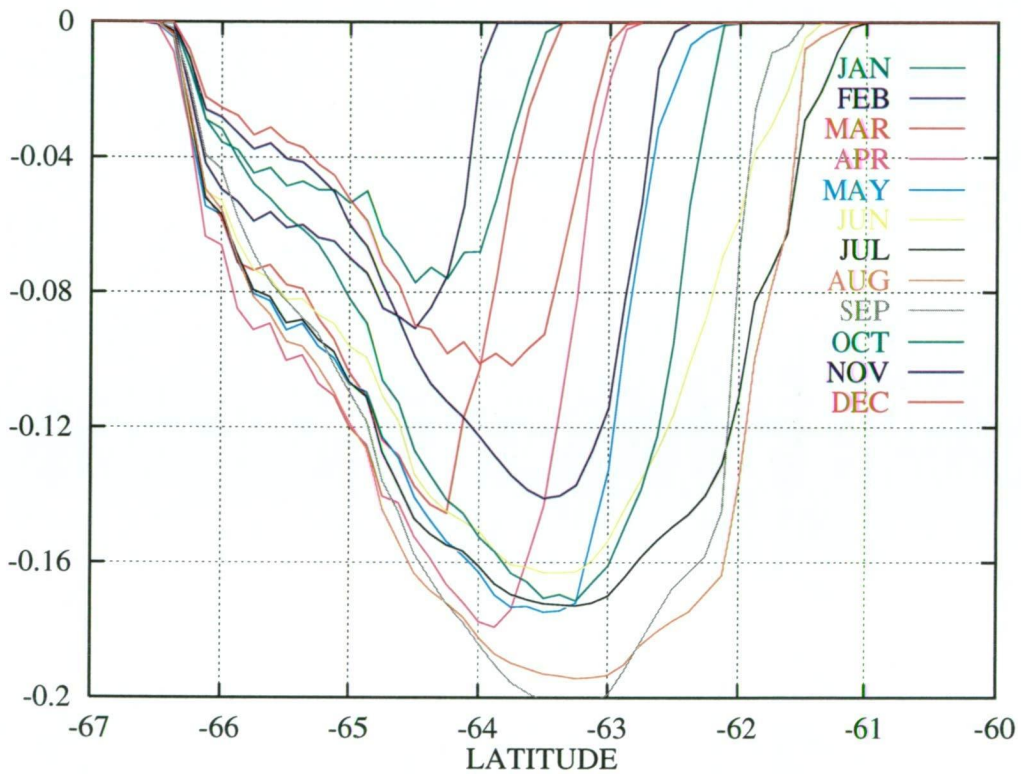

Fig. 3.24: Zonally integrated mean monthly zonal sea-ice velocity (m s^{-1}) averaged over the last 10 years of the reference simulation.

3.4 Oceanic Heat Flux

The greatest unknown in the thermodynamic balance governing sea-ice growth and melt in the Southern Ocean is the oceanic heat flux to the base of the sea-ice. For the relatively stable Arctic Ocean an oceanic heat flux of around 2 W m^{-2} has generally being used in sea-ice modelling studies (Maykut and Untersteiner, 1971; Parkinson and Washington, 1979; Wu *et al.*, 1997). Models of the atmosphere/sea-ice system in the Southern Hemisphere have shown that the sea-ice thickness and areal coverage is very sensitive to the oceanic heat flux (Parkinson and Washington, 1979; Wu *et al.*, 1998). Although varying estimates have been made as to the magnitude of the oceanic heat flux, little is known about its seasonality, with the exception of the work by Heil *et al.* (1996), where seasonal estimates are calculated for landfast ice.

A variety of indirect methods have been used to estimate the oceanic heat flux in the Southern Ocean. Gordon (1981), using mean monthly climatologies of sea surface temperature, air temperature, dew point temperature, wind speed and cloud cover for the 60–70°S latitude band, calculates a mean annual sea to air heat exchange of 31 W m^{-2}. Gordon and Huber (1990) estimate the entrainment rate of Weddell Deep Water into the mixed layer using observed oxygen concentrations. They find that the associated vertical heat flux averages 41 W m^{-2} during the active winter entrainment period. For individual hydrographic stations this value is as high as 100 W m^{-2}. Assuming a summer heat flux of 2 W m^{-2} due to vertical diffusion of heat they conclude that the mean annual oceanic heat flux for the area is 16 W m^{-2}. Martinson (1993) balances sea-ice thickness and divergence measurements with air/sea heat exchange to obtain a minimum for oceanic heat flux in the Weddell Sea of 19 W m^{-2}.

Several attempts at direct measurement of oceanic heat flux have been made in the Southern Ocean. Lytle and Ackley (1996) report on measure-

ments made during the first half of 1992 in the western Weddell Sea as part of the Ice Station Weddell experiment. They found the oceanic heat flux measurements averaged 7±2 W m^{-2}. Direct measurement of oceanic heat flux was also attempted in the Antarctic Zone Flux Experiment carried out in the Eastern Weddell Sea during July–August 1994 (McPhee *et al.* 1996). During an observed atmospheric storm event, the measured upward oceanic heat flux reached 100 W m^{-2} over a warm water anomaly in the pycnocline. Where the mixed layer was both cooler and deeper, the ocean heat flux was 25 W m^{-2}. A wintertime (August) oceanic heat flux of around 15 W m^{-2} was found in a study (near 140°E, 65°S) by Lytle *et al.* (1999). Unfortunately, available measurements are sparse in both time and space. However they do point out that large variations in upper ocean temperature structure, and hence in vertical oceanic heat flux, do exist.

Coupled ocean/sea-ice modelling can give valuable insight into the spatial and temporal variability of the oceanic heat flux and the processes responsible for controlling it. Few attempts have been made to explicitly calculate oceanic heat flux in the Southern Ocean. Lemke *et al.* (1990) coupled a dynamic thermodynamic sea-ice model to a one-dimensional mixed-layer/pycnocline ocean model, and applied it to the Weddell Sea region. They found the oceanic heat flux to have a mean of around 3 W m^{-2}. A similar study by Stössel *et al.* (1990) for the entire Southern Ocean gives the same basic result. These studies did not incorporate the full complexity of the ocean's dynamic and thermodynamic circulation. The first Antarctic ocean/sea-ice model to include a full three-dimensional ocean was that of Häkkinen (1995). That study shows the ocean heat flux to be highly spatially variable, with local annual means ranging from 0 to 100 W m^{-2}. As numerical models become increasingly sophisticated and of higher resolution one expects that the corresponding calculations of oceanic heat flux will become more accurate.

For the purpose of this study, oceanic heat flux, Q_{net}, is defined to

be the heat made available by oceanic processes to the upper layer of the model ocean. The oceanic heat has three sources: heat due to convective over-turning, Q_{con}; heat due to vertical diffusion, Q_{dif}; and heat due to the three-dimensional advection of the ocean's thermal field, Q_{adv}.

$$Q_{net} = Q_{con} + Q_{dif} + Q_{adv} \tag{3.1}$$

Convective over-turning occurs when an unstable density stratification exists at a vertical column within the ocean, i. e. when heavier (more dense) water overlies lighter water. Ignoring the effects of salinity, colder water is more dense than warmer water. Ignoring the effects of temperature, saltier water is more dense than fresher water. Simulation of convective processes in the HOPE model involves the uniform mixing of potential temperature and salinity in any two vertically adjoining grid cells that exhibit density instability. i. e.

$$\Theta_{i,j,k} = \Theta_{i,j,k+1} = \frac{\Delta z_{i,j,k}\Theta_{i,j,k} + \Delta z_{i,j,k+1}\Theta_{i,j,k+1}}{\Delta z_{i,j,k} + \Delta z_{i,j,k+1}} \tag{3.2}$$

$$S_{i,j,k} = S_{i,j,k+1} = \frac{\Delta z_{i,j,k}S_{i,j,k} + \Delta z_{i,j,k+1}S_{i,j,k+1}}{\Delta z_{i,j,k} + \Delta z_{i,j,k+1}} \tag{3.3}$$

Here $\Delta z_{i,j,k}$ is the thickness, $\Theta_{i,j,k}$ is the potential temperature and $S_{i,j,k}$ the salinity of the grid cell in layer k having longitudinal index i and latitudinal index j. Note that for convection in the model, as with all mixing processes, the thickness of the upper layer is modified to account for sea surface elevation and sea-ice draft (see Equation 2.33).

Vertical eddy diffusion of the thermohaline fields is calculated using an implicit time discretisation, with Gaussian elimination and back substitution, to solve the eddy diffusivity equations:

$$\frac{\partial \Theta}{\partial t} = D_V \frac{\partial}{\partial z}\left(\frac{\partial \Theta}{\partial z}\right) \tag{3.4}$$

$$\frac{\partial S}{\partial t} = D_V \frac{\partial}{\partial z}\left(\frac{\partial S}{\partial z}\right) \tag{3.5}$$

Three-dimensional advection of potential temperature and salinity includes the small effects of horizontal eddy diffusivity by use of a constant

coefficient harmonic operator. i. e.

$$\frac{\partial \Theta}{\partial t} = -u\frac{\partial \Theta}{\partial x} - v\frac{\partial \Theta}{\partial y} - w\frac{\partial \Theta}{\partial z} + D_H \nabla^2 (\Theta) \tag{3.6}$$

$$\frac{\partial S}{\partial t} = -u\frac{\partial S}{\partial x} - v\frac{\partial S}{\partial y} - w\frac{\partial S}{\partial z} + D_H \nabla^2 (S) \tag{3.7}$$

The advection scheme is solved using a predictor-corrector method.

The terms on the right hand side of Equation 3.1 are then evaluated as

$$Q_{con} = \rho_O c_w \frac{\Delta \Theta_{con}}{\Delta Z} \tag{3.8}$$

$$Q_{dif} = \rho_O c_w \frac{\Delta \Theta_{dif}}{\Delta Z} \tag{3.9}$$

$$Q_{adv} = \rho_O c_w \frac{\Delta \Theta_{adv}}{\Delta Z} \tag{3.10}$$

Here $\Delta\Theta_{con}$, $\Delta\Theta_{dif}$, and $\Delta\Theta_{adv}$, are the temperature changes in the upper layer of the model ocean resulting from Equation 3.2 for the case of convection, from Equation 3.4 for the case of diffusion, and from Equation 3.6 for the case of advection. ΔZ is the thickness of the upper model layer, accounting for sea-ice draft and sea surface elevation.

Figure 3.25 shows the seasonal variation in the areal mean of the net oceanic heat flux. Oceanic heat flux has been calculated every second day throughout the model run and then averaged onto an annual cycle for the last decade of the simulation. The annual cycle was then smoothed using a 10 day running mean. The annual mean net oceanic heat flux is 8.1 W m^{-2}, with convective, diffusive and advective annual means of 5.6, 1.0 and 1.5 W m^{-2} respectively. It is clear that convection is the dominant process in determining the magnitude of the modelled oceanic heat flux for the months April–September inclusive. In the summer (November–February) advection dominates, while diffusion is fairly constant throughout the year. The areal-averaged wintertime oceanic heat flux peaks near 19 W m^{-2} in June, and is around 10–20 W m^{-2} during the period April–August. This is in reasonable agreement with the only direct observation of time averaged wintertime oceanic heat flux for the East Antarctic region of 15 W m^{-2} (Lytle *et al.*, 1999).

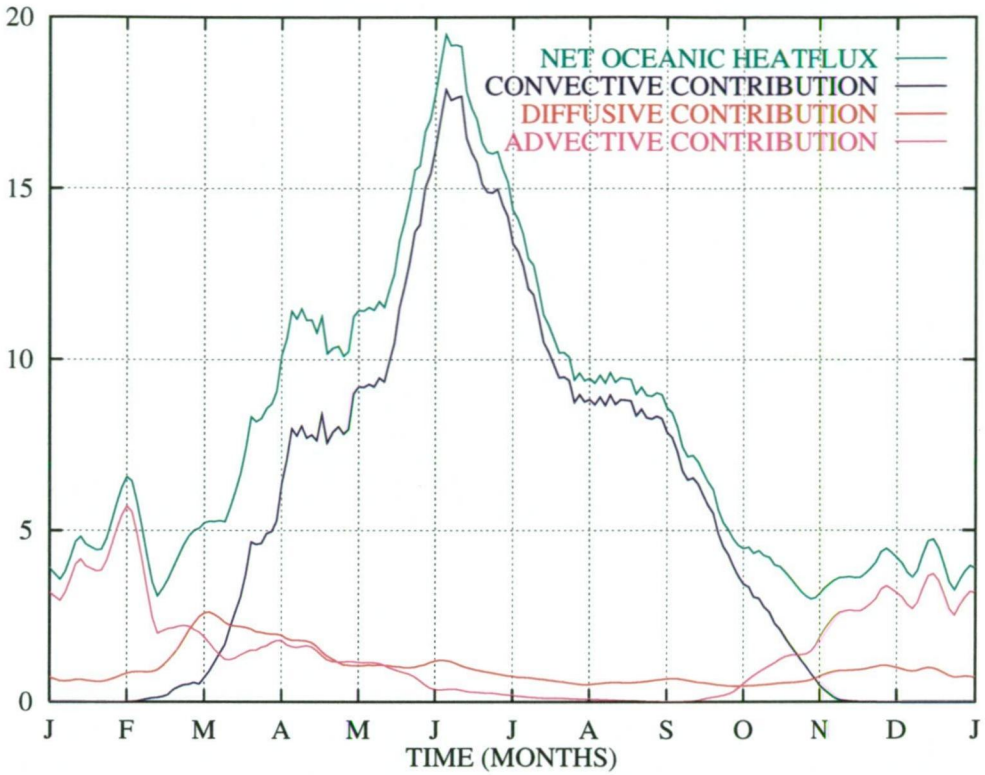

Fig. 3.25: Seasonal cycle of instantaneous areal-mean oceanic heat flux (W m^{-2}) averaged over the last 10 years of the 60 year reference simulation. Net oceanic heat flux is shown as a sum of convective, diffusive and advective heat fluxes. Convection dominates as a source of oceanic heat from April to September. The annual mean is 8.1 W m^{-2}.

The spatial variability in the mean monthly net oceanic heat flux for the last 10 years of the 60 year reference simulation is shown in Figure 3.26. The corresponding mean monthly convective, advective and diffusive contributions to *in situ* oceanic heat flux are shown in Figures 3.27, 3.28 and 3.29 respectively. Note that the scaling of contour intervals used in Figures 3.26 and 3.27 is different to that used in Figures 3.28 and 3.29. Also note that the areas of white north of the sea-ice zone are not indicative of general oceanic heat gain throughout the year in these regions, but have instead being excluded from the calculations of oceanic heat flux as sea-ice is never present

in these regions. That is, only the oceanic heat flux to the base of sea-ice is considered, and the time averaging is only over the period for which sea-ice is present. High values of net oceanic heat flux persist throughout the year near the sea-ice edge, due to convection in the winter months and both advection and diffusion in the summer months. The net flux of heat to the base of sea-ice is also relatively high in the coastal polynya region (133–134°E, 65–66°S) mainly due to convection in the model, although the advection becomes important here during the months December and January. Much of the advective heat provided at the sea-ice edge in the summer months is not from the deep ocean, but rather from atmospheric warming of the relatively fresh (and therefore vertically stable) surface waters immediately to the north of the sea-ice edge. Apart from near the sea-ice edge where mean monthly values can be above 100 W m^{-2}, within the coastal polynya where values approach 50 W m^{-2}, and in the seasonal zone (62–64°S) where values in the range 5–20 W m^{-2} are common in the winter months, for most of the year at most other locations the oceanic heat flux lies in the range of 0–5 W m^{-2}.

For completeness the annual mean net oceanic heat flux, along with the annual mean convective, advective and diffusive components of this flux, is shown in Figure 3.30. Once again it is clear that convection is dominant over both advection and diffusion in providing ocean heat to the base of the sea-ice. Also, apart from within the coastal polynya, it can be seen that the convection is only strong in the model's seasonal sea-ice zone. That is, north of approximately 64°S.

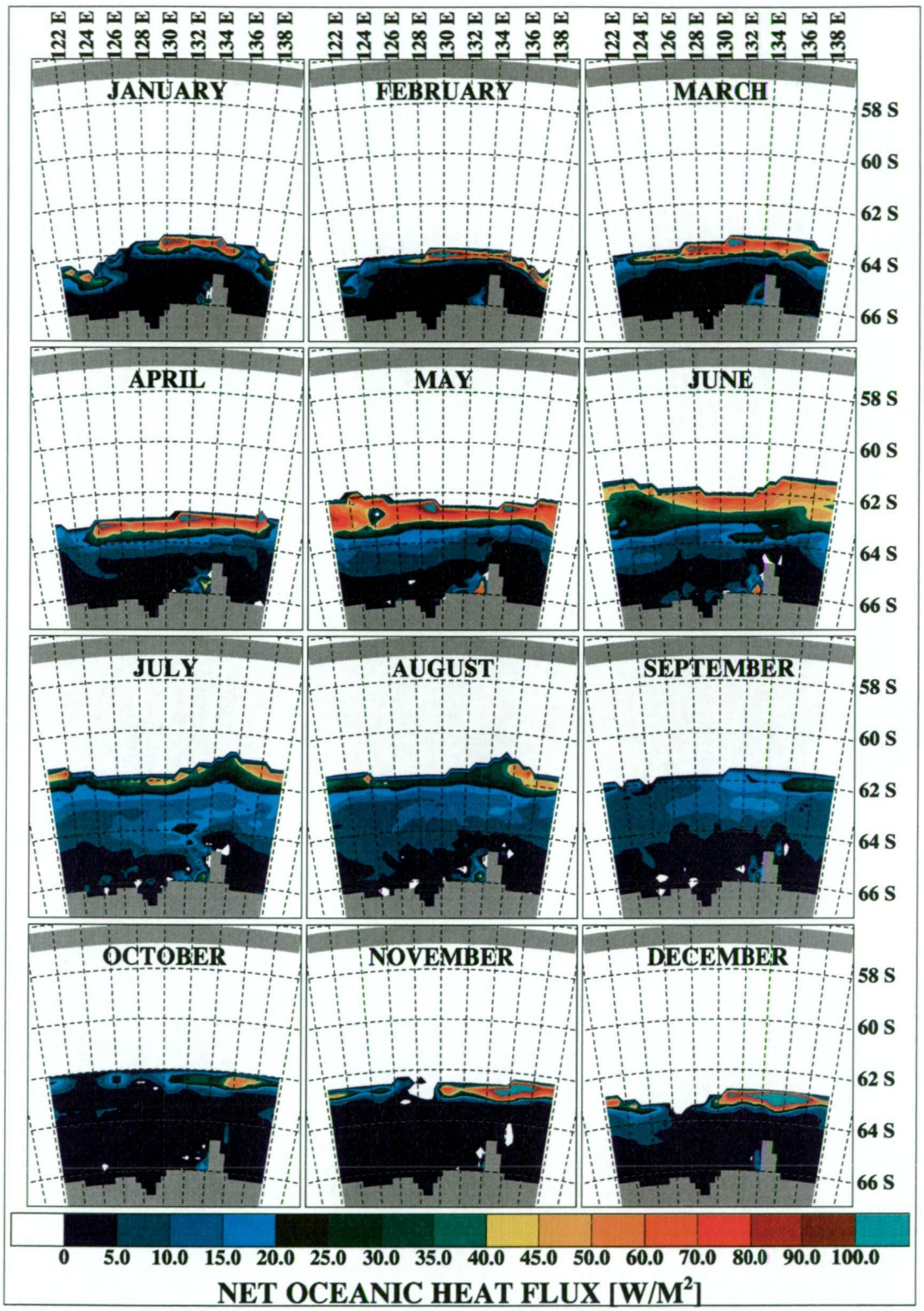

Fig. 3.26: Seasonal cycle of spatial distribution of net oceanic heat flux in W m^{-2}. Mean monthly values for each grid cell were determined using output from the last 10 years of the control simulation.

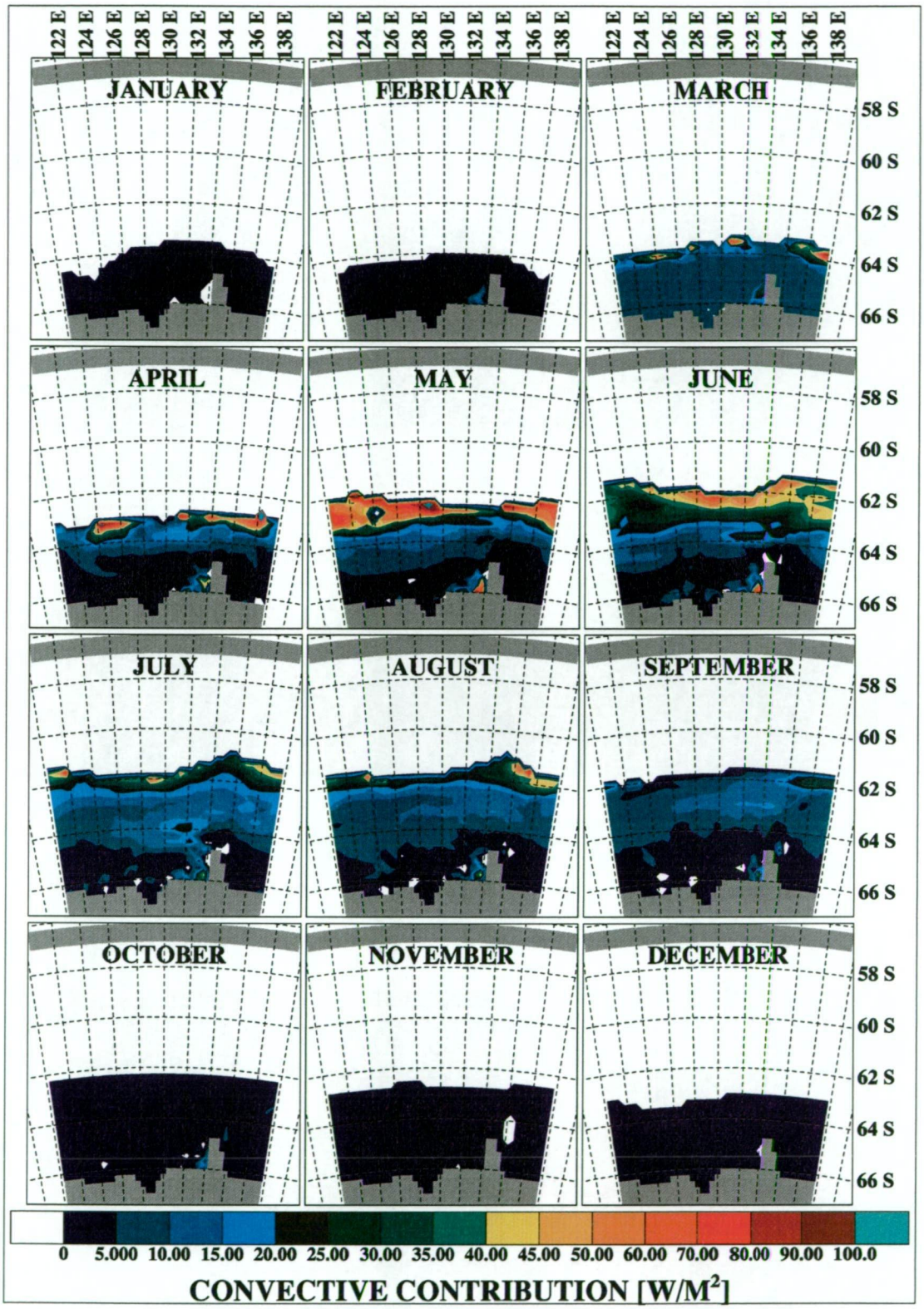

Fig. 3.27: As in Figure 3.26 but only for the convective contribution to net oceanic heat flux (W m^{-2}).

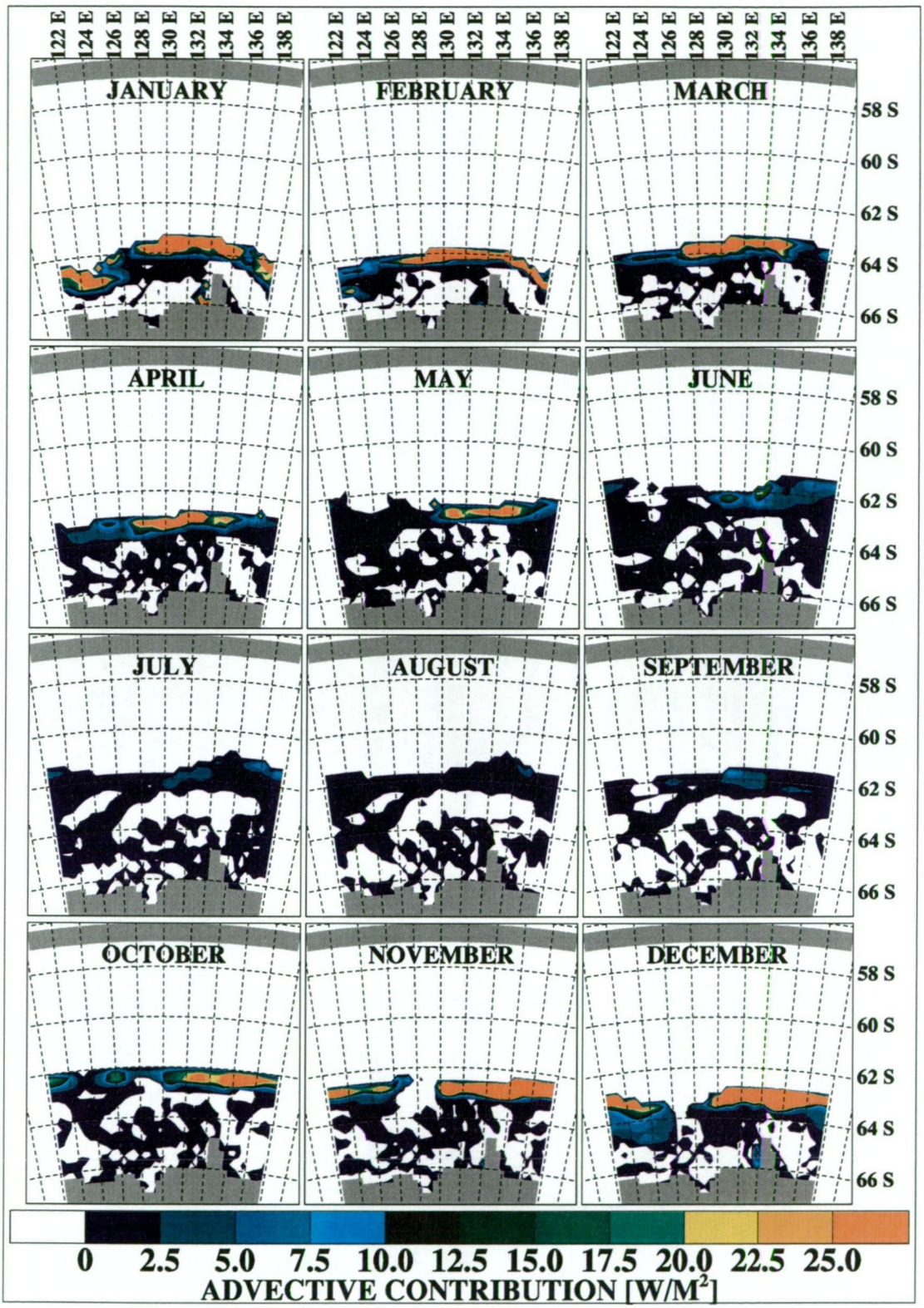

Fig. 3.28: As in Figure 3.26 but only for the advective contribution to net oceanic heat flux (W m^{-2}).

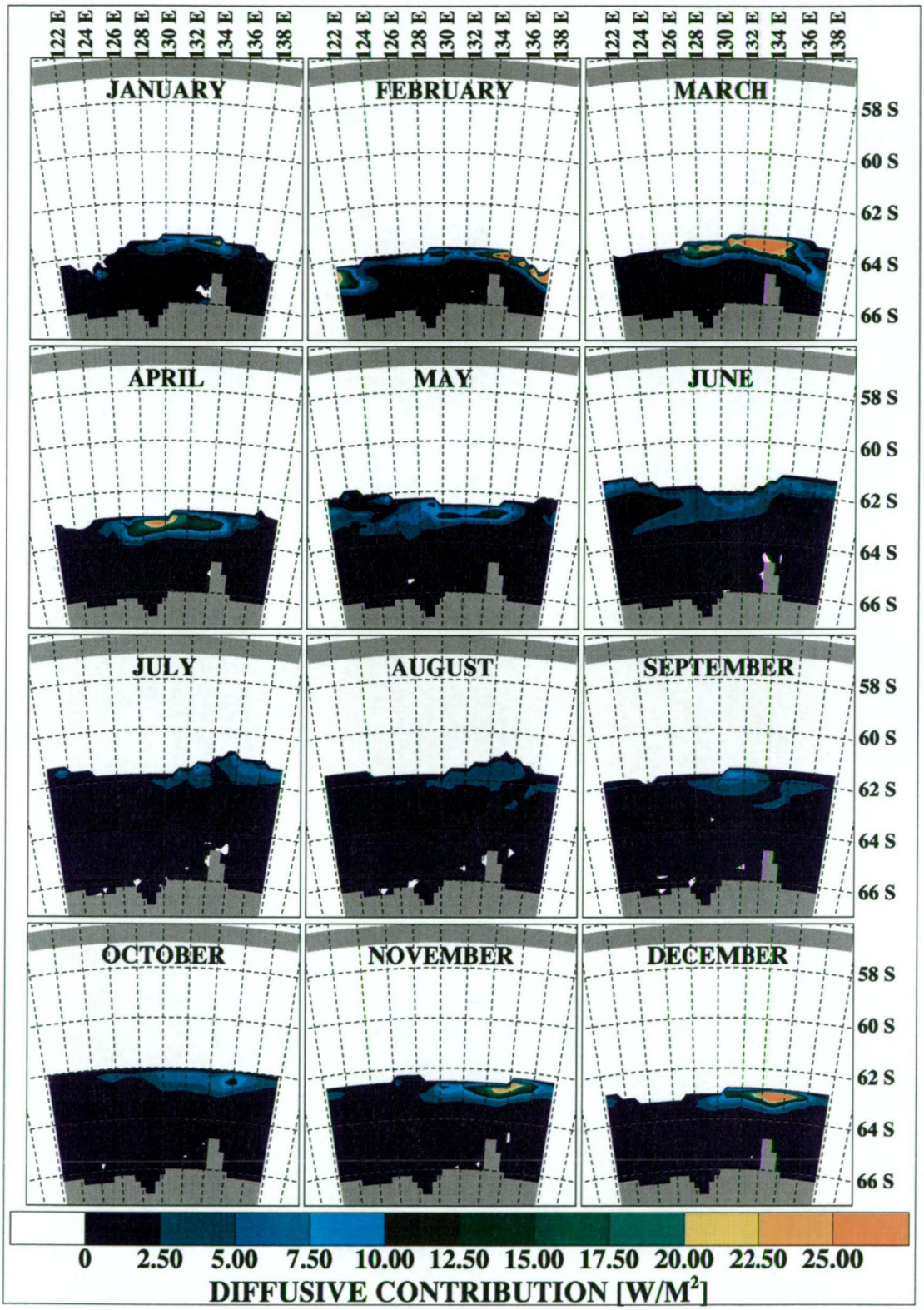

Fig. 3.29: As in Figure 3.26 but only for the diffusive contribution to net oceanic heat flux (W m^{-2}).

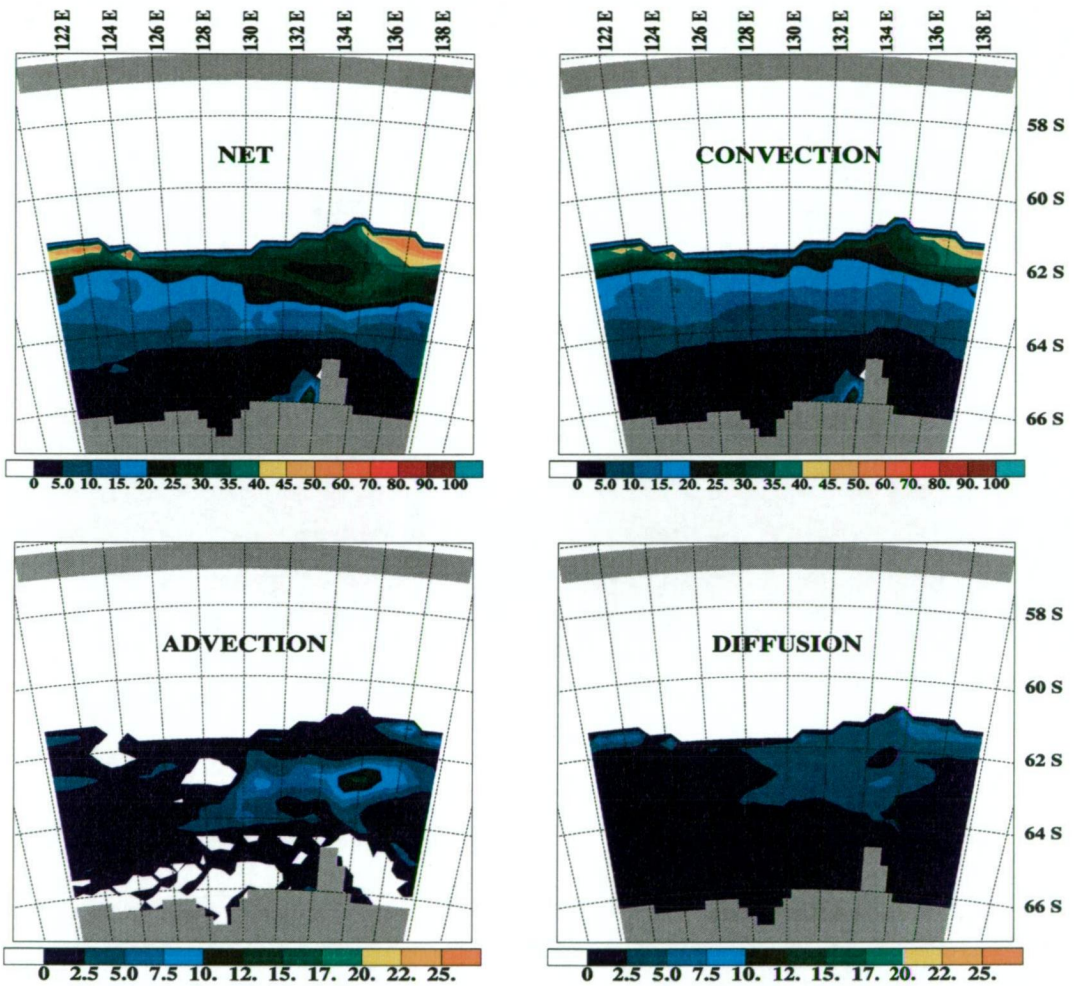

Fig. 3.30: Annual mean fields of oceanic heat flux (W m^{-2}), corresponding to the monthly mean fields of Figures 3.26 to 3.29.

4. SENSITIVITY EXPERIMENTS WITH THE HIGH-RESOLUTION MODEL

4.1 Sensitivity to a Doubling in Horizontal Resolution

This section focuses on the results from a 49 year simulation in which the only change to the model as discussed in Chapter 3 is a doubling of the horizontal resolution. This gives a resolution of $\frac{1}{8}^\circ$ in latitude and $\frac{1}{4}^\circ$ in longitude in each of the subgrids (odd/even) of the Arakawa E-grid, with an effective spacing (D in Figure 2.1) of 9.8 km at 60°S.

Figure 4.1 shows a timeseries of mass transport across the periodic boundary of the very high-resolution (hereafter VHR) simulation. The evolution of the model's mean zonal flow is similar to that in the high-resolution (hereafter REF) simulation as discussed in Section 3.2 (see Figure 3.5). A comparison between the REF and VHR runs for years 44 to 49 is shown in Figure 4.2. Both simulations exhibit the same strong barotropic response to the surface wind stress. The main difference in the intra-annual behaviour of the mass transport between the two simulations is the change from around -55 to -45 Sv in the maximum seasonal transport with the increase in horizontal resolution. The zonal momentum balance averaged over the last decade of the VHR simulation is shown in Figure 4.3. The curves of baroclinic and barotropic form stress (i. e. form stress and surface tilt in Figure 4.3 respectively) in VHR are somewhat smoother than in REF, but

as with the mass transport, the general pattern is similar between the two simulations. Once again a small *chequer-boarding* problem is evident in the horizontal Laplacian friction.

Figure 4.4 shows the seasonal cycle of area averaged net oceanic heat flux, along with the contributing terms, averaged over the last decade of the 49 year VHR simulation. Qualitatively, the area averaged convection is much smoother in the VHR run (c. f. Figure 3.25). The annual mean is 7.7 W m^{-2}, with the convective, diffusive and advective terms having annual means of 5.2, 1.4 and 1.1 W m^{-2} respectively. Thus, comparing with REF, the doubling in horizontal resolution produces a 5% decrease in the net oceanic heat flux. This is brought about by decreases of 7% and 26% in the convective and advective heat fluxes respectively, with an increase of 40% in the diffusive heat flux. The increase in diffusion and decrease in convection in the VHR simulation indicates that slightly greater vertical

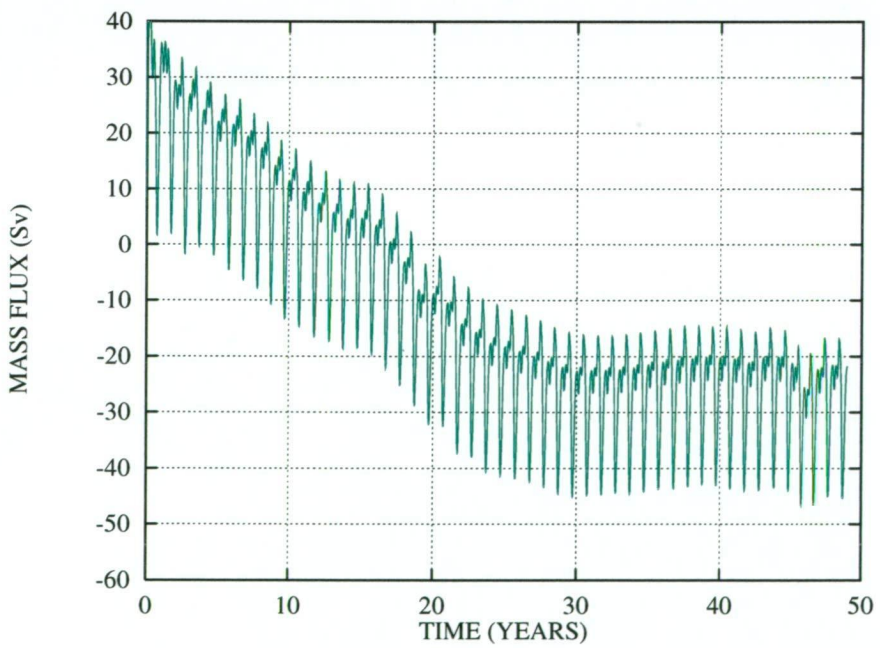

Fig. 4.1: Mass transport (Sv) across the periodic east-west boundary of the ocean model for the 49 years of the very high-resolution (VHR) simulation.

stability is obtained with increased horizontal resolution.

As there is little difference between the REF and VHR simulations the sensitivity experiments in the remainder of this chapter have been run using the more computationally economical lower resolution version. However, it should be pointed out that the mesoscale behaviour in the VHR version alters significantly when the Laplacian formulation of viscosity is replaced with the higher order biharmonic form. Biharmonic friction has the advantage of being scale selective, i. e. viscosity damping is greater for the biharmonic formulation at small scales, and significantly reduced on larger scales with respect to the lower order harmonic form (Holland, 1978). Such scale selectivity has led to biharmonic friction being the preferred method in eddy-resolving numerical ocean simulations (e. g. Semtner and Chervin, 1988; Webb *et al.*, 1998). Figure 4.5 shows a typical picture of instantaneous

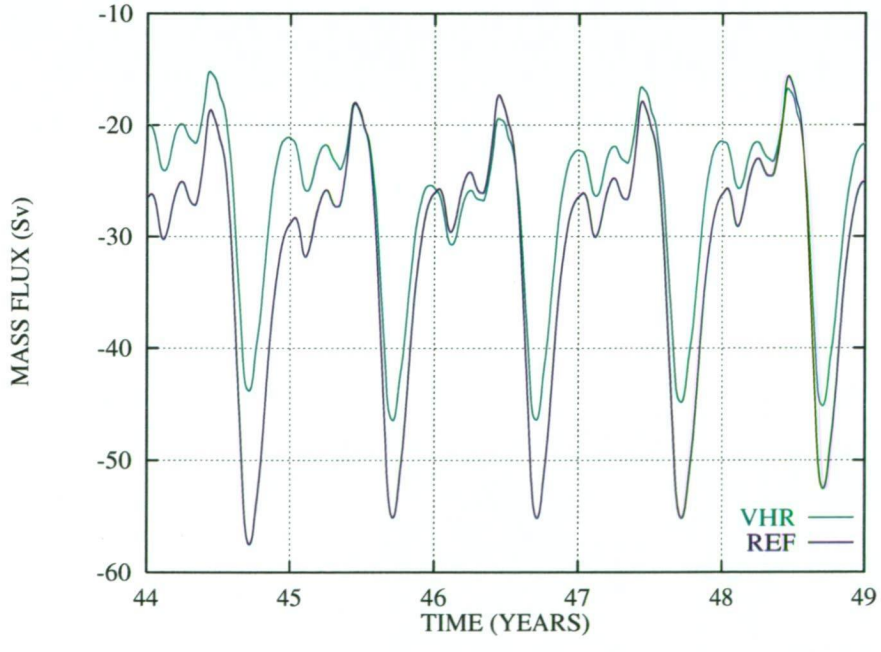

Fig. 4.2: Mass transport (Sv) across the periodic east-west boundary of the ocean model for the last 5 years of the VHR simulation, and for the corresponding period in the high-resolution (REF) simulation of Chapter 3.

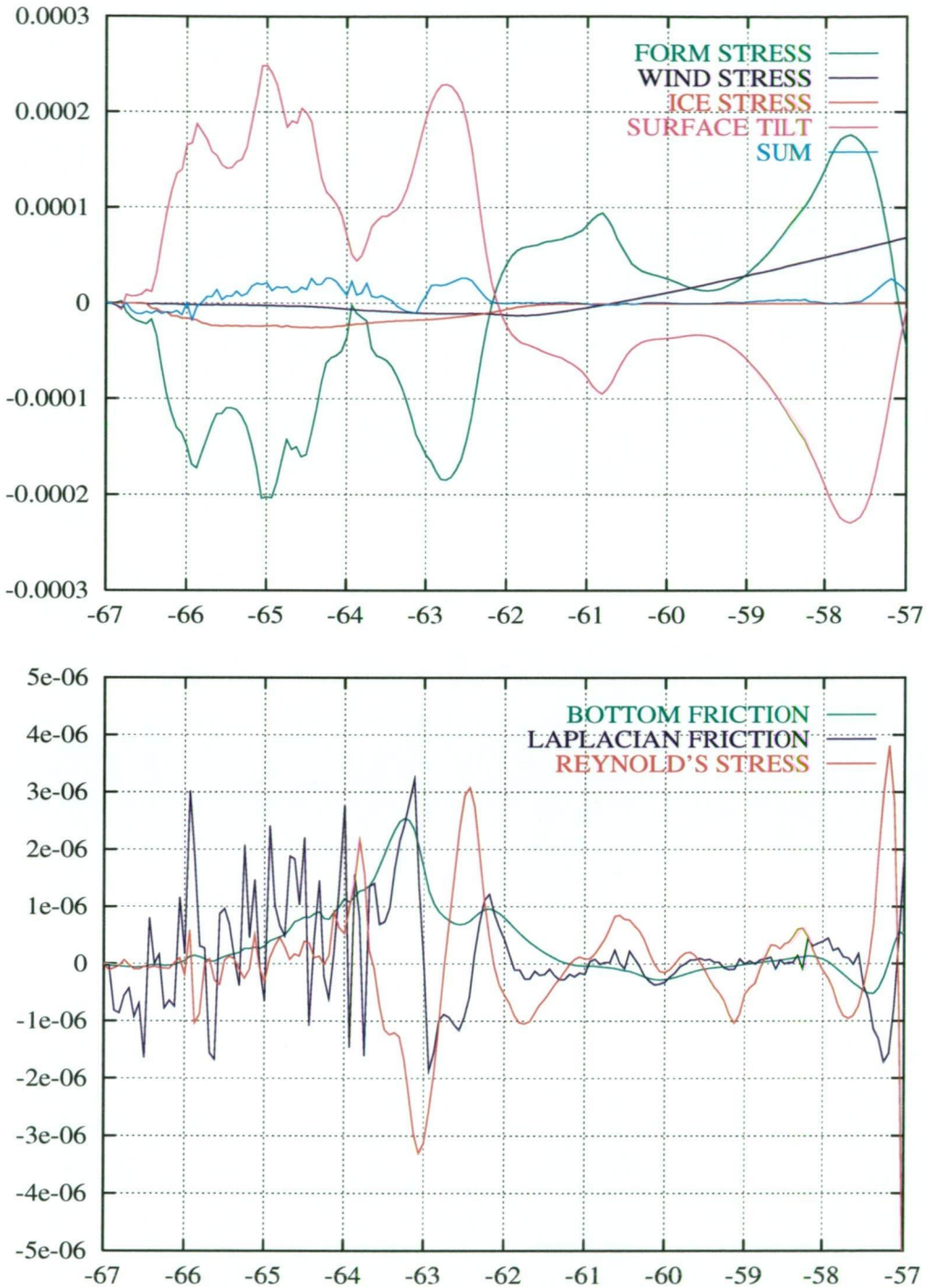

Fig. 4.3: Zonally integrated momentum balance ($m^2\ s^{-2}$) versus latitude, averaged over the last 10 years of the very high-resolution (VHR) simulation. The upper plot shows the dominant terms and the overall sum. The lower plot shows the small magnitude terms (note the change in scale).

model temperature from a simulation of the VHR model using biharmonic friction. The temperature distribution on the upper surface of the three dimensional picture shows a rich eddy structure, e. g. a mushroom vortex. Regions of higher temperature are sources for locally high oceanic heat flux. Unfortunately the above mentioned *chequer-boarding* is more severe when biharmonic friction is used, an effect currently not understood, but believed to be caused by failure of the numerical scheme to correctly model the momentum balance at the lateral boundaries in the presence of complex topography.

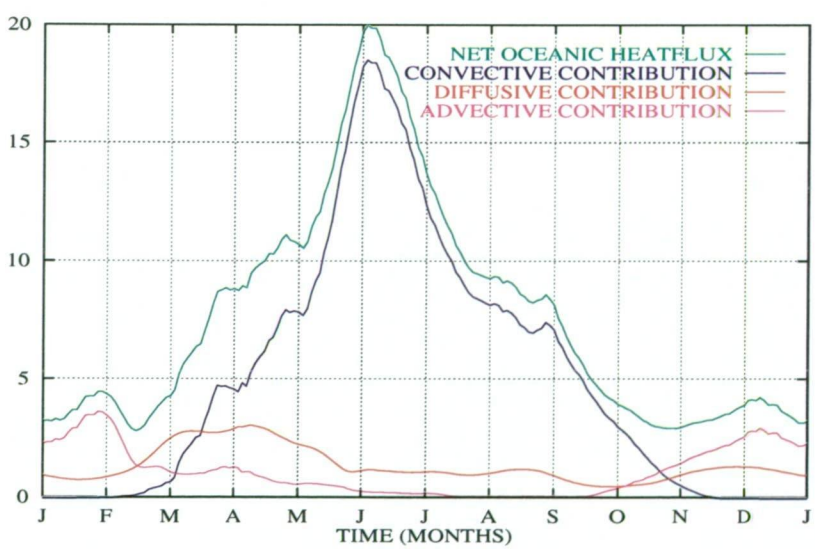

Fig. 4.4: Seasonal cycle of instantaneous areal-mean oceanic heat flux (W m^{-2}) averaged over the last 10 years of the 49 year VHR simulation.

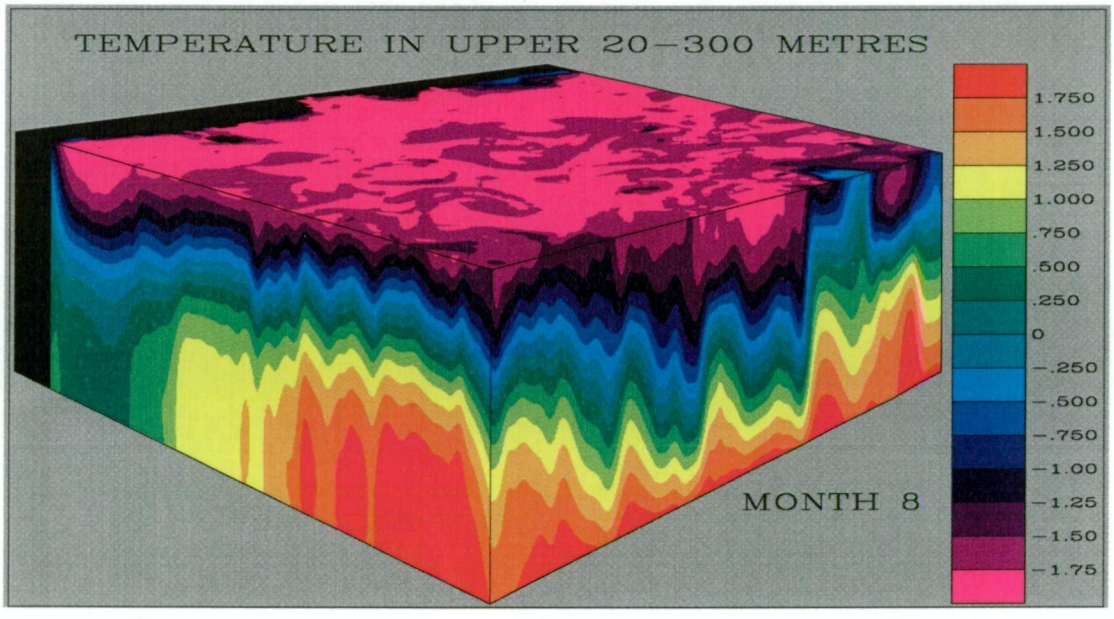

Fig. 4.5: Instantaneous picture of model potential temperature (°C) from a simulation using biharmonic viscosity.

4.2 Sensitivity to Sea-Ice Model Formulation

In this section a number of alternative formulations of the sea-ice model are considered. All of these sensitivity simulations are initialised with the ocean/sea-ice state at the end of Year 50 of the reference simulation (REF) discussed in Chapter 3 and are run for a further 10 years. Specifically, the following sensitivities are investigated: the exclusion of sea-ice dynamics (ND); the exclusion of the snow model (NS); removal of the snow-ice formation parameterisation (NS2I); and a series of simulations in which the constant salinity of sea-ice (S_{ice}) is incremented by 5 psu between simulations relative to the 5 psu used in the reference simulation (S10, S15, S20, S25, S30).

Figures 4.6 and 4.7 show the time evolution of sea-ice extent and volume respectively, for experiments REF, ND, NS, and NS2I. The largest changes are seen for the case excluding sea-ice dynamics (ND). In that simulation sea-ice thickness increases with time everywhere south of approximately 63°S (not shown), where the sea-ice cover also persists throughout the year. The maximum extent in ND is larger than all other cases, which indicates that sea-ice dynamic processes, rather than the *in situ* heat balance, are responsible for determining the location of the sea-ice edge. It is quite obvious that the ND scenario is unrealistic, the sea-ice becomes too thick and the seasonal minimum too great.

There is little difference in the maximum sea-ice extents between experiments REF, NS, and NS2I. However, the minimum sea-ice extent tends to increase in NS, and decrease in NS2I, which is also true for the sea-ice volume. The absence of the thermal insulation of a snow cover in NS brings about an increased sea-ice thickness relative to REF through additional freezing of sea water. This results in a 62% increase in the minimum sea-

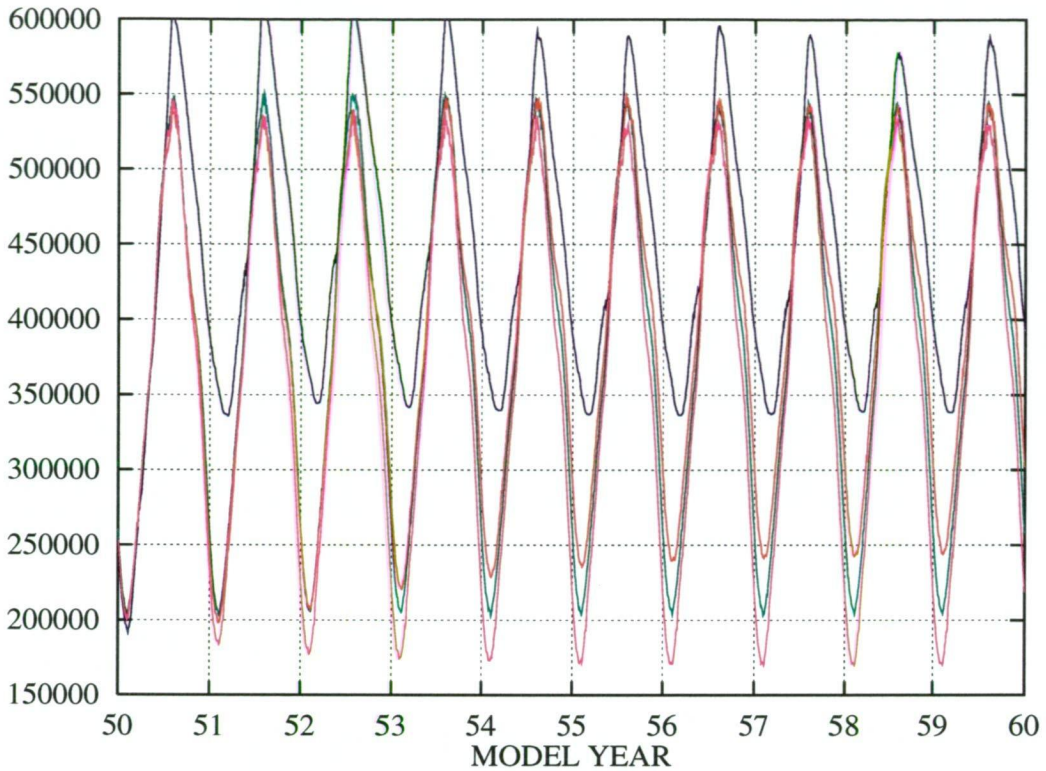

Fig. 4.6: Timeseries of sea-ice extent (km^2) for experiments REF, ND, NS, and NS2I. Color coding is as for Figure 4.7.

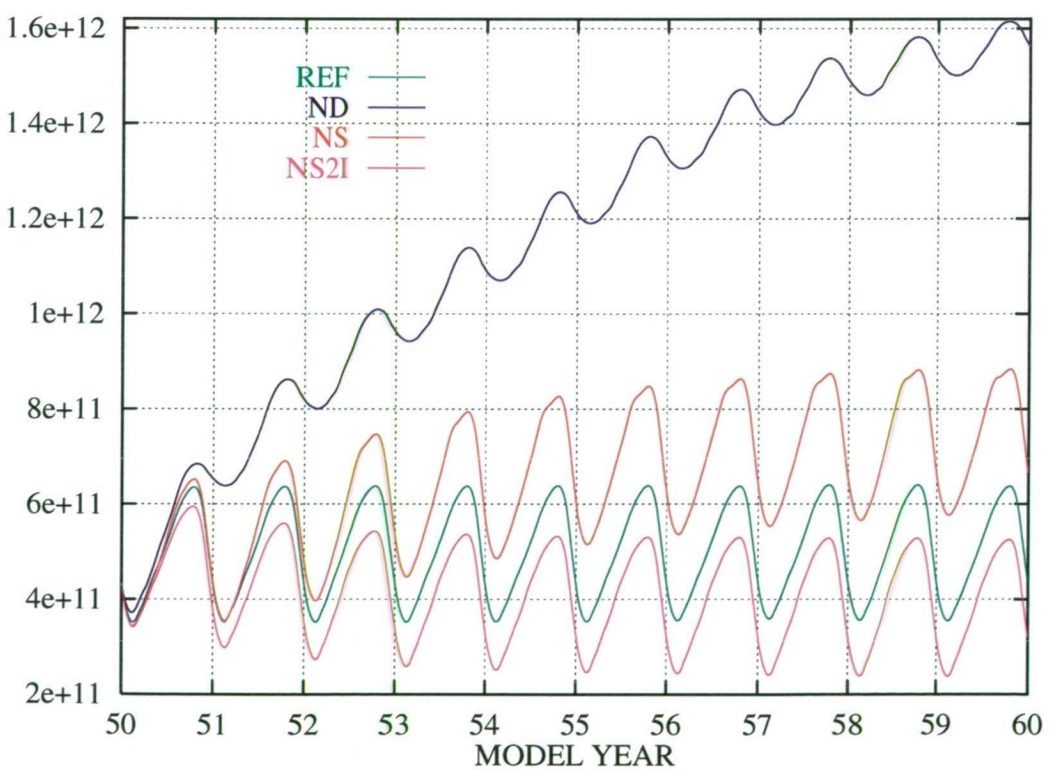

Fig. 4.7: Timeseries of sea-ice volume (m^3) for experiments REF, ND, NS, and NS2I.

ice volume and a 38% increase in the maximum sea-ice volume in the final year of NS relative to REF. Similarly there is a 19% increase in minimum extent and a 3% decrease in maximum extent. In NS2I it is the absence of snow-ice conversion that directly causes the decreased sea-ice thickness relative to REF. There is a 33% decrease in minimum sea-ice volume and an 18% decrease in maximum sea-ice volume in the final year of NS2I relative to REF. Likewise, there is a 17% decrease in minimum extent and a 3% decrease in maximum extent.

Figure 4.8 shows the seasonal cycle of oceanic heat flux for experiments REF, ND, NS and NS2I, along with a breakdown into convective, diffusive

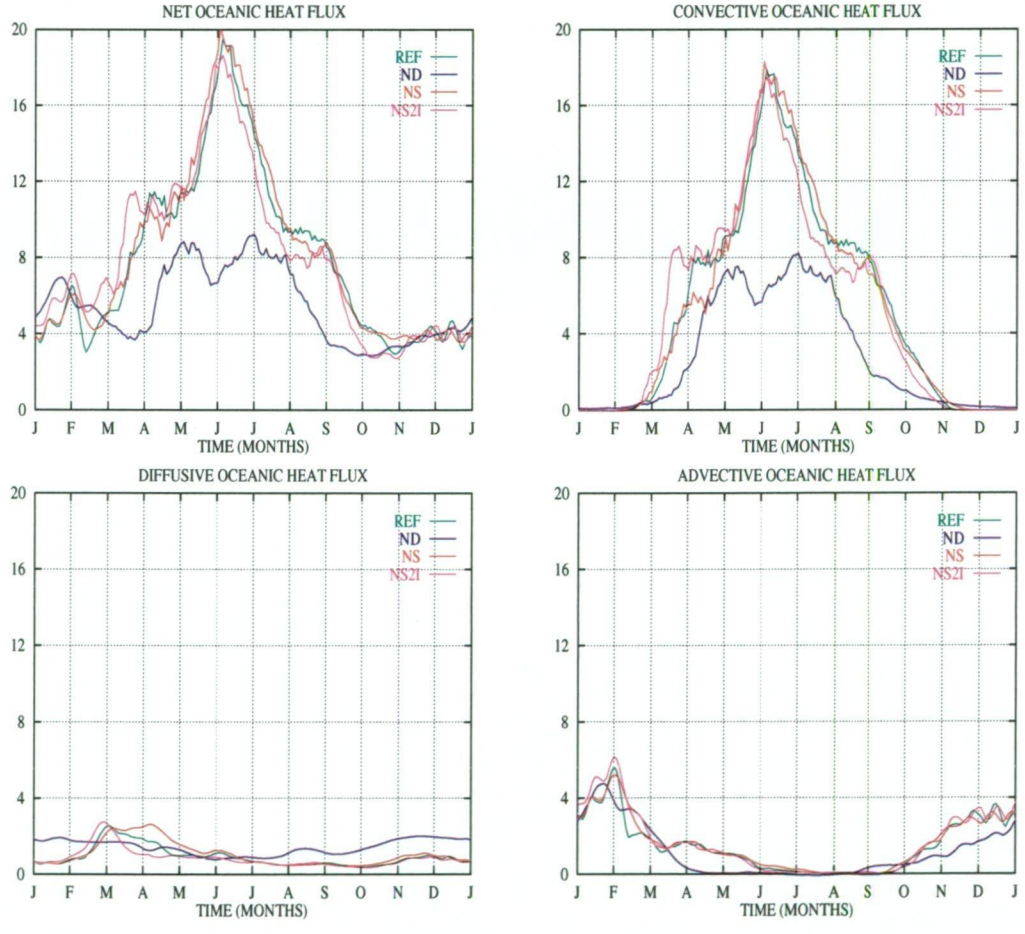

Fig. 4.8: Seasonal cycle of net, convective, diffusive and advective oceanic heat flux (W m^{-2}), averaged over years 50–60 of experiments REF, ND, NS, and NS2I.

and advective components. Once again the largest difference to REF is in ND. This is due to a large reduction in convection in that simulation, directly related to the reduction in sea-ice formation evident in Figure 4.7, although this is offset somewhat by an increase in diffusion. There is little difference in the magnitude or seasonality of the oceanic heat flux terms between experiments REF, NS, and NS2I.

Timeseries of sea-ice extent and volume for the final year of the sea-ice salinity sensitivity experiments (REF, S10, S15, S20, S25, S30) are shown in Figures 4.9 and 4.10 respectively. There is a clear trend relating increased sea-ice salinity to an increase in both the sea-ice extent and the sea-ice volume. The model gives this result because there is a direct relationship between the sea-ice salinity and the sea surface salinity, between the sea surface salinity and the rate of oceanic convection, between the rate of oceanic convection and the oceanic heat flux, and between the oceanic heat flux and the sea-ice bulk properties (extent and volume). As S_{ice} is increased the impact of brine rejection on the sea-surface salinity is decreased. Figure 4.11 shows the salinity of the model ocean's upper layer over the last year of the simulations. Increasing S_{ice} from 5 psu to 30 psu decreases the intra-annual variability in areal mean surface salinity from 0.26 psu to 0.10 psu for the year shown.

The net oceanic heat flux for the sea-ice sensitivity experiments, along with the contributing terms, is shown in Figure 4.12. The convective contribution decreases with respect to increasing S_{ice}, and the diffusive contribution increases with respect to increasing S_{ice}. There is little difference between simulations in the advective contribution. The time means of the area averaged oceanic heat flux components for the decade under consideration are given in Table 4.1. Comparing experiment REF (5 psu) with experiment S30 (30 psu), there is a 19% decrease in the net oceanic heat flux, brought about by a 64% decrease in the convective heat flux, the effect of which is offset by a 195% increase in the diffusive heat flux and a much

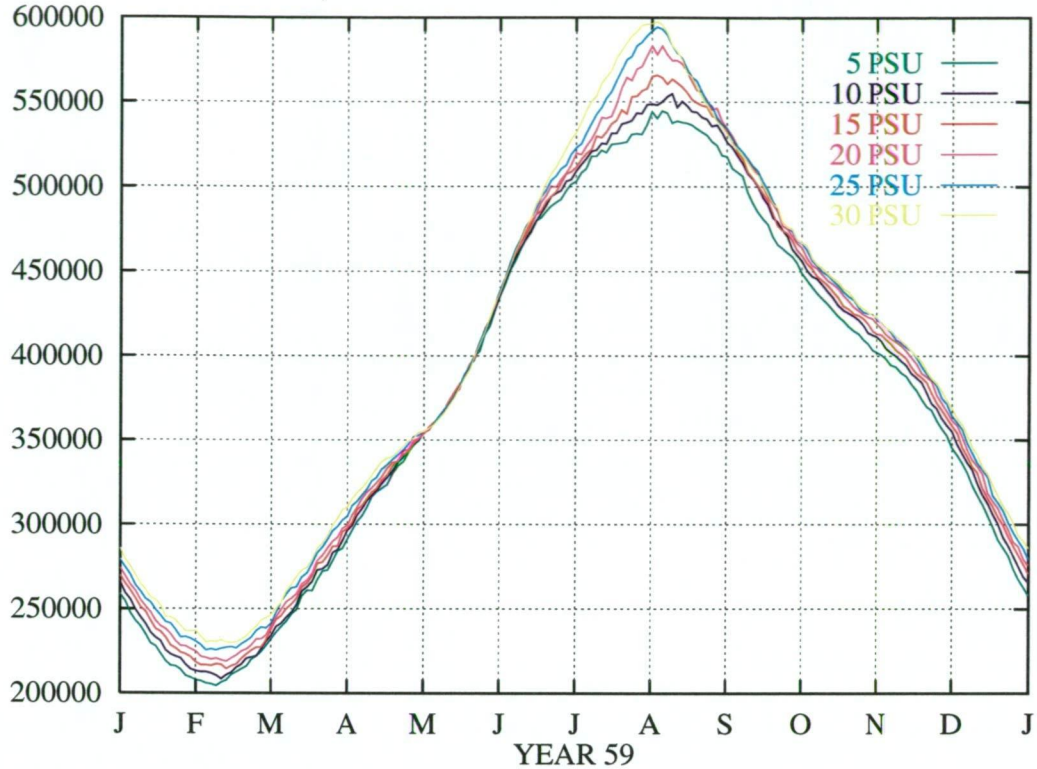

Fig. 4.9: Timeseries of sea-ice extent (km^2) for experiments REF (5 psu), S10, S15, S20, S25, and S30.

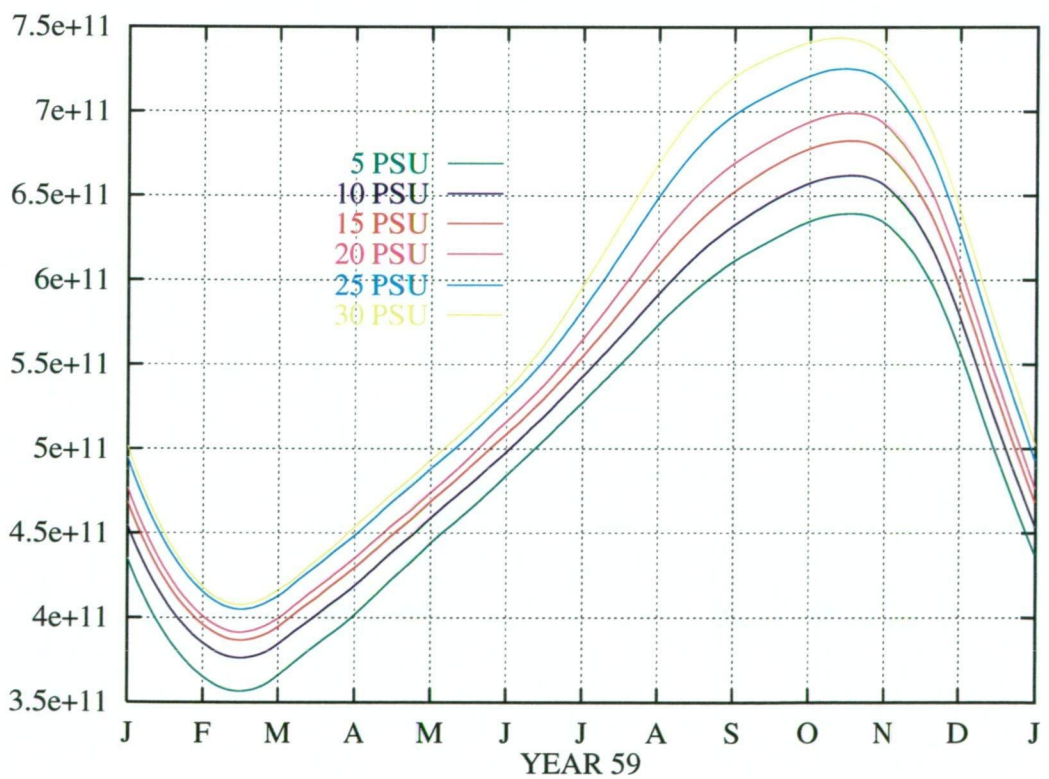

Fig. 4.10: Timeseries of sea-ice volume (m^3) for experiments REF (5 psu), S10, S15, S20, S25, and S30.

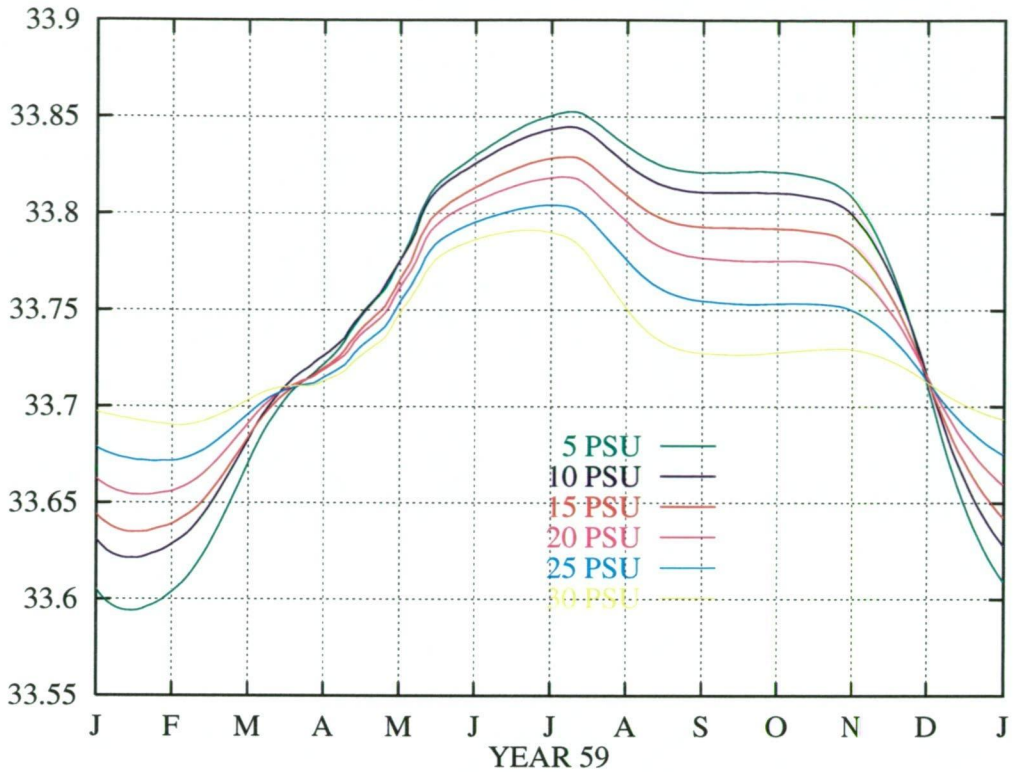

Fig. 4.11: Timeseries of model ocean upper layer mean salinity (psu) for the reference simulation ($S_{ice} = 5$ psu), and for the sea-ice salinity sensitivity simulations.

smaller (5%) increase in the advective heat flux. The inverse relationship between the convective and diffusive fluxes is explained as follows. Convection erodes the oceanic vertical stability and tends to produce vertical homogeneity of the ocean's thermohaline fields where it is active. This reduces the magnitude of the vertical gradients of temperature and salinity and hence the diffusion, due to the constant coefficient parameterisation used (see Equations 2.8 and 2.9). On the other hand as convective activity is reduced, the gradients of temperature and salinity become stronger, and the diffusion parameterisation provides more heat to the surface. It is indicative of the importance of the sea-ice salinity in controlling the sea surface salinity via brine rejection, that in REF convection provides 69% of the net oceanic heat flux and diffusion 13%, while in S30 convection provides

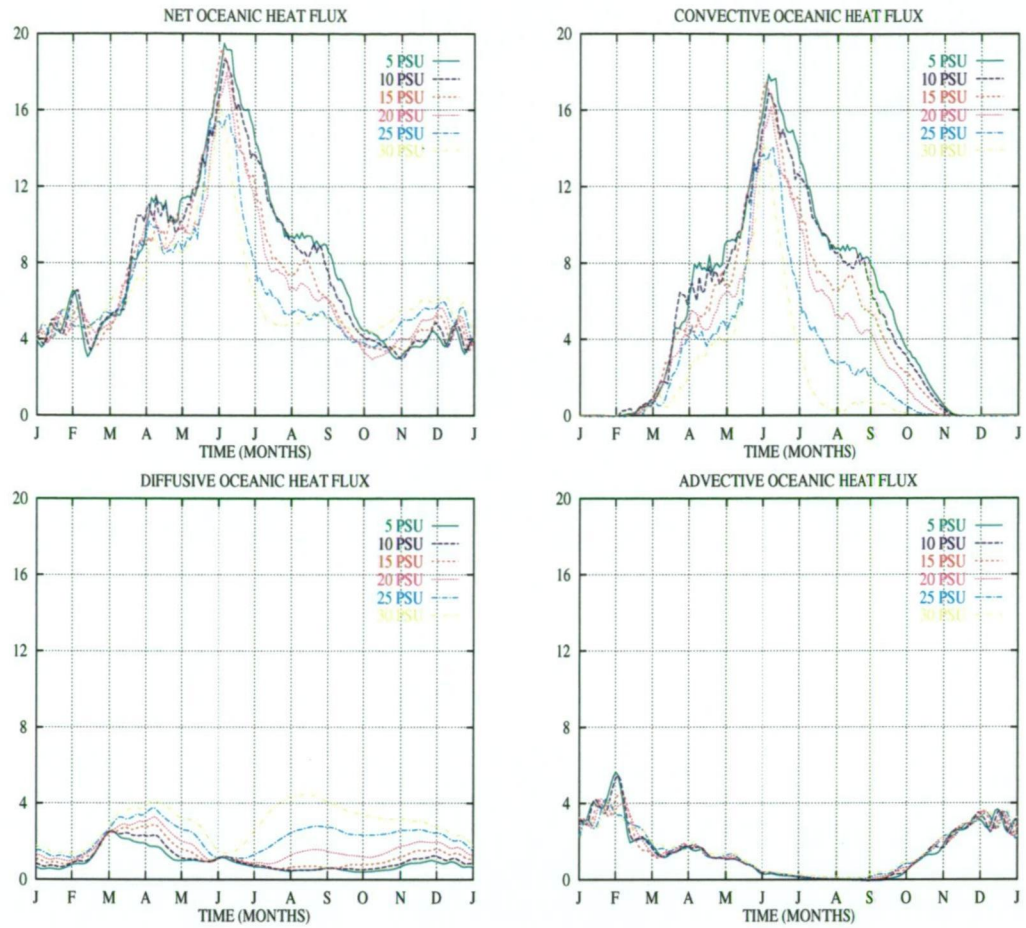

Fig. 4.12: Seasonal cycle of net, convective, diffusive and advective oceanic heat flux (W m^{-2}), averaged over years 50–60 of experiments REF, S10, S15, S20, S25, and S30.

only 30% of the net and the diffusive contibution increases to 45%.

S_{ice}	$\bar{Q}_{net}$	$\bar{Q}_{con}$	$\bar{Q}_{dif}$	$\bar{Q}_{adv}$
5	8.06	5.51	1.01	1.54
10	7.86	5.16	1.14	1.56
15	7.39	4.52	1.34	1.54
20	7.08	3.82	1.69	1.56
25	6.78	2.88	2.31	1.59
30	6.56	1.97	2.98	1.61

Tab. 4.1: Time averaged components of oceanic heat flux (W m^{-2}) for the constant sea-ice salinity (S_{ice}) sensitivity simulations. $\bar{Q}_{net}$, $\bar{Q}_{con}$, $\bar{Q}_{dif}$, and $\bar{Q}_{adv}$ denote the time mean net, convective, diffusive and advective fluxes respectively, averaged over the 10 years of each simulation.

4.3 Sensitivity to Variations in Constant Surface Fresh Water Flux

There is a great deal of seasonal variability in both the extent and areal concentration of the sea-ice cover in the Southern Hemisphere. The sea-ice maximum is around 19 $\times$ 10^6 km^2 in September–October, with a minimum of 4 $\times$ 10^6 km^2 in February (Zwally *et al.*, 1983; Gloerson *et al.*, 1992). Gordon (1981), using a mean monthly surface climatology to determine if air/sea heat exchange alone was able to explain the rapid spring melt of Antarctic sea-ice, was the first to suggest that the magnitude of surface fresh water flux may be a major factor in determining this seasonality. He points out that in contrast to the Arctic Ocean, where a high surface fresh water flux induces a fresher surface layer and a stronger pycnocline that inhibits vertical heat exchange between the warmer deep water and the cooler surface, the relatively low fresh water flux in the Southern Ocean leads to a much weaker pycnocline with significantly less resistance to the upward transport of oceanic heat through mixing and dynamical processes. The work of Fichefet and Morales Maqueda (1997a) suggests the sensitivity of a sea-ice model to the inclusion of snow, and to snow-ice conversion is much greater in the Antarctic than in the Arctic. Weatherly and Walsh (1996) show that Arctic sea-ice is particularly sensitive to changes in precipitation, using a regional version of the Modular Ocean Model with dynamic/thermodynamic sea-ice. In their zero precipitation experiment sea-ice thickness reduced rapidly due to the much higher oceanic heat flux, while in a double precipitation experiment sea-ice thickness increased to a lesser extent. Until now, the sensitivity of the upper-ocean/sea-ice interaction to variations in the surface fresh water flux has not been directly investigated for the Southern Ocean.

Five simulations of the East Antarctic high-resolution coupled ocean/sea-

ice model, each starting from the end of Year 50 of the reference simulation discussed in Chapter 3, have been run with constant precipitation minus evaporation (P–E) rates of 0, 25, 50, 75 and 100 cm a^{-1}. Figure 4.13 compares time evolution of total sea-ice extent (i. e. the sum of the areas of grid cells containing sea-ice) for these space and time constant surface fresh water flux simulations. In general both the sea-ice maximum and minimum extents increase with increasing P–E rate, as does the seasonal variability of extent and the time mean extent. The time mean sea-ice extents for the decade shown were 333000, 348000, 377000, 393000, and 410000 km^2 for the 0, 25, 50, 75 and 100 cm a^{-1} P–E rates respectively. Fitting this to a simple linear regression model yields a coefficient of determination of 0.99, indicating that 99% of the sum of squares of the deviations of mean extent within each simulation, with respect to mean extent across all five simulations, can be explained by the variation in P–E rate. Hence there is a strong linear relationship between the time mean sea-ice extent and the constant P–E rate for the decade under consideration.

Figure 4.14 shows the evolution of upper ocean layer salinity for the five model runs, and for comparison the sea surface salinity (SSS) for the corresponding period in the reference simulation. The response of SSS to variation in constant fresh water flux is to be expected, with a lower P–E rate leading to a higher SSS and vice versa. It can also be seen that the magnitude of intra-annual variation in SSS decreases with decreasing P–E rate. This is a result of the reduced intra-annual variation in sea-ice extent (and volume), and the associated reduction in salt exchanges between the ocean and sea-ice models. The mean monthly P–E rates for the reference simulation vary in space and time (see Figure A.3 in the appendices), but have an annual mean of 46.2 cm a^{-1} over the modelled region. Therefore it is not surprising that the SSS response of the reference simulation is very similar to that of the 50 cm a^{-1} constant P–E simulation. Also this allows some confidence that the use of a constant P–E rate is not a bad

approximation over the model region.

The seasonal cycle of net oceanic heat flux, along with it's breakdown into convective, advective and diffusive terms, is shown in Figure 4.15. The time averaged values for the 5 years from Year 55 to Year 59 inclusive are summarised in Table 4.2. Considering the 25, 50, 75 and 100 cm a^{-1} P–E runs it is found that the convective contribution ($\bar{Q}_{con}$) is monotonically decreasing with respect to increasing P–E, and that the diffusive contribution ($\bar{Q}_{dif}$) is monotonically increasing with respect to increasing P–E. These two effects tend to balance each other, and as there is little change in the advective contribution ($\bar{Q}_{adv}$) the result is that there is little difference in the time averaged net oceanic heat flux ($\bar{Q}_{net}$) between the 25, 50, 75 and 100 cm a^{-1} P–E runs. However, the 0 cm a^{-1} P–E simulation has a time mean oceanic heat flux of 15.4 W m^{-2}, nearly double that of the other runs. This relatively high value is maintained by oceanic convection, which is around 30 W m^{-2} for the months June to August, and exceeds the convective heat flux of the other simulations throughout the year (excepting December–January when convection is not present in any of the runs).

It turns out that an annual cycle of sea-ice advance and retreat similar

P–E	$\bar{Q}_{net}$	$\bar{Q}_{con}$	$\bar{Q}_{dif}$	$\bar{Q}_{adv}$
0	15.36	11.85	1.11	2.40
25	8.75	6.24	0.73	1.79
50	7.71	5.04	1.09	1.58
75	7.91	4.36	1.97	1.58
100	8.67	2.69	4.29	1.69

Tab. 4.2: Time averaged components of oceanic heat flux (W m^{-2}) for the constant P–E sensitivity simulations (cm a^{-1}). $\bar{Q}_{net}$, $\bar{Q}_{con}$, $\bar{Q}_{dif}$, and $\bar{Q}_{adv}$ denote the time mean net, convective, diffusive and advective fluxes respectively.

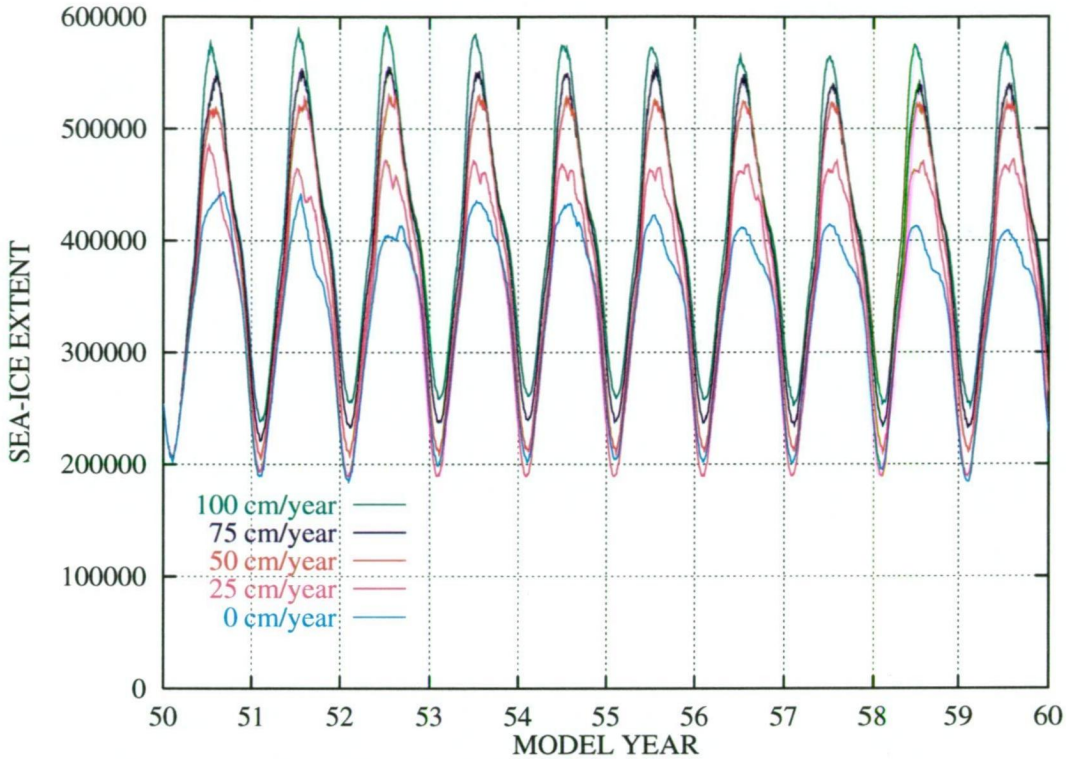

Fig. 4.13: Timeseries of sea-ice extent (km^2) for the constant P–E sensitivity simulations.

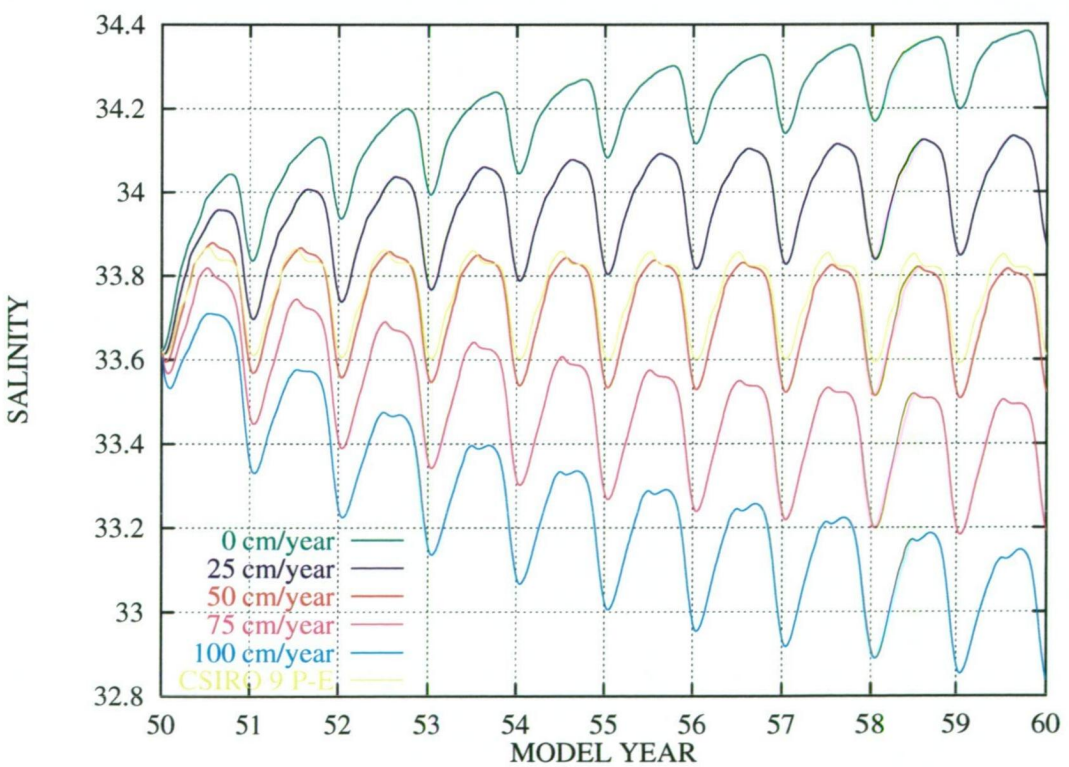

Fig. 4.14: Timeseries of model ocean upper layer mean salinity (psu) for the constant P–E sensitivity simulations, and for the reference simulation using CSIRO 9 P–E.

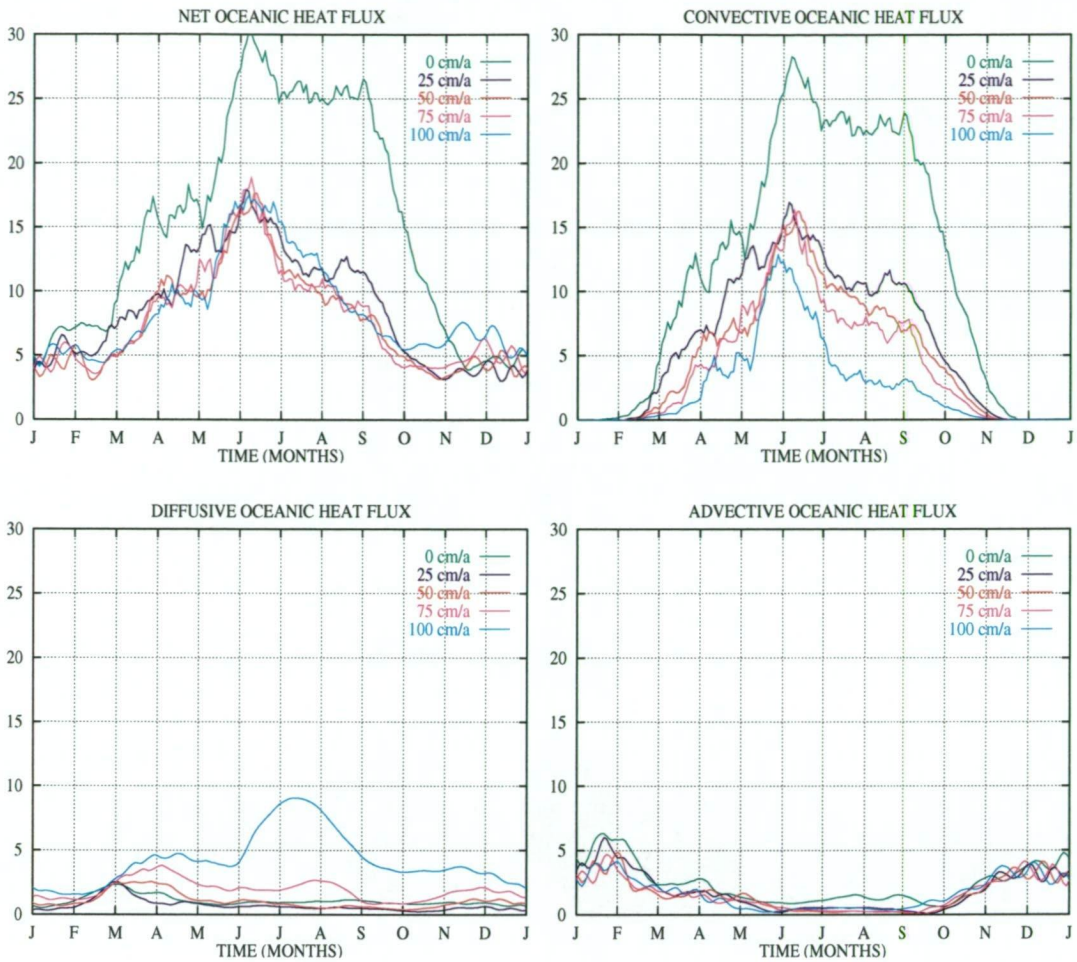

Fig. 4.15: Seasonal cycle of net, convective, diffusive and advective oceanic heat flux (W m^{-2}), averaged over the second 5 years of the 10 year run (i. e. Year 55–59) of each of the five constant surface fresh water flux simulations.

to that seen in the reference simulation of Chapter 3 cannot be maintained for the case of 0 cm a^{-1} P–E forcing. The increasing SSS (Figure 4.14) and strong oceanic convection (Figure 4.15) eventually leads to a transition in the ocean's thermohaline state which brings about an increase in SST and a large reduction in sea-ice extent. Figures 4.16 and 4.17 compare the time evolution of sea-ice extent and SSS in the 0 and 25 cm a^{-1} constant P–E simulations for extended runs of 40 years. In the period Year 60–65 of the 0 cm a^{-1} P–E simulation, the magnitude of the seasonal cycle of sea-ice

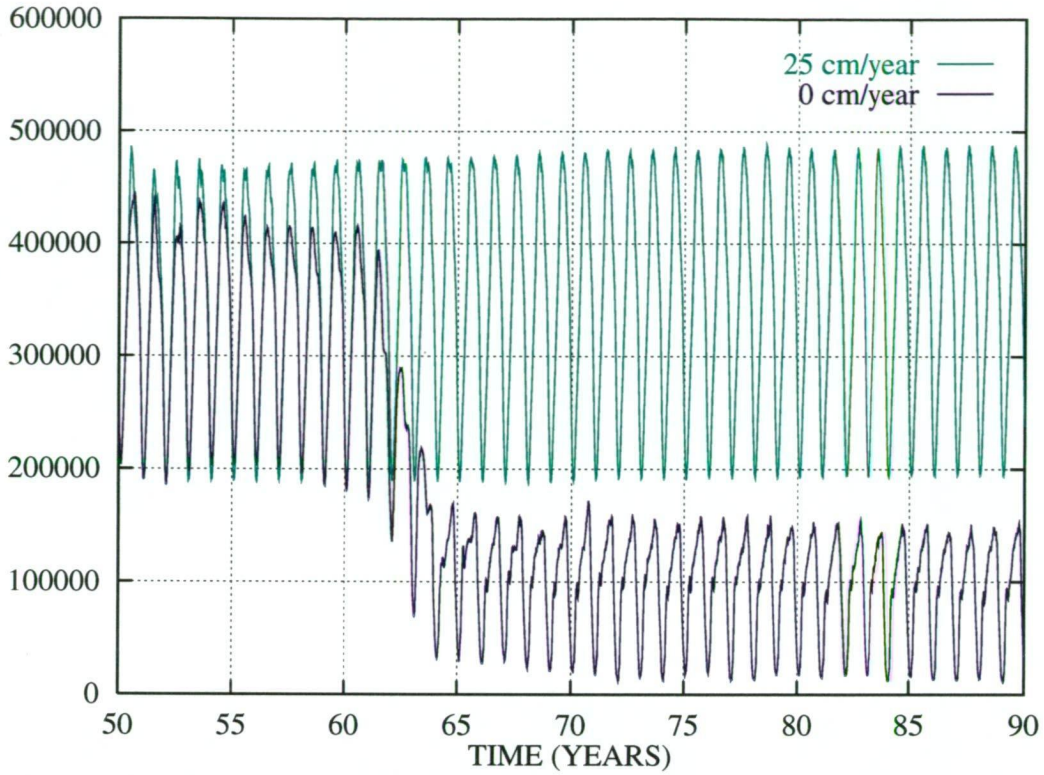

Fig. 4.16: Seasonal cycle of sea-ice extent (km^2) for the 0 and 25 cm a^{-1} constant P–E simulations over a 40 year period.

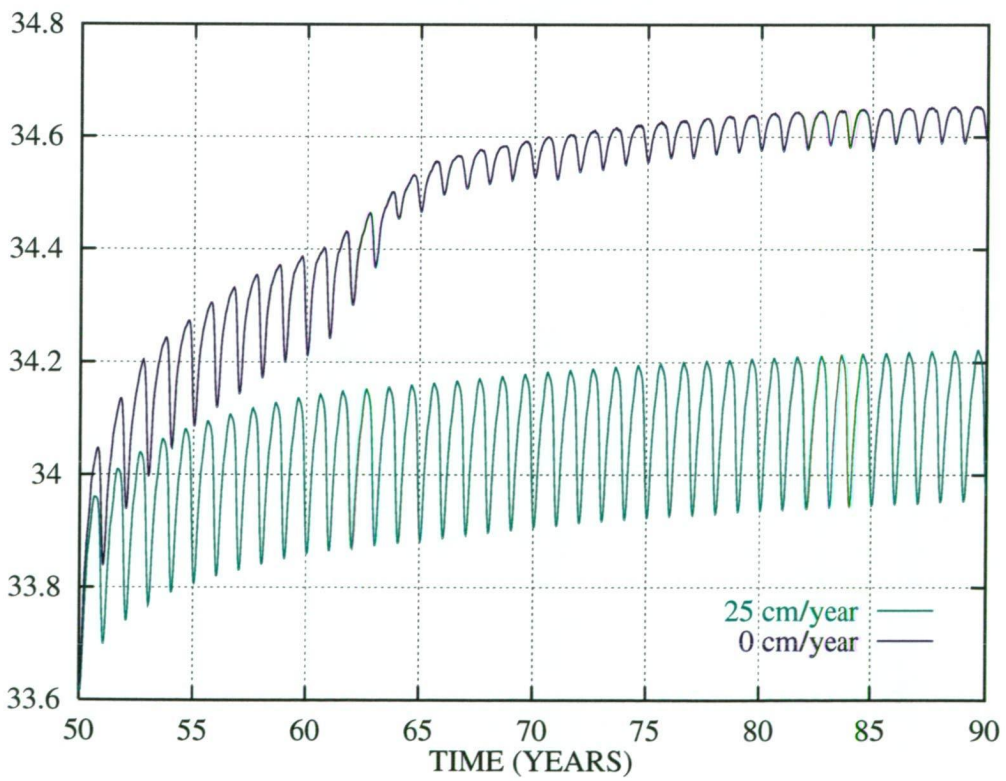

Fig. 4.17: Same as Figure 4.16 but for SSS (psu).

extent rapidly decreases. After Year 65 the cycle of sea-ice extent becomes stable, but with a maximum extent that is less than the minimum extent prior to Year 60, and with almost zero sea-ice cover at minimum extent. In contrast, there is very little variability in the seasonality of sea-ice extent in the 25 cm a^{-1} constant P–E simulation. The SSS timeseries for these two model runs are shown in Figure 4.17. Although the spatially averaged SSS increases in magnitude throughout both the simulations, the trend is far more pronounced in the 0 cm a^{-1} model, especially before Year 70. After Year 70 the ocean/sea-ice coupling in this scenario has entered a new state, characterised by high SSS ($\sim$34.6 psu relative to a deep water salinity of $\sim$34.7 psu) and diminutive sea-ice extent.

Figures 4.18 and 4.19 compare meridional sections of mean annual salinity and temperature respectively, between Year 50 of the reference simulation and Year 90 of the 0 cm a^{-1} P–E simulation. The effect of a prolonged period of 'thermal mode' activity (large-scale temperature-driven convection) in the 0 cm a^{-1} run is to mix the ocean's haline distribution throughout the water column. Also, a large portion of the model's deep water has been considerably cooled by this process. Interest in the physics of the 'thermal mode' ocean at high latitudes was sparked by the appearance of the Weddell Polynya in the 1970's, a subject discussed in more detail in Chapter 5.

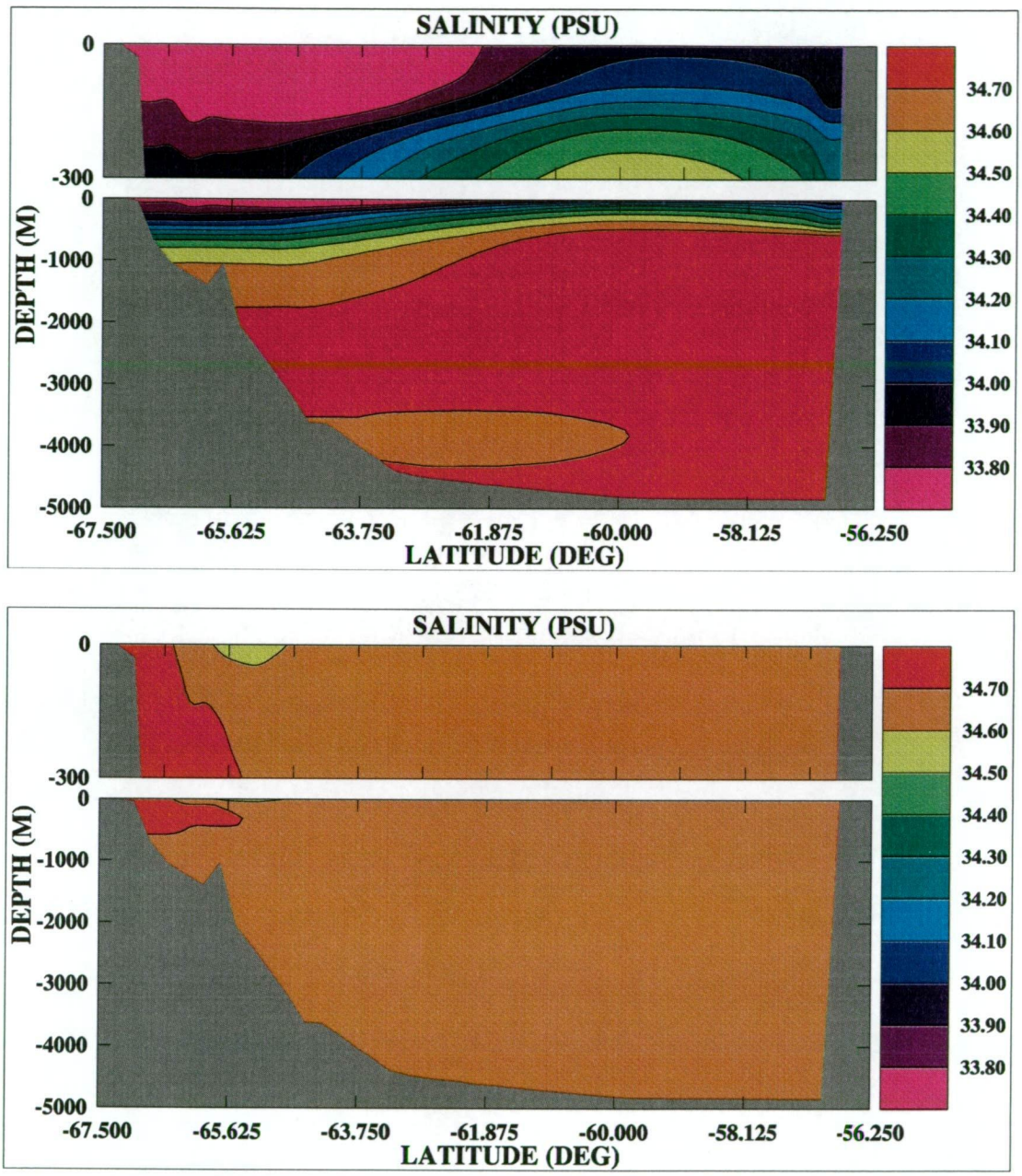

Fig. 4.18: Meridional section of mean annual zonally integrated salinity (psu) from Year 50 of the reference simulation (top), and Year 90 of the 0 cm a^{-1} P–E simulation (bottom). The upper panel in each plot shows a magnified view of the upper 300 m of the ocean's salinity field.

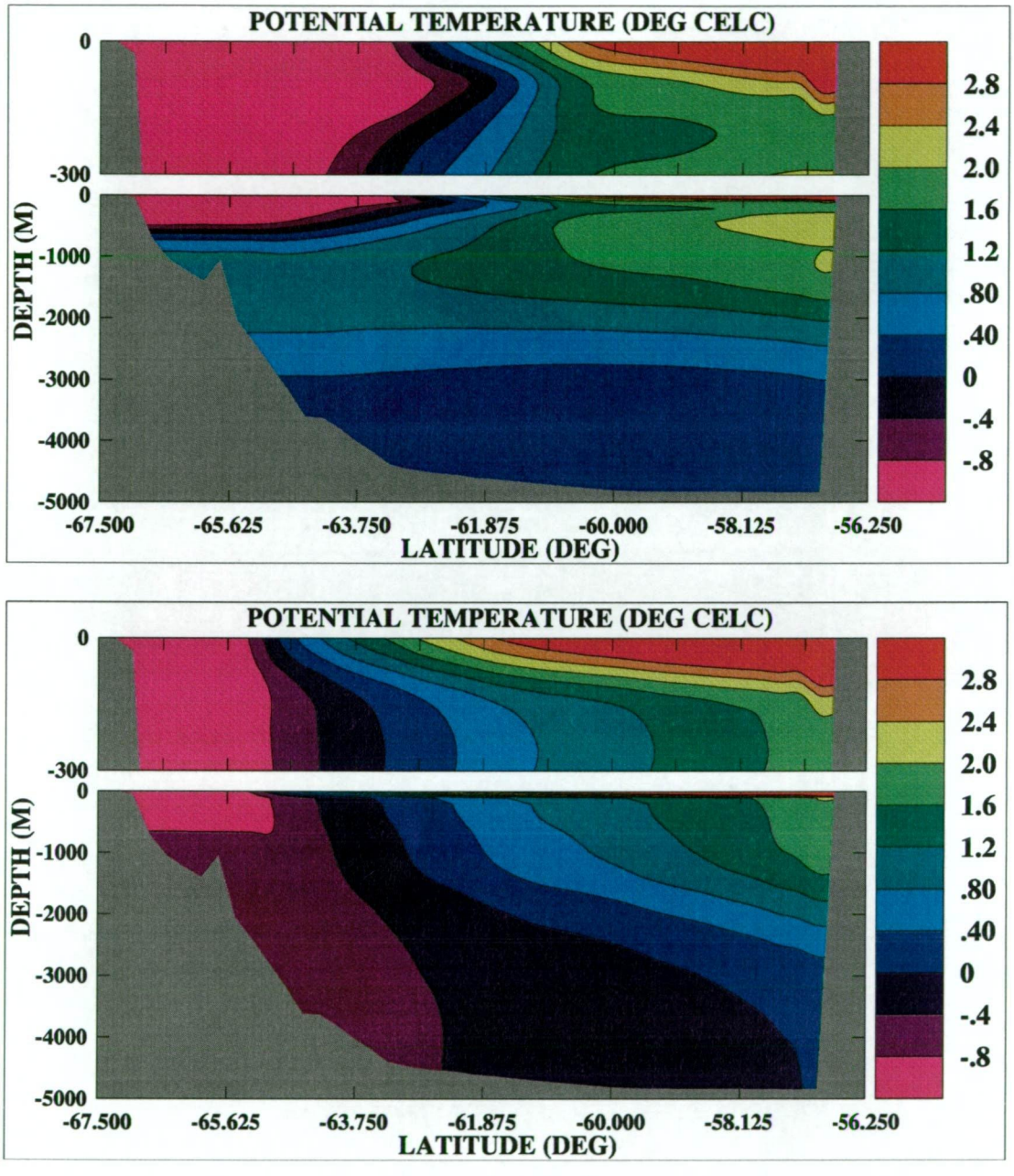

Fig. 4.19: As in Figure 4.18 but for potential temperature (°C).

5. THE SOUTHERN OCEAN SECTOR MODEL

5.1 Model Description

To investigate the behaviour of the full Southern Ocean coupled ocean/sea-ice system the model has been formulated in a full Southern Hemisphere version known as the Southern Ocean Sector Model, employing the telescoped grid of Wolff (1994; 1999). The horizontal grid of the Southern Ocean Sector Model is shown in Figure 5.1. Within each of the subgrids (odd/even) of the Arakawa E-grid the model is coarse-resolution (2.5° in longitude) from 120°W to 60°E, fine-resolution (0.5° in longitude) between 120-180°E, of smoothly decreasing longitudinal resolution between 60-120°E, and of smoothly increasing longitudinal resolution between 180-240°E. A resolution of 1° in latitude is used in each subgrid throughout the model domain. The vertical grid has 15 layers with thicknesses of 10, 10, 20, 20 ,80, 120, 280, 320, 280, 720, 780, 720, 780, 720, and 1280 meters from surface to bottom respectively. The model topography is shown in Figure 5.2. A solid wall with no-slip boundary condition is used to close the model near the equator. The model time step is 1 hour. Model constants and parameters are the same as for the high-resolution model (see Tables 3.1 and 3.2) except for the following horizontal viscosity and diffusivity parameters: the harmonic horizontal viscosity coefficient is 5000 m^2 s^{-2}; the biharmonic horizontal viscosity coefficient is 1×10^{-3} m^4 s^{-2}; and the coefficient of hor-

izontal diffusivity is 1000 m^2 s^{-2}. Temperature and salinity initialisation fields were obtained from the data set of J. Reid for the period from the early 1900's to 1985 (N. Bindoff, pers. comm.). The thermohaline data was mapped onto model levels using vertical EOF's (Bindoff and Wunsch, 1992) and then onto the model grid using objective mapping.

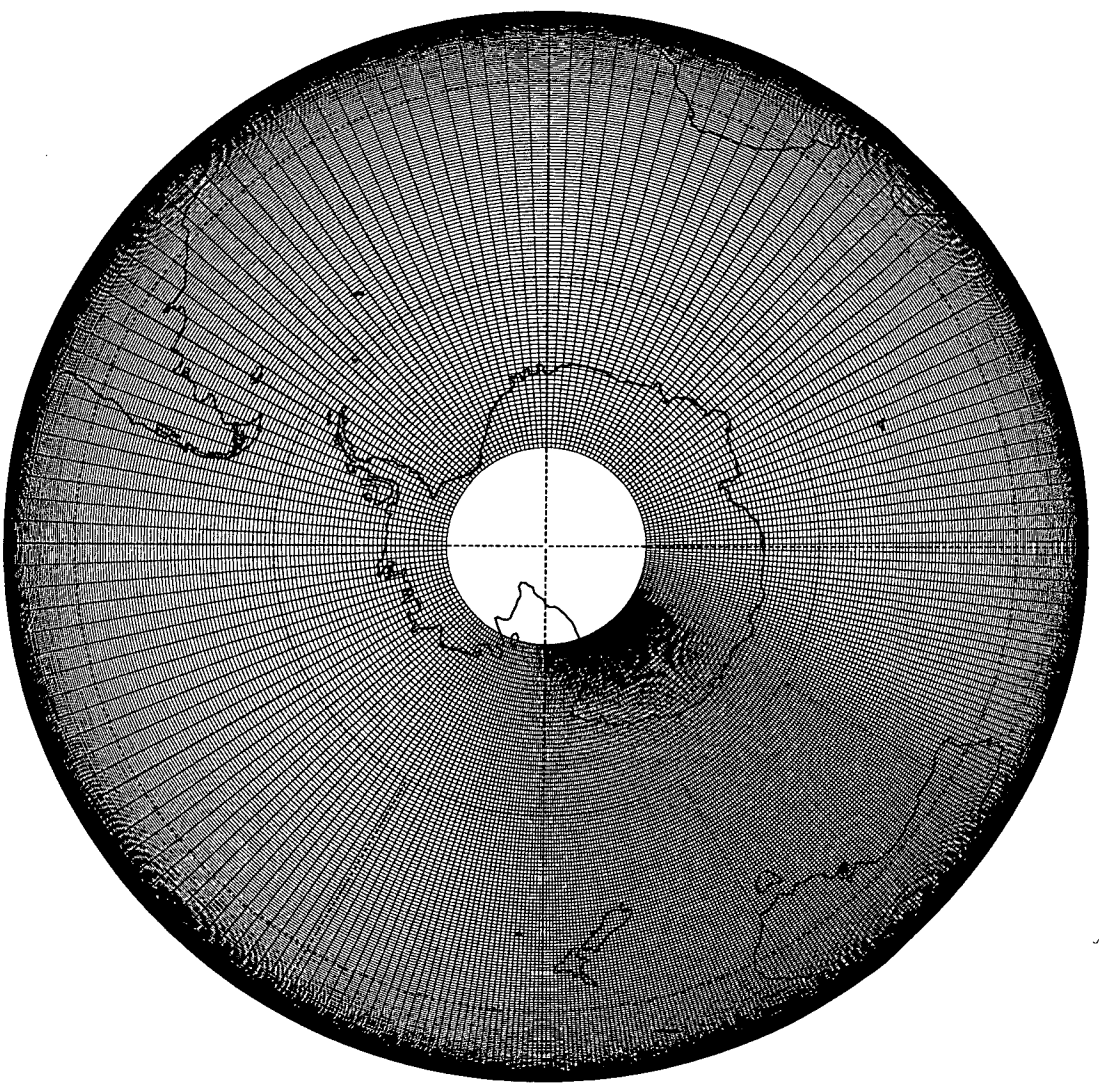

Fig. 5.1: Solid lines show the horizontal grid of the Southern Ocean Sector Model. The grid is separated into a coarse-resolution and a fine-resolution sector, with variable resolution in the remainder as discussed in the text.

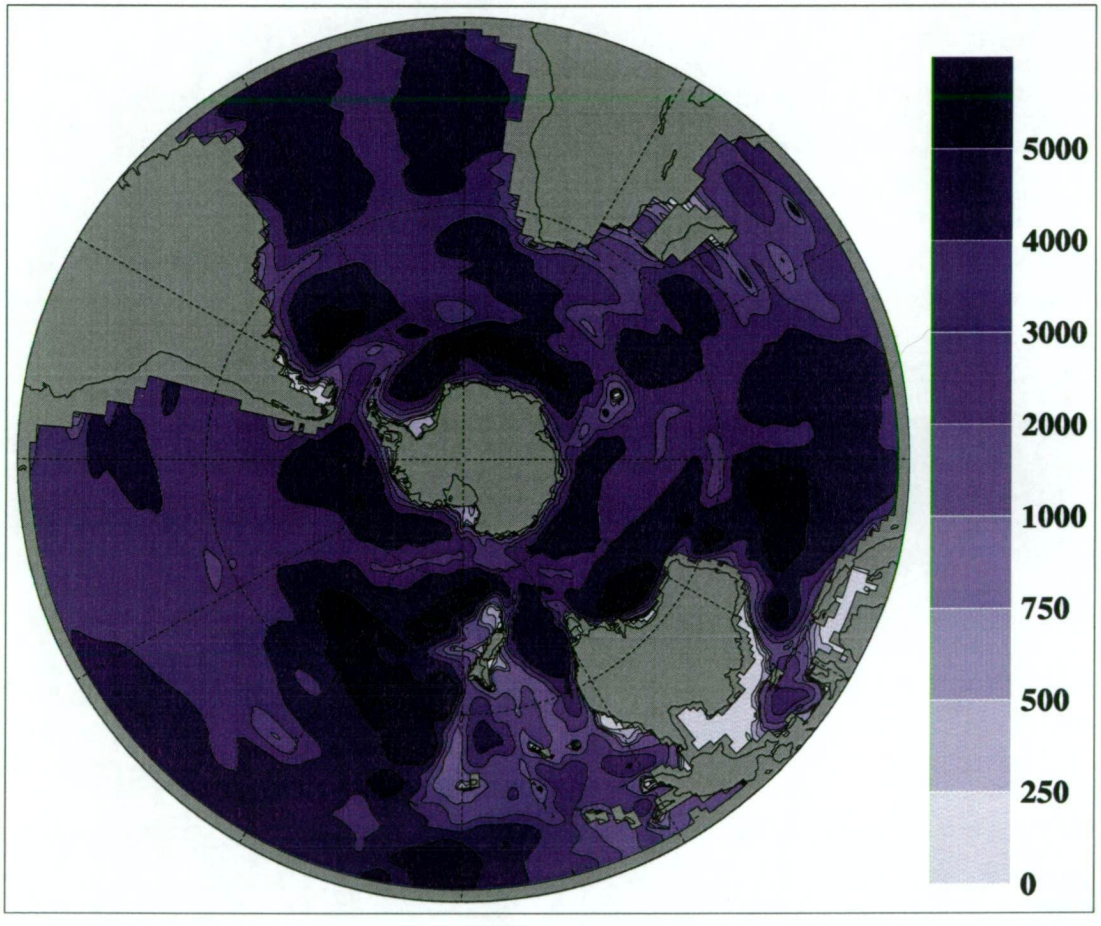

Fig. 5.2: Bathymetry (m) of the Southern Ocean Sector Model.

5.2 Reference Simulation

In this section a 5 year reference simulation of the Southern Ocean Sector Model is briefly discussed. Mean monthly surface forcing is derived from the same source as the high-resolution model of Chapter 3 (i. e. from output of the CSIRO 9 model for the decade 1981–1990), and is shown in Appendix B. The sea-ice compactness distribution for the final year of the integration is shown in Figure 5.3. The annual cycle compares reasonably well with satellite observations (Gloerson *et al.*, 1992), although the spring melt is too extreme which results in too little sea-ice in the months December–March. An interesting feature is the occurrence of a springtime (November) polynya in the Ross Sea which also appears in the satellite observations. The wintertime compactness is quite high ($> 90\%$) in most regions.

The seasonal cycle of the oceanic heat flux terms is shown in Figure 5.4. The pattern is quite similar to that found in the high-resolution model, with convection dominating in the winter months, advection dominating in December–January, and the diffusion being relatively constant throughout the year. In the rapid growth phase (March–May) the areal-average convective heat flux exceeds 50 W m^{-2}, and is around 35 W m^{-2} for the remainder of the winter (June–August). This is in reasonable agreement with an estimate of 41 W m^{-2} for the active winter entrainment period obtained using hydrographic data (Gordon and Huber, 1990). The mean net oceanic heat flux over the last 3 years of the simulation is 25.1 W m^{-2}. The means for the convective, diffusive and advective contributions are 20.6, 2.1, and 2.4 W m^{-2} respectively.

Figure 5.5 shows the spatial distribution of mean monthly net oceanic heat flux. During the winter months the oceanic heat flux is very high in most places, excepting in the Western Weddell Sea where a pronounced tongue of lower oceanic heat flux forms, and in the Bellingshausen Sea. These regions of lower oceanic heat flux expand in September to cover over

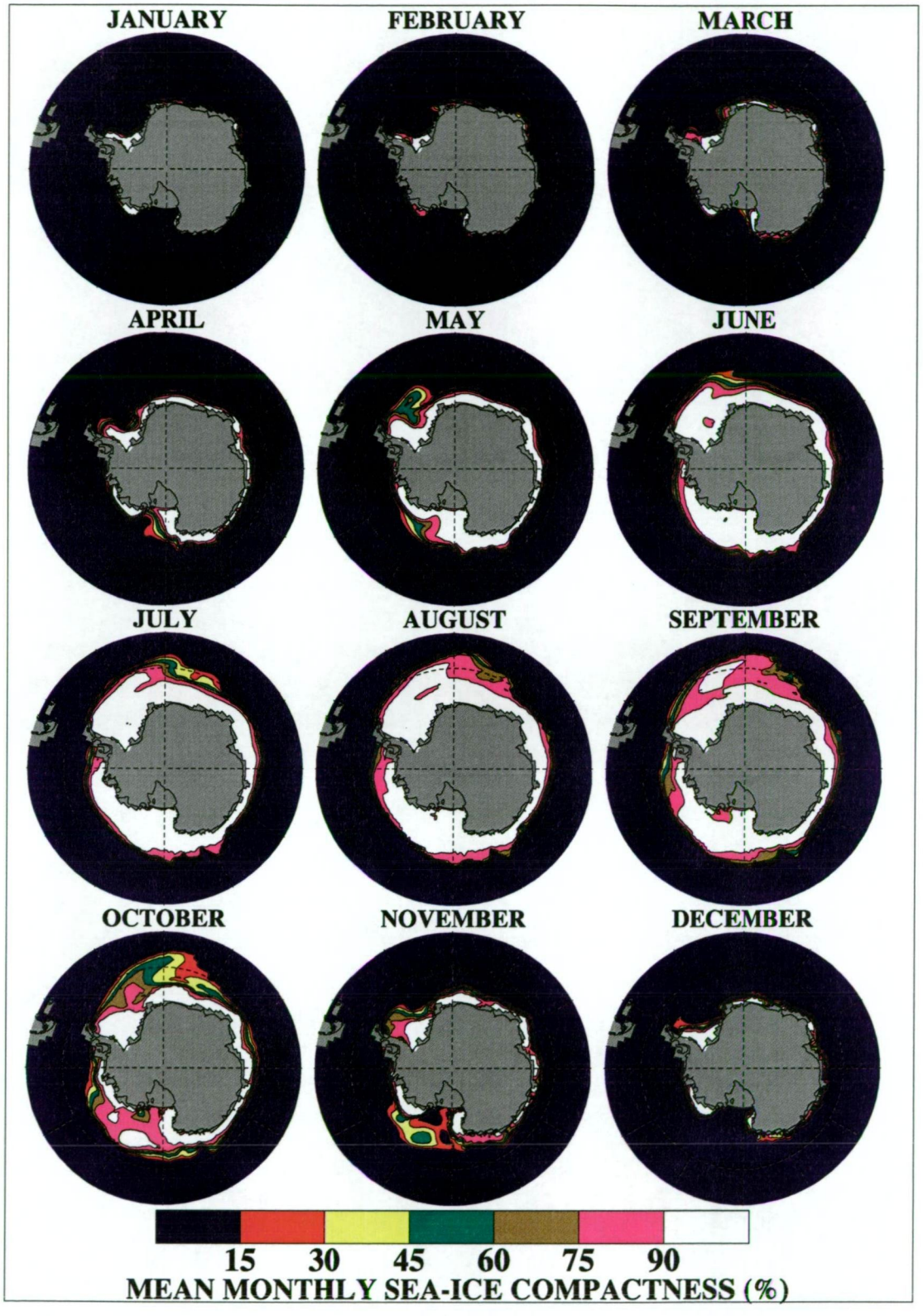

Fig. 5.3: Mean monthly sea-ice compactness (%) in the 5^{th} year of the reference simulation of the Southern Ocean Sector Model.

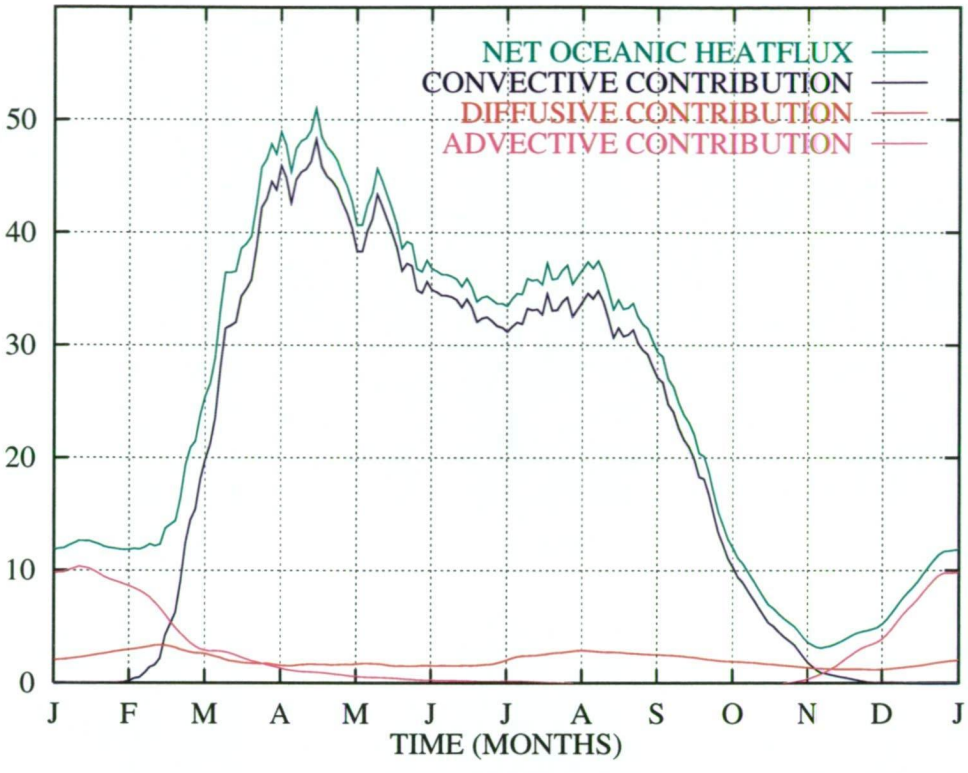

Fig. 5.4: Seasonal cycle of net oceanic heat flux (W m^{-2}) averaged over the last 3 years of the reference simulation.

half the Southern Ocean sea-ice zone. In the period October–February the oceanic heat flux is quite low almost everywhere, although in the Ross Sea the oceanic heat flux is high throughout the year. This indicates that the Ross Sea is an area of strong oceanic convection.

The barotropic streamfunction averaged over the final year of the simulation is shown in Figure 5.6. The massflux through Drake passage is approximately 140 Sv, which is in reasonable agreement with observations (e. g. Whitworth and Peterson, 1985), but this is not a surprising result because of the short period of integration. As the focus of this study is on the upper ocean/sea-ice interaction these short integration times are sufficient. A strong gyre is also present in the Weddell Sea, with lesser gyres in the Ross Sea and also at 90°E.

It is hoped that the initialization of the ocean model from climatology

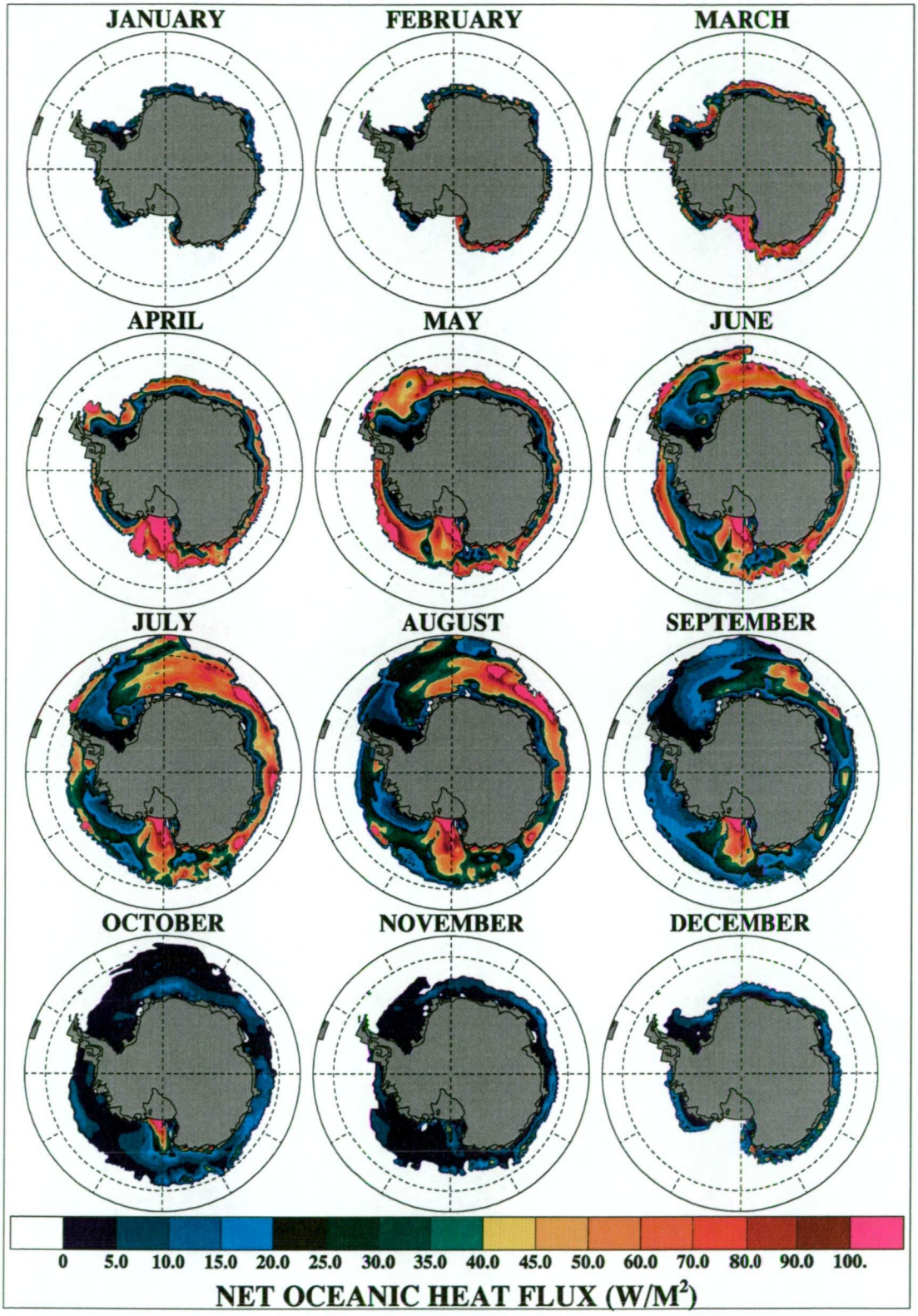

Fig. 5.5: Mean monthly spatial distribution of net oceanic heat flux in the 5^{th} year of the reference simulation.

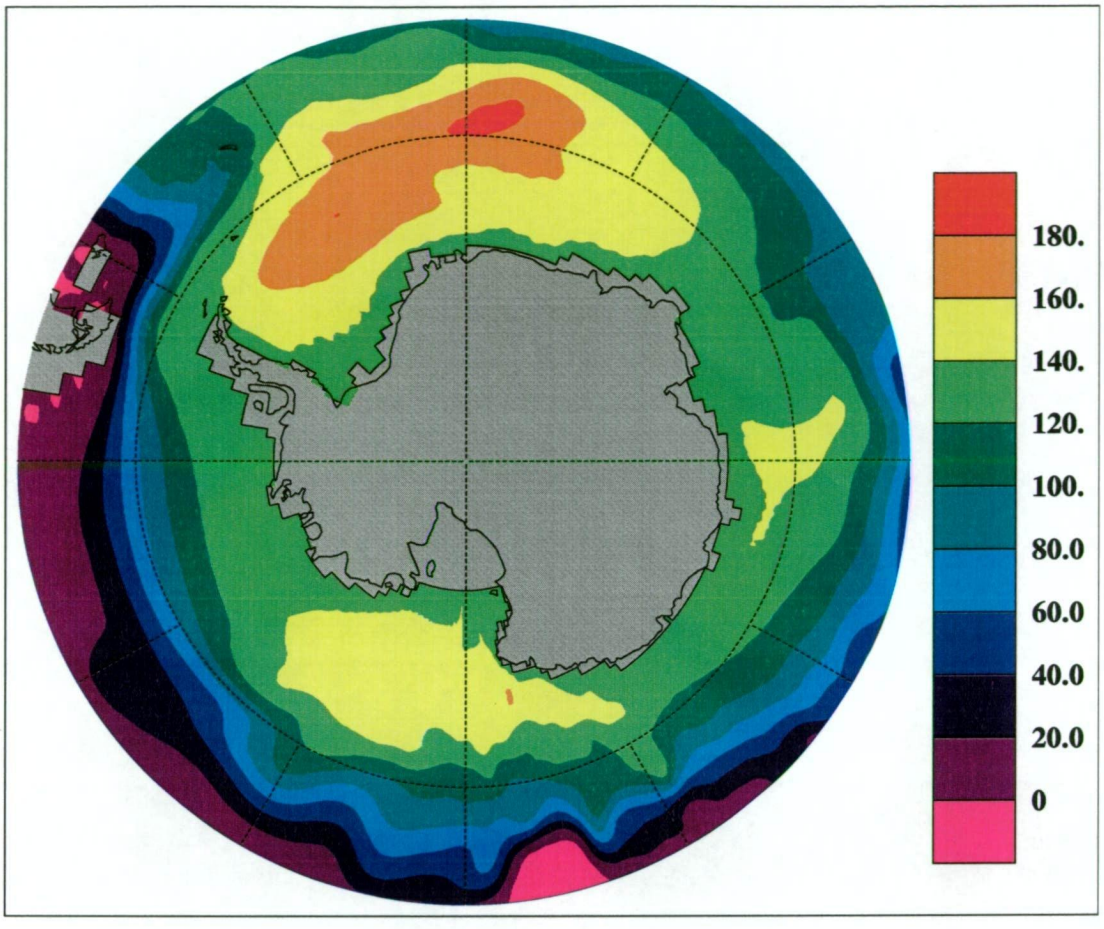

Fig. 5.6: Barotropic streamfunction (Sv) averaged over the final year of the reference simulation.

in combination with the short time-scale of the integration described here results in a coupled system that is in reasonable agreement with the real world. Unfortunately numerical model's of climate systems rarely behave exactly as might be wished for, and so it is useful to give some indication of the drift in key quantities during the course of the simulation. After the initial year, which is somewhat biased because of the initialization from a state of no sea-ice present, there is very little change in the annual cycle of sea-ice extent. This is also true for the oceanic heat flux and it's component terms. The annual maximum sea-ice volume increases almost linearly each year, from around 8.6×10^{12} m^3 in the first year to around 9.4×10^{12} m^3 in the final year. The increase in sea-ice volume is attributed to the build up

of thick sea-ice, approaching 5 m, at the coastal boundaries in the Western Weddell and Ross Seas. As a measure of the circumpolar circulation, massflux through Drake Passage builds to around 140 Sv within 2 months and stays within 5% of this value for the remainder of the simulation. In the upper 6 model layers (280 m) the mean temperatures are dominated by the seasonal cycle of surface forcing and show no trend. However the water column does tend to warm slightly below this, except in the bottom model layer where cooling occurs. Salinity in the upper 6 layers tends to decrease slightly throughout the simulation, with increasing salinity in the thermocline waters (260–1000 m), and little change to the salinity in the deeper waters.

5.3 Sensitivity to Choice of Precipitation Minus Evaporation Climatology and the Inclusion of Glacial Meltwater

Six simulations using the Southern Ocean Sector Model have been run to test for sensitivity of the coupled ocean/sea-ice system to variations in surface fresh water flux (SFWF). The first three only differ in the source of precipitation minus evaporation climatology. The second three are repeats of the first three but with the addition of glacial meltwater to the SFWF. Mean monthly precipitation minus evaporation rates for the Southern Hemisphere were obtained from output of the CSIRO 9 level coupled atmosphere/sea-ice/ocean model (McGregor *et al.*, 1993), from the Australian Bureau of Meteorology's Global Atmospheric Assimilation and Prediction (GASP) model (Bourke *et al.*, 1991), and from the European Centre for Medium-Range Weather Forecasting (ECMWF) Re-analysis Level III-B Global Atmospheric Data Archive (ERA, 1997). In each case the model was initialised with the ocean at rest and no sea-ice cover, and run for 5 years from January 16^{th}. The seasonal sea-ice cover adjusts very quickly with a full cover developing in the first model year. Similar rapid adjustment has been reported by Wu *et al.* (1996) in a coupled atmosphere/sea-ice model of the Southern Hemisphere subjected to instantaneous sea-ice removal.

Figure 5.7 shows the net annual precipitation minus evaporation (P–E) over the Southern Ocean seasonal sea-ice region for the CSIRO 9, GASP, and ECMWF climatologies. Horizontal resolution of the original data was rhomboidal 21 wave spectral truncation (CSIRO 9), rhomboidal 31 wave spectral truncation (GASP), and on a 2.5 × 2.5 degree latitude/longitude grid (ECMWF). There is a pronounced low in P–E over the Ross Sea (180°E) in all three climatologies (though somewhat weaker in the GASP case). The ECMWF re-analysis shows significantly less fresh water flux in the Wed-

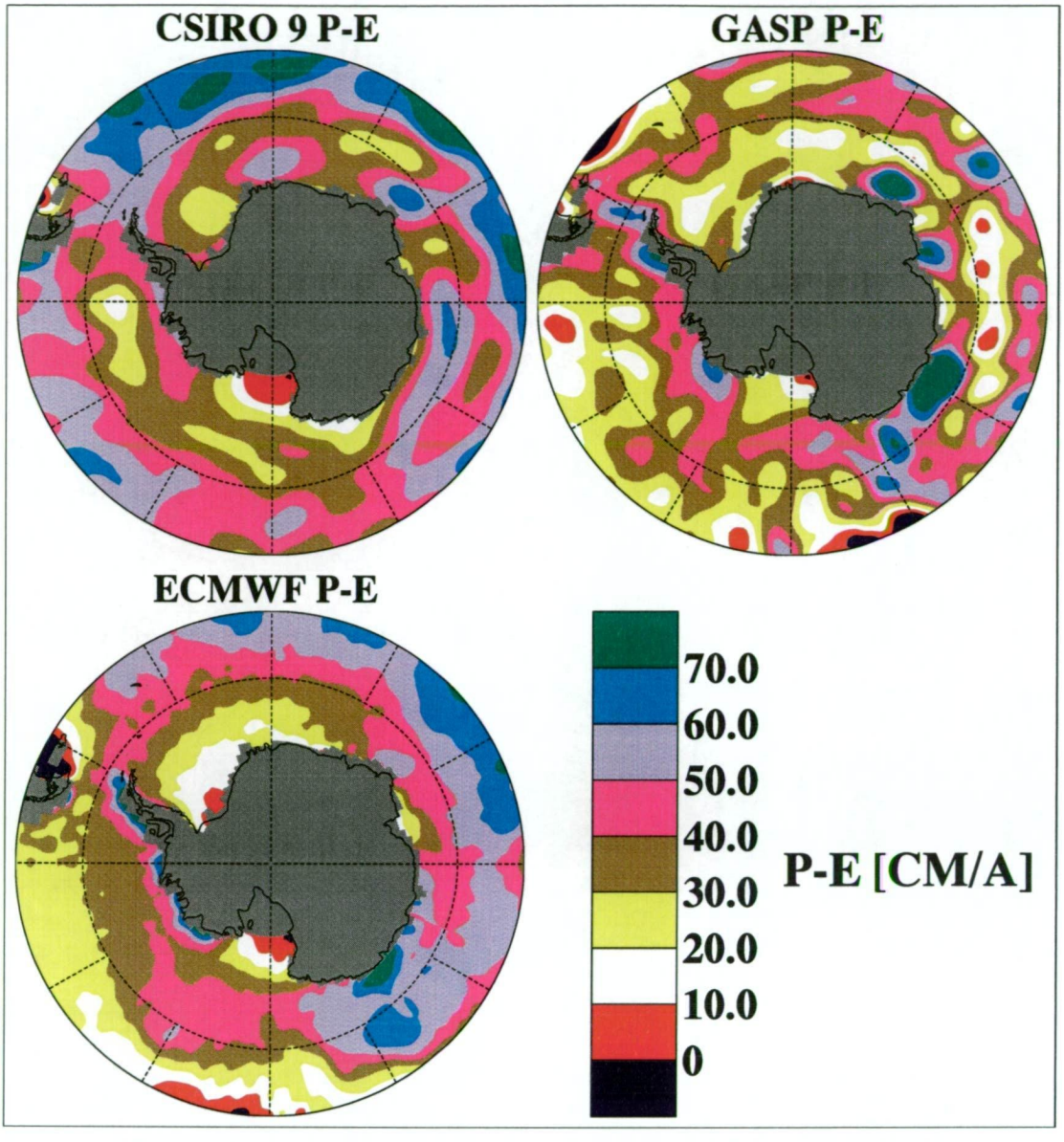

Fig. 5.7: Net annual P–E fields from the CSIRO 9 model climatology for the decade 1981–90, the GASP model twice daily analyses from December 1989 to November 1992, and the ECMWF Re-analysis Data Archive for 1979 to 1993. The region south of 50°S is shown.

dell Sea, while the CSIRO 9 values are noticeably higher in the region of Maud Rise (0°E). The GASP climatology is the most spatially variable of the three, perhaps due to it's relatively short time history or higher horizontal resolution. The P–E rate is relatively high along the coastline of East

Antarctica (the region considered in the high-resolution re-entrant channel model in Chapter 3) compared to other regions at a similar latitude in all three climatologies.

Häkkinen (1995) notes that precipitation minus evaporation is the least well known aspect of the Southern Ocean surface climatology. Fichefet and Morales Maqueda (1997a) remarked that in light of the sensitivity of snow-ice production in their coupled sea-ice/mixed-layer/pycnocline model to changes in precipitation rate in the Antarctic, that it was somewhat disturbing that the few precipitation climatologies available differ so much from one another over the Southern Ocean. In particular they point out that the climatologies of Jaeger (1976) and of Legates and Willmott (1990) differ by more than 100% in some zonally averaged mean monthly values south of 60°S.

Precipitation and evaporation alone do not account for the total fresh water flux in the Southern Ocean. Gordon (1981), using estimates of P–E over the Antarctic glacial mass and the assumption that the total glacial mass is constant in time, determines that glacial runoff and the associated iceberg melt provide an additional 10 cm a^{-1} of SFWF to the ocean area between 60 and 70°S. To investigate the model's sensitivity to this glacial contribution to the SFWF, the simulations forced with the CSIRO 9, GASP, and ECMWF mean monthly P–E climatologies have been repeated, but with the addition of 10 cm a^{-1} of glacial meltwater to the region south of 60°S in each case.

A demonstration of the model sea-ice sensitivity to variations in SFWF is shown in Figures 5.8 (sea-ice compactness) and 5.9 (sea-ice/snow layer thickness). Shown are the instantaneous sea-ice fields near the time of maximum sea-ice extent (September 1^{st}) in the 5^{th} year of each of the six simulations. The most striking feature of the sea-ice distribution in these simulations is the occurrence of a large scale polynya in the Weddell Sea

for the GASP and ECMWF P–E climatologies when glacial meltwater is not added to the SFWF, and the absence of such a polynya when glacial meltwater is added. That is, a small change in the SFWF (10 cm a^{-1}) can cause a large change in the sea-ice distribution in the model.

Figures 5.10 and 5.11 show the instantaneous model sea surface salinity (SSS) and sea surface temperature (SST), also on September 1^{st} in the 5^{th} model year. A local high in SSS occurs in the Weddell Sea for all six forcing scenarios. The SSS here is considerably higher (by approximately 0.2 psu) for the two simulations in which an open ocean polynya forms, which is also true for the SST. The greatest SSS occurs on the continental shelf of the Western Ross Sea and is above 34.7 psu. It is somewhat surprising that similar high SSS's are not also found on the continental shelf of the Western Weddell Sea in the model. The presence of a broad continental shelf with a western topographic barrier is regarded as an important factor for Antarctic Bottom Water (AABW) formation in both the Weddell and Ross Seas (Carmack, 1986). Gill (1973) gives a good review of the types of processes that may be involved in AABW formation. He shows that very cold shelf water increases in salinity as it moves westwards along the shelf, and then mixes with much warmer (but very salty) Circumpolar Deep Water (CDW) as it flows down the continental slope. It is possible that the model's coarse horizontal resolution in the Weddell Sea is not able to adequately resolve the presence of the continental shelf and the bottom water formation processes that one would expect to occur there, whereas the considerably higher horizontal resolution used in the Ross Sea region is.

In the open ocean polynya state deep convection results in vertical homogenization of the thermohaline fields. Figure 5.12 shows this by comparing a north-south section of instantaneous ocean salinity for the GASP P–E forced simulations with and without the glacial meltwater contribution. Deep convection associated with the polynya at 68°S results in a vertically homogeneous salinity column that reaches to the ocean floor in the simula-

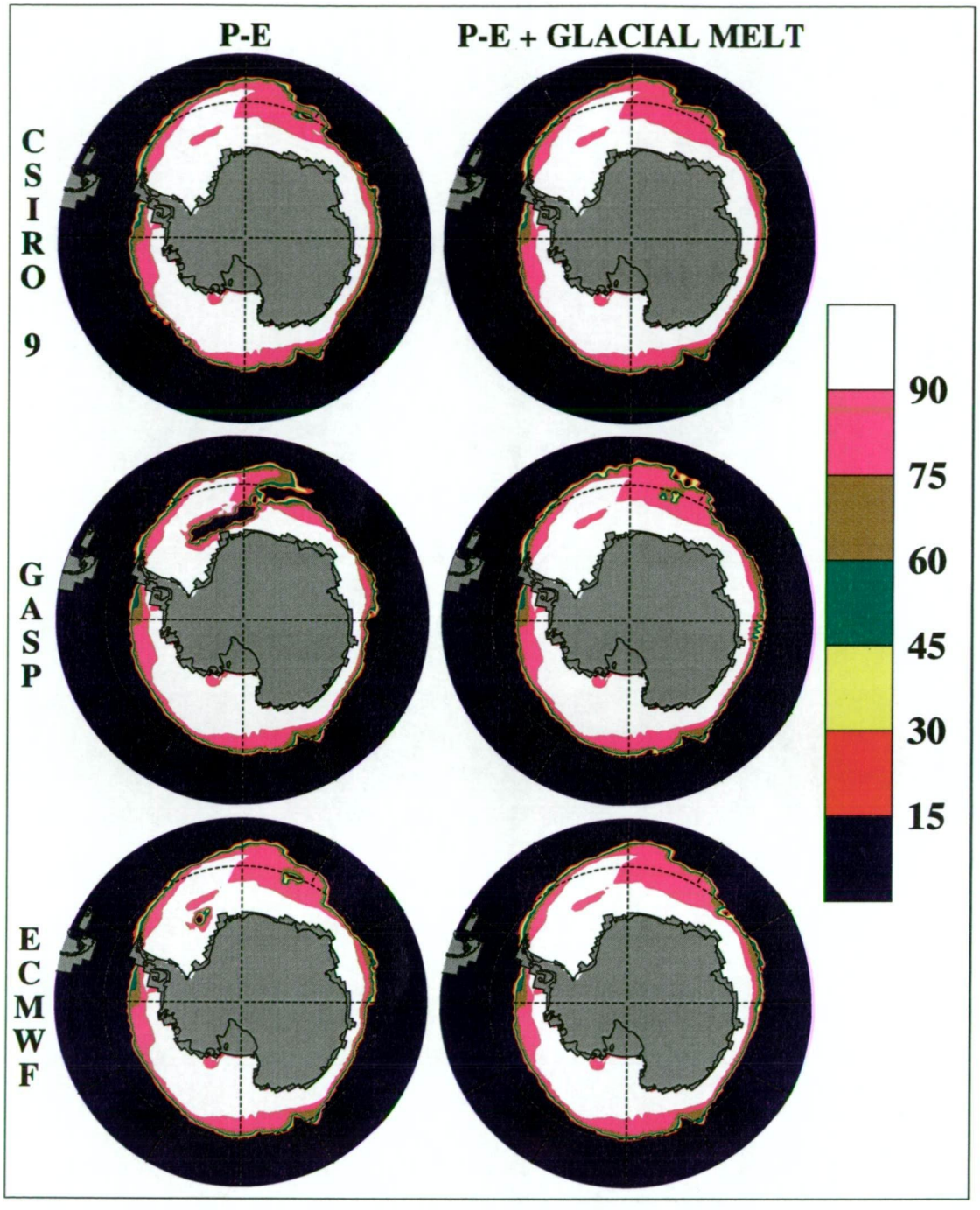

Fig. 5.8: Sea-ice compactness (%) near the time of maximum sea-ice extent in the 5^{th} year for CSIRO 9 (top row), GASP (middle row) and ECMWF (bottom row) precipitation minus evaporation (P–E) climatologies. In each row the plot on the left shows the case where only the relevant P–E climatology is used as SFWF and the plot on the right shows the case where 10 cm a^{-1} of glacial meltwater has been added to the SFWF in the region south of 60°S.

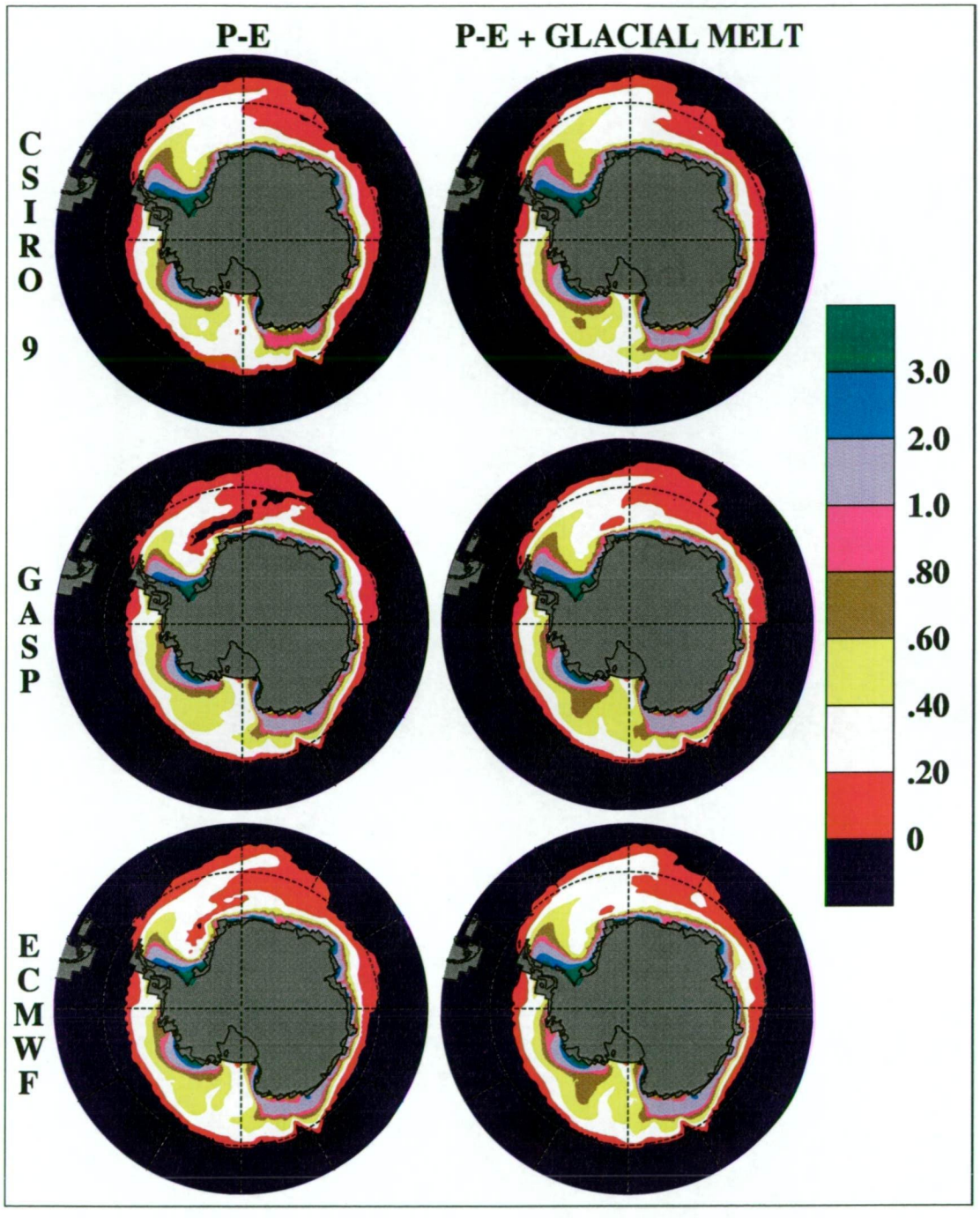

Fig. 5.9: Same as Figure 5.8 but for thickness of the sea-ice/snow layer (m). Large-scale polynyas form in the Weddell Sea for the GASP and ECMWF P–E climatologies when glacial meltwater is not added to the SFWF.

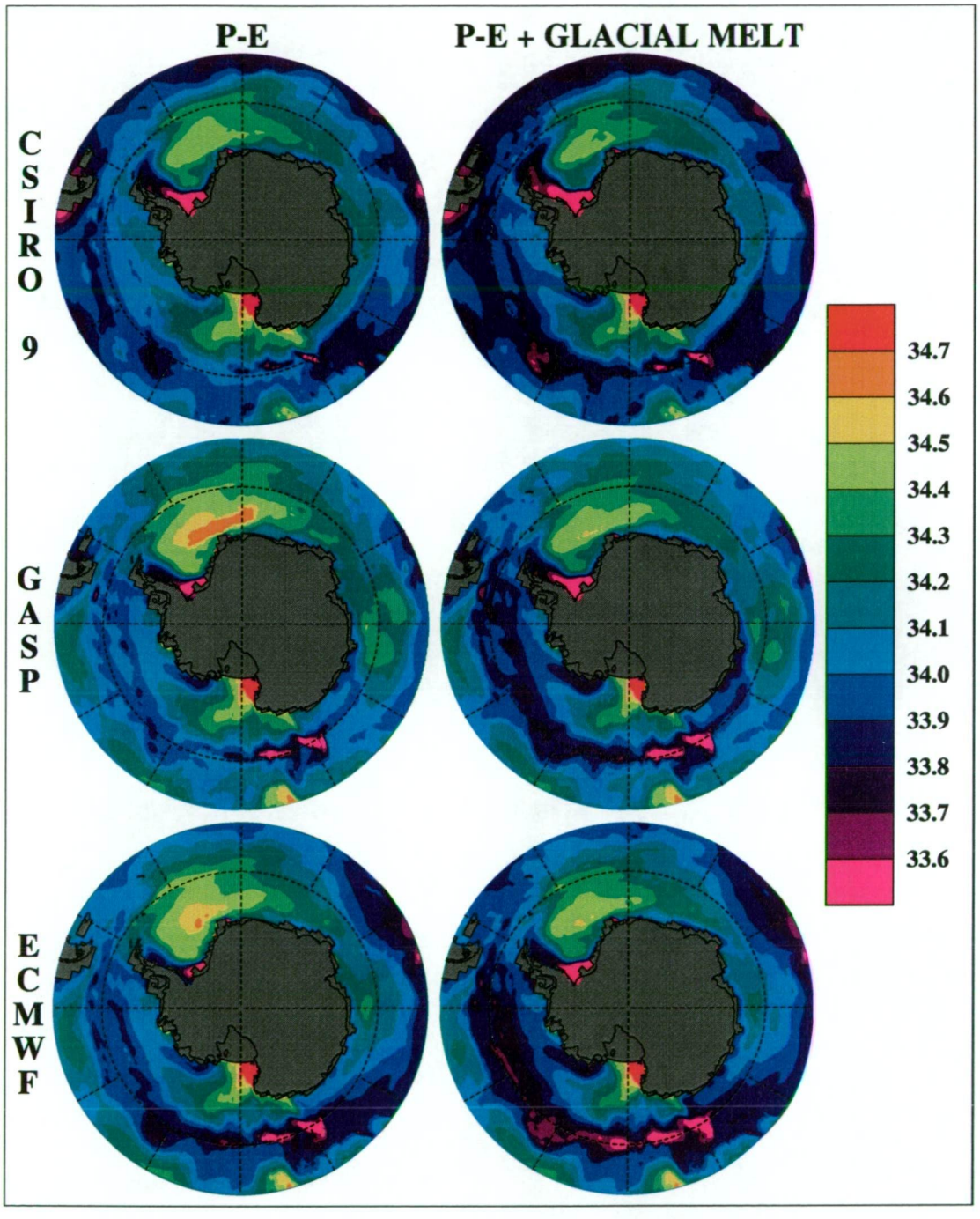

Fig. 5.10: Same as Figure 5.8 but for sea surface salinity (psu).

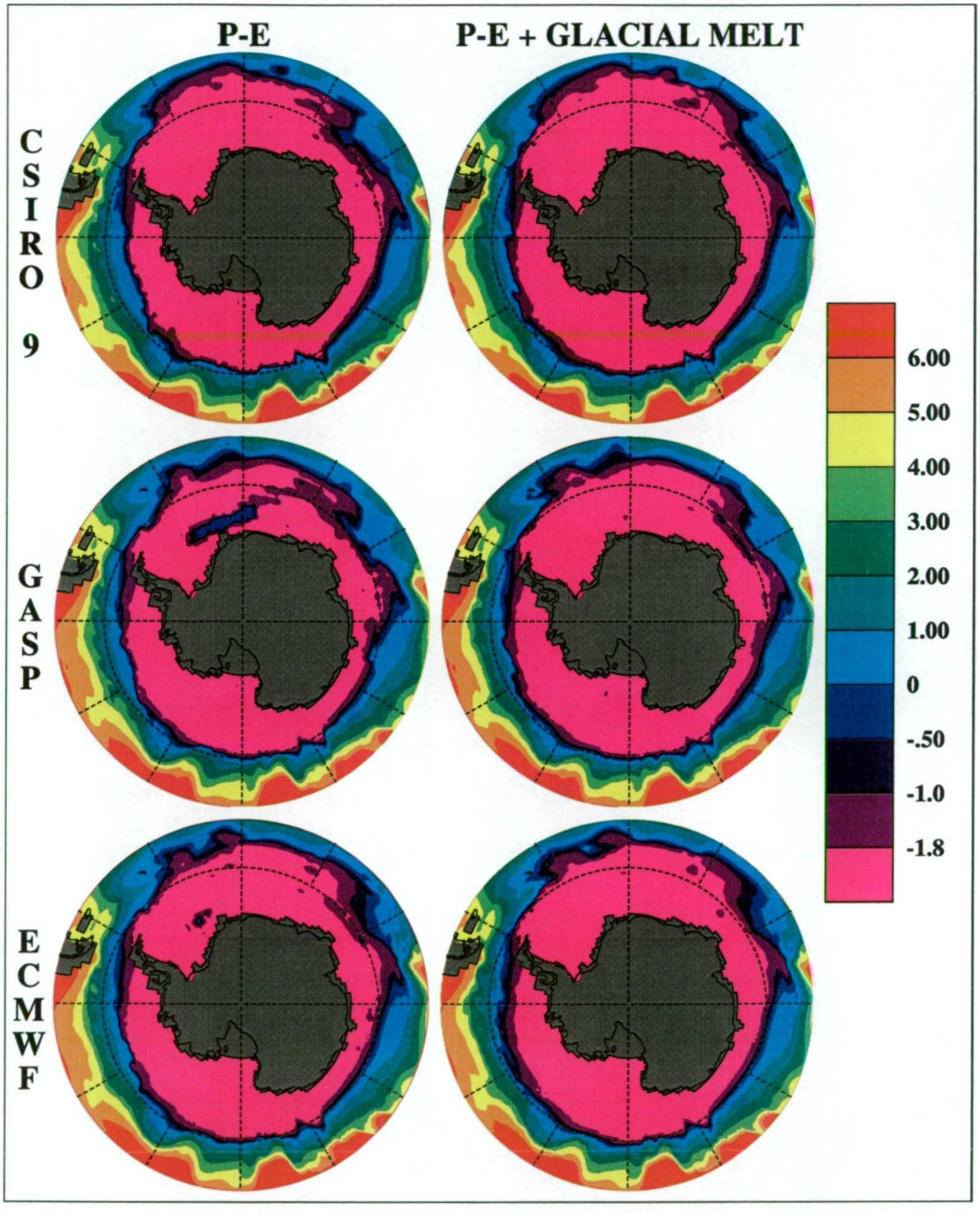

Fig. 5.11: Same as Figure 5.8 but for sea surface temperature (SST in °C). SST is well above the ocean freezing temperature within the large scale polynyas.

tion where no glacial meltwater is added to the surface fresh water forcing. This results in SSS and SST taking on the properties of the CDW. Such water is too warm for sea-ice formation and hence the polynya occurs

Figure 5.13 further highlights the sensitivity of the Southern Ocean sea-ice distribution to modifications of the SFWF forcing. Here the 5 year simulations using ECMWF P–E and ECMWF P–E plus 10 cm a^{-1} have been repeated for the cases of a uniform reduction in SFWF of 20 cm a^{-1} and 10 cm a^{-1}, and for the cases of a uniform increase in SFWF of 20 cm a^{-1} and 30 cm a^{-1}. This gives a set of 6 model runs in which the SFWF modification ranges from – 20 to + 30 cm a^{-1} with increments of 10 cm a^{-1} between simulations. In each case the SFWF modification is applied uniformly in time and space to the region south of 60°S. Once again it is found that small changes in the SFWF can lead to large differences in the modelled sea-ice extent. For the case of a modification of – 10 cm a^{-1} the modelled Weddell Polynya covers most of the Weddell Sea. When the SFWF is reduced by 20 cm a^{-1} the polynyas in both the Weddell and Ross Seas increase to the point of becoming embayments where no sea-ice formation occurs. Such a response suggests that the Weddell and Ross Seas are the most marginally stable areas in the Southern Ocean for seasonal sea-ice formation, and hence least able to resist the onset of large-scale deep convection induced by sea-ice formation. On the other hand, when the SFWF is increased (+ 10 cm a^{-1}, + 20 cm a^{-1}, + 30 cm a^{-1} simulations) there is little difference in the sea-ice distribution at the time of maximum extent.

The Weddell Polynya (Figure 5.14) was observed by an Electrically Scanning Microwave Radiometer (ESMR) aboard the Nimbus 5 satellite in the years 1974–6 (Zwally *et al.*, 1979; Zwally *et al.*, 1983). The polynya was 2–3×10^5 km^2 in size and changed through a seasonal cycle of embayment, enclosure, growth and embayment (Carsey, 1980). It was centred at 0°E 67°S in 1974, 345°E 67°S in 1975, and 340°E 68°S in 1976 (Parkinson, 1983) and propagated westward at 1 ± 0.6 cm s^{-1} (Carsey, 1980). Comiso and Gordon

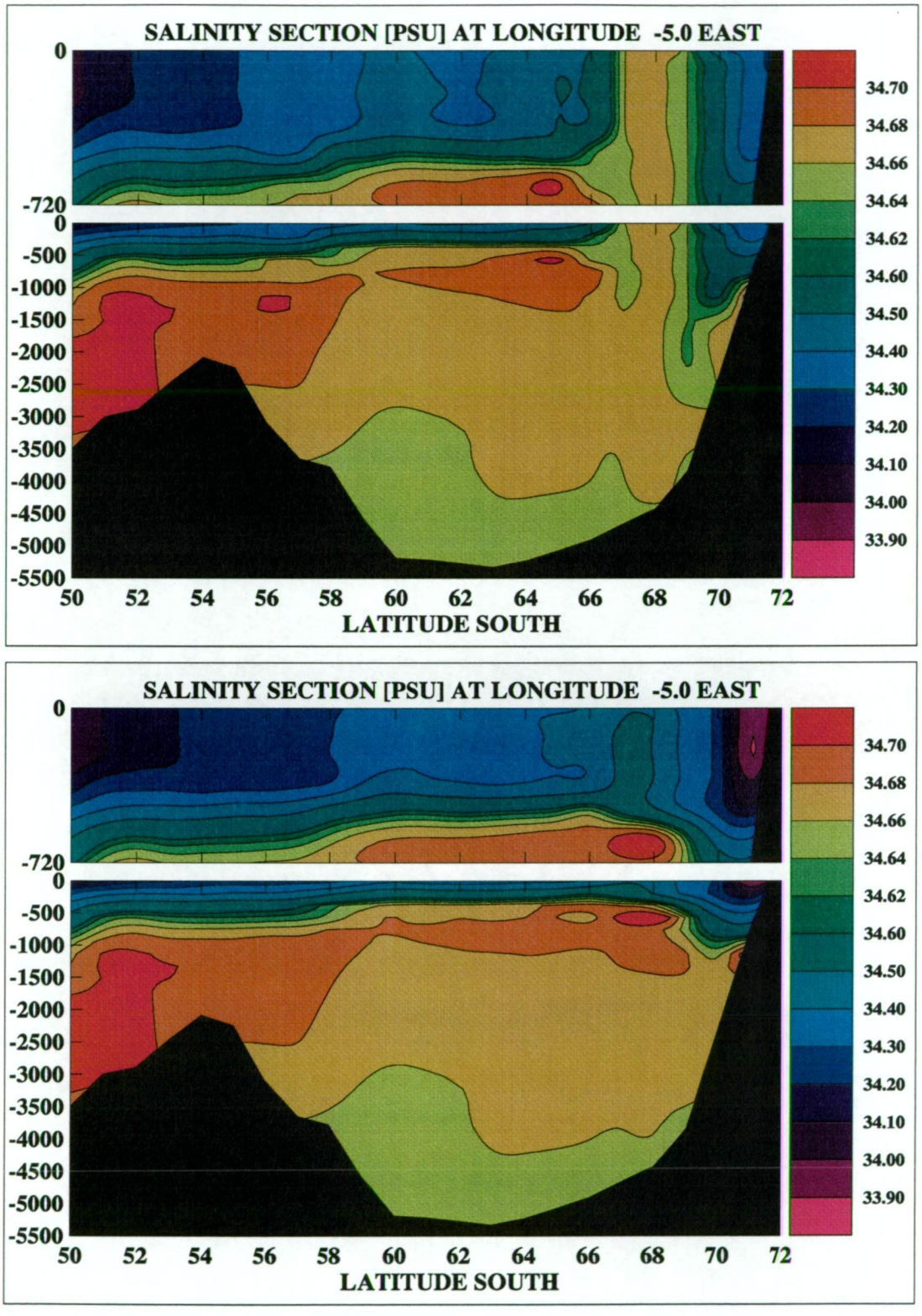

Fig. 5.12: Instantaneous meridional salinity section at 5°W for GASP P–E (top) and GASP P–E plus glacial meltwater (bottom), on September 1^{st} in the 5^{th} model year. Contour intervals are 0.1 psu except between 34.6 and 34.7 psu where they are 0.02 psu.

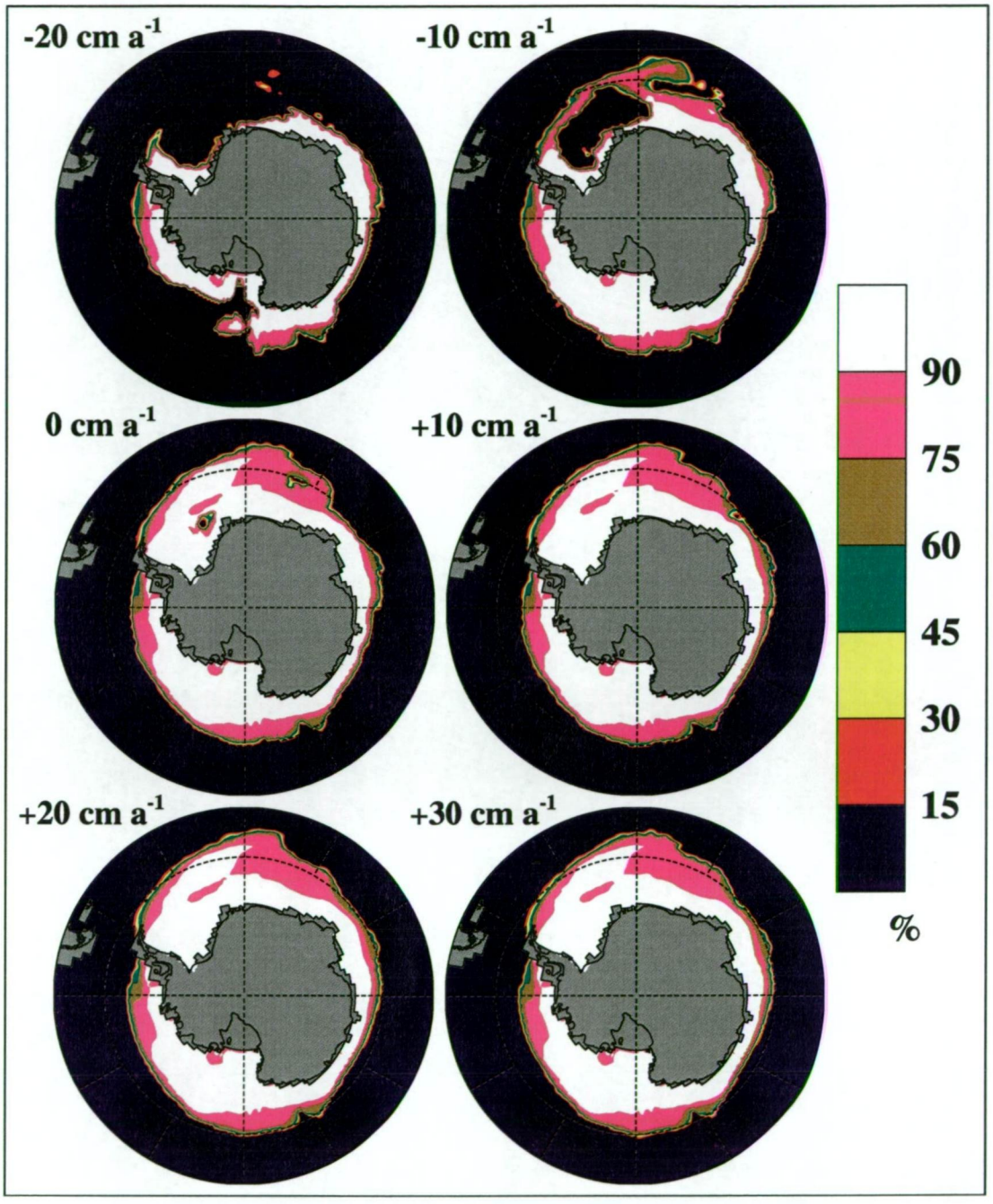

Fig. 5.13: Sea-ice compactness (%) near the time of maximum sea-ice extent in the 5^{th} year for simulations where the SFWF is derived from the mean monthly ECMWF P–E climatology modified by a constant in the region south of 60°S. The constant increments by 10 cm a^{-1} from – 20 cm a^{-1} (top left) to + 30 cm a^{-1} (bottom right).

(1987) note that there were also periods of reduced sea-ice concentration in the vicinity of Maud Rise in the Weddell Sea during 1980. The occurrence of a large scale polynya in the Ross Sea during December of each year from 1978–86 (except in 1979 when the polynya is replaced by an embayment of open water) can be seen clearly in the Nimbus 7 Scanning Multichannel Microwave Radiometer (SMMR) derived mean monthly sea-ice concentrations (Gloerson *et al.*, 1992). Onset of the Ross Sea Polynya shows up in the November mean monthly concentrations as an area of reduced (~40–70%) sea-ice cover in the far south of the Ross Sea.

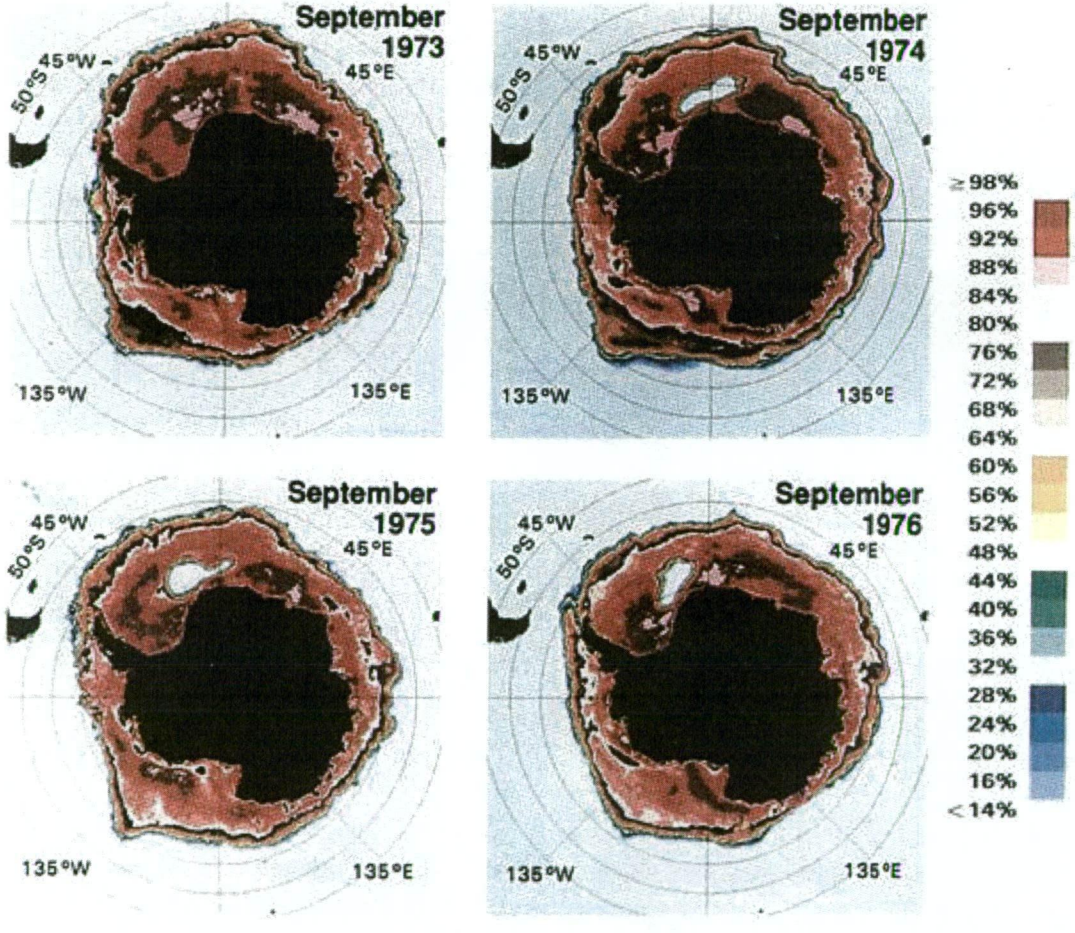

Fig. 5.14: September mean monthly Nimbus 5 ESMR satellite data of Southern Ocean sea-ice concentration for the years 1973–1976. A distinctive feature is the occurrence of a large polynya in the Weddell Sea during the years 1974–1976.

A number of studies have attempted to identify the physical mechanisms responsible for producing the Weddell Polynya. Carsey (1980) examines several hypotheses: that a perennial low pressure atmospheric state results in continual sea-ice divergence in the area; that sea-ice divergence is associated with a clockwise gyre driven by coastal winds; that the polynya is driven by oceanic heat provided by local eddies; and that there is a large scale oceanic gyre (standing eddy) resulting in oceanic upwelling. He concludes that it may be a complex combination of all of these that result in formation of the polynya. There is general agreement that the ocean thermohaline state must be preconditioned to support the presence of the Weddell Polynya (Carsey, 1980; Martinson *et al.*, 1981; Comiso and Gordon, 1987; Motoi *et al.*, 1987; Gordon and Comiso, 1988; Gordon and Huber, 1990; Martinson, 1990). Only in a 'thermal mode' ocean (Gordon, 1991), with the surface fresh water cap significantly eroded, will continual large scale polynya existence be possible in the presence of below freezing surface air temperatures. The Maud Rise region has been identified as being particularly sensitive to the development of such a 'thermal mode' ocean state because of frontal zone instabilities that are generated here (Gordon and Huber, 1984) and because of interactions between the local circulation and bottom topography (Gordon and Huber, 1990).

Parkinson (1983) used a coarse resolution ($\sim$200 km) regional sea-ice model similar to the one used by Parkinson and Washington (1979) to show that occurrence of the Weddell Polynya could be explained solely by variations in the wind forcing. Furthermore, she found that it was not the wind direction and its influence on the sea-ice dynamics that caused this, but rather the effect of wind speed on the sea-ice thermodynamics. Slow winds at the centre of high or low pressure systems moderate the exchanges of sensible and latent heat fluxes which restricts sea-ice formation. One problem with the Parkinson (1983) study is that the ocean heat flux was held constant throughout each simulation. As seen in Section 4.3 the ocean

heat flux is considerably higher in the 'thermal mode' ocean than elsewhere, due to the large convective upwelling of relatively warm Circumpolar Deep Water.

Based on the current study, it is likely that a negative anomaly in precipitation over Maud Rise in the early 1970's, in conjunction with the marginal stability typical of the area, would be sufficient cause for the observed Weddell Polynya. Motoi *et al.* (1987) proposed that this was a likely cause of the high summer mixed-layer salinity that they concluded was the primary cause resulting in the polynya's formation in 1974. That study used a one-dimensional convective mixed-layer model subjected to the mean monthly atmosphere/ocean and atmosphere/sea-ice heat flux climatology of Gordon (1981). It was found that for P–E less than a critical value of 40 cm a^{-1}, deep convection could be induced by surface cooling alone. This is considerably less than the 78 cm a^{-1} found by Martinson *et al.* (1981) with their convective model of the polynya. The sensitivity in this study suggests that the 40 cm a^{-1} value of Motoi *et al.* (1987) is more realistic (c. f. net annual P–E in the Weddell Sea for the GASP and ECMWF climatologies in Figure 5.7). For example the mean annual P–E south of 60°S in the region 30°W–30°E is approximately 30 cm a^{-1} in the ECMWF climatology. The 'thermal mode' ocean state tends to be self-perpetuating. As salty deep water rises to near the surface it is cooled to a point where it drives further deep convection. Martinson *et al.* (1981) point out that in order to terminate this polynya activity it is necessary to form a new surface fresh water cap either by increased precipitation or by convergence of sea-ice into the polynya area where it melts.

5.4 Sensitivity to Variations in Mean Surface Air Temperature

The two simulations using ECMWF P–E in Section 5.3, i. e. those with and without the addition of 10 cm a^{-1} glacial meltwater, are here repeated but with modified surface air temperature. Two case are considered, a uniform decrease of 2°C and a uniform increase of 2°C in the mean monthly CSIRO 9 surface air temperature forcing. For convenience, a naming convention for these experiments is given in Table 5.1. All of these simulations start from rest and are integrated for a period of 5 years. The sea-ice distribution at maximum extent in the final year of all six simulations is compared in Figure 5.15. The modelled Weddell Polynya appears in four out of the six simulations: as a small polynya near 335°E, 69°S in runs EC and ECP10P2; and as a larger polynya in the region 330-350°E, 67-70°S in runs ECM2 and ECP2. No Weddell Polynya forms in runs ECP10M2 and ECP10. It is interesting when comparing the three runs without glacial meltwater added to the SFWF (ECM2, EC and ECP2), that both an increase and a decrease in the surface air temperature will lead to an increase in the polynya area. There are two distinct processes responsible here. In experiment ECM2

Simulation	SFWF	ΔT_{air}
ECM2	ECMWF P–E	- 2°C
EC	ECMWF P–E	
ECP2	ECMWF P–E	+ 2°C
ECP10M2	ECMWF P–E + 10 cm a^{-1}	- 2°C
ECP10	ECMWF P–E + 10 cm a^{-1}	
ECP10P2	ECMWF P–E + 10 cm a^{-1}	+ 2°C

Tab. 5.1: Description of the six simulations used to investigate sensitivity of the sea-ice distribution to changes in surface air temperature (ΔT_{air}), and surface fresh water flux (SFWF).

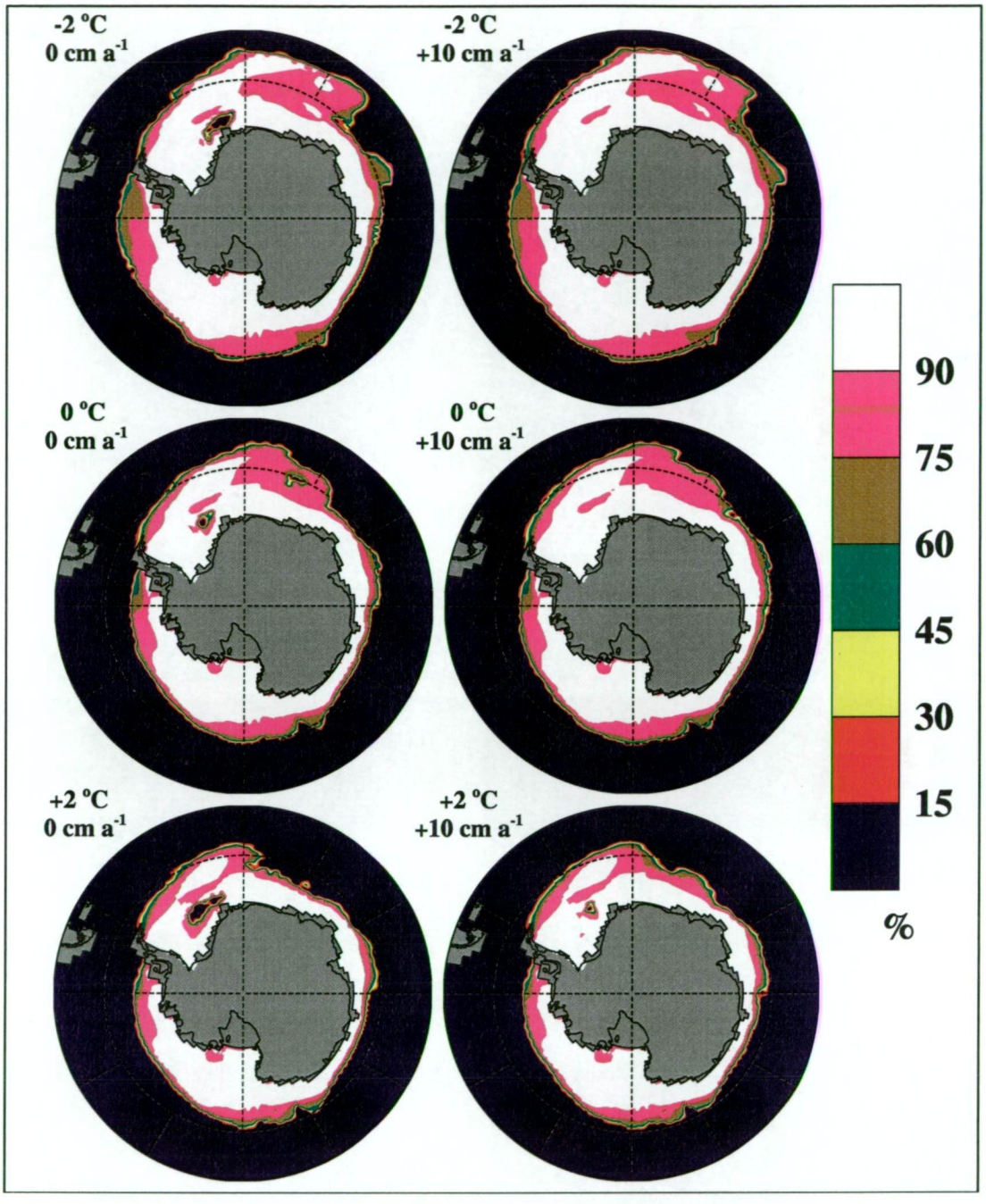

Fig. 5.15: Sea-ice compactness (%) near maximum extent in the 5^{th} year for simulations using the ECMWF P–E as SFWF (left column), and for simulations using the ECMWF P–E + 10 cm a^{-1} glacial meltwater south of 60°S (right column). Mean monthly surface air temperatures have been reduced by 2°C (top row) and increased by 2°C (bottom row), relative to the simulations using ECMWF P–E in Section 5.3 (middle row).

the reduced air temperature induces more sea-ice production (relative to experiment EC), and the associated increased level of brine rejection is responsible for enhancing convection and increasing the polynya size. For the case of increased air temperature (ECP2) the sea-ice formation rate and the associated convection rate are reduced (on the large scale), allowing the convective activity that is present in the already marginally unstable region of the ocean model to become more effective in maintaining the polynya.

Figure 5.16 shows timeseries of sea-ice extent and sea-ice volume averaged over the 5 years of the surface air temperature sensitivity simulations. Sea-ice extent is calculated as the sum of the areas of all grid cells containing sea-ice. For comparison the seasonal cycle of Southern Ocean sea-ice extent averaged over the lifetime of the SMMR satellite (October 26, 1978 to August 20, 1987) is also shown (Gloerson *et al.*, 1992). The greatest difference between the satellite data and the model output is that sea-ice melts much more rapidly in the model during October and November. Such behaviour was noted for the Arctic by Semtner (1976a) in his zero layer sea-ice thermodynamic model and was attributed to the lack of a parameterisation of heat storage within the sea-ice layer. As atmospheric surface temperatures warm in early spring some heat would go to warming the sea-ice interior whereas in the zero layer model all such heat is used for melting. The maxima in sea-ice extent from the simulations where surface air temperature is unaltered (i. e. runs EC and ECP10) are the closest to the satellite observed maxima. The model performs less well in reproducing the observed minimum sea-ice extent, with all six simulations underestimating this quantity.

Time mean sea-ice extents and volumes are given in Table 5.2. For both the SFWF cases considered it is found that an increase of 2°C in surface air temperature results in an 18% decrease in sea-ice extent, while a 2°C decrease in surface air temperature leads to a 23% increase in sea-ice extent. The sea-ice volume decreases by around 23% for the warming scenario, and increases by around 25% in the cooling scenario.

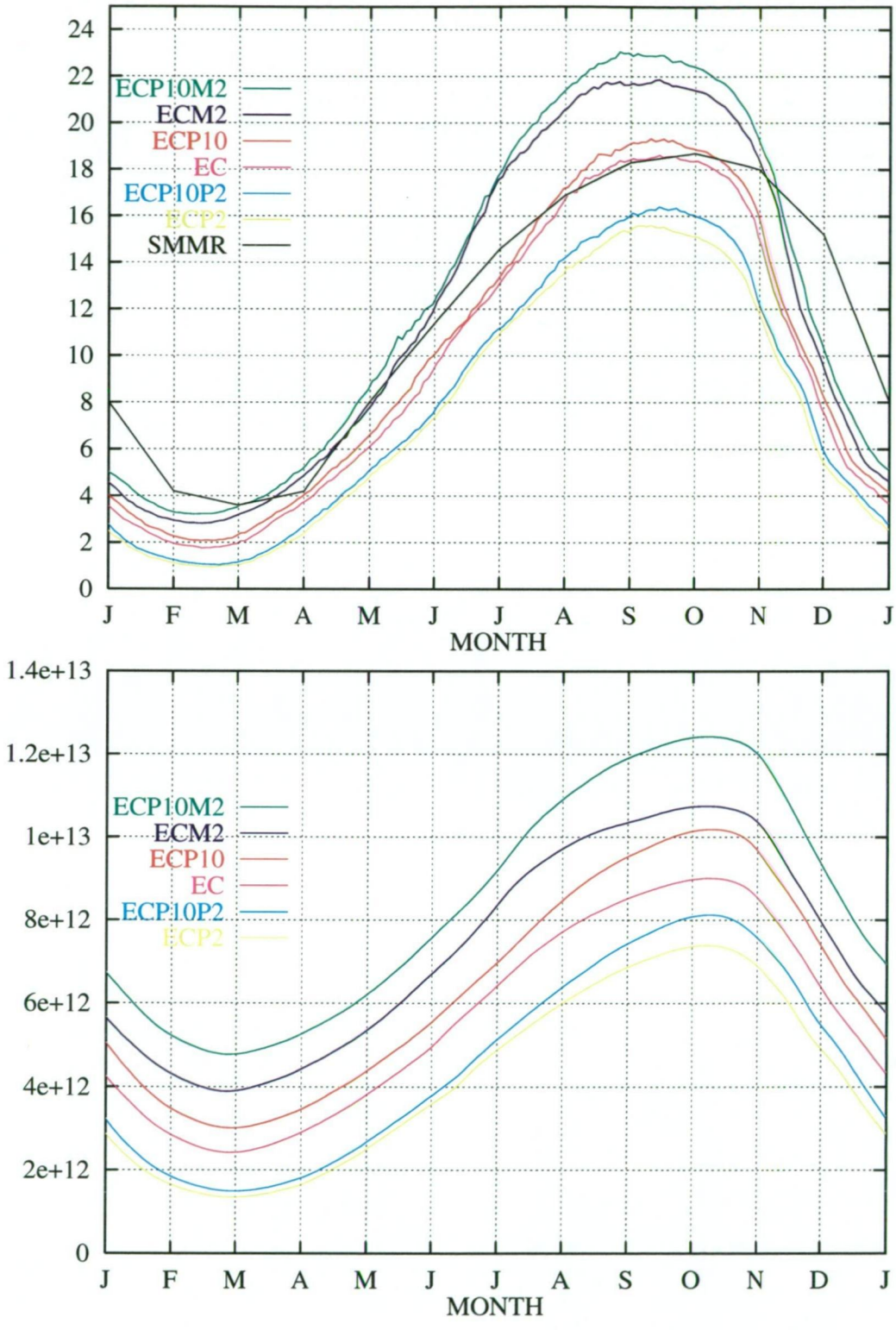

Fig. 5.16: Top: Total sea-ice extent (10^6 km^2) for the last year of each of the surface air temperature simulations, and averaged over the lifetime of the SMMR satellite observations. Bottom: Modelled sea-ice volume (m^3) for the corresponding period.

Simulation	EXTENT	VOLUME	OHF
ECM2	11.90	6.59	22.85
EC	9.67	5.31	25.00
ECP2	7.91	4.17	27.46
ECP10M2	12.51	7.41	20.51
ECP10	10.13	5.90	22.36
ECP10P2	8.28	4.51	24.84

Tab. 5.2: Mean sea-ice extent (10^6 km^2), mean sea-ice volume (10^{12} m^3), and time averaged net oceanic heat flux (W m^{-2}) for the surface air temperature sensitivity experiments. Averages are over the last 3 years of each 5 year simulation.

Figure 5.17 shows the net oceanic heat flux averaged over the last 3 years of the 5 year surface air temperature simulations. Within each SFWF scenario, increasing the air temperature increases the oceanic heat flux and decreasing the air temperature decreases the oceanic heat flux throughout most of the year. The opposite is true in the period of rapid melt, when the contribution to vertical stability by surface warming further enhances

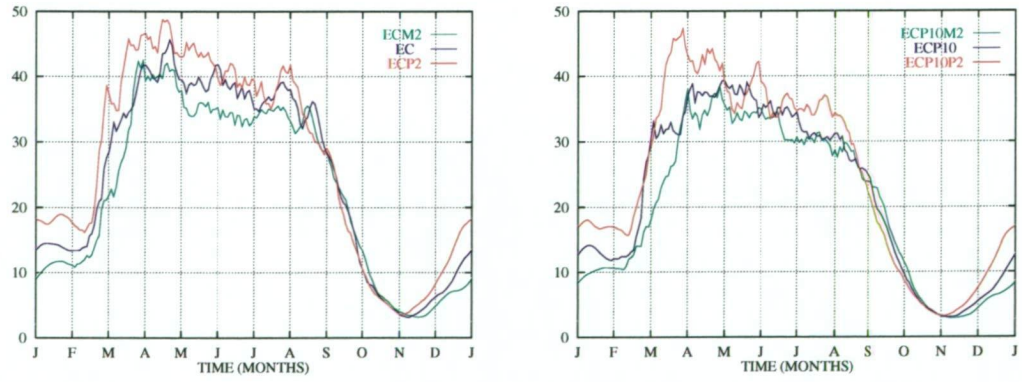

Fig. 5.17: Seasonal cycle of net oceanic heat flux (W m^{-2}) for the surface air temperature sensitivity simulations without glacial meltwater added to the SFWF (left), and with glacial meltwater added to the SFWF (right).

the contribution to vertical stability by the introduction of fresh (5 psu) melt water, and the convection rate becomes inversely proportional to the air temperature.

The mean net oceanic heat fluxes for this period are given in Table 5.2. For the 3 pairs of experiments in which only a change in SFWF is made the average decrease in net oceanic heat flux, corresponding to a 10 cm a^{-1} increase in SFWF, is 2.5 W m^{-2} (i. e. for $\bar{Q}_{net}^{ECP10M2} - \bar{Q}_{net}^{ECM2} = 2.34$ W m^{-2}, $\bar{Q}_{net}^{ECP10} - \bar{Q}_{net}^{EC} = 2.64$ W m^{-2}, and $\bar{Q}_{net}^{ECP10P2} - \bar{Q}_{net}^{ECP2} = 2.62$ W m^{-2}). Similarly, for the 4 pairs of experiments in which only a 2°C increase in T_{air} is considered, the average increase in net oceanic heat flux is 2.2 W m^{-2} (i. e. for $\bar{Q}_{net}^{EC} - \bar{Q}_{net}^{ECM2} = 2.15$ W m^{-2}, $\bar{Q}_{net}^{ECP2} - \bar{Q}_{net}^{EC} = 2.46$ W m^{-2}, $\bar{Q}_{net}^{ECP10} - \bar{Q}_{net}^{ECP10M2} = 1.85$ W m^{-2}, and $\bar{Q}_{net}^{ECP10P2} - \bar{Q}_{net}^{ECP10} = 2.48$ W m^{-2}). The mean net oceanic heat flux over the last 3 years of all 6 simulations is 23.8 W m^{-2}. Hence it is found that an increase in the SFWF of 10 cm a^{-1} reduces the net oceanic heat flux by approximately 10%, and an increase in the surface air temperature of 2°C increases the net oceanic heat flux by approximately 10%. The increase in surface air temperature results in a decrease in mean annual sea-ice extent and volume of around 20%, while the increase in SFWF results in an increase in mean annual sea-ice extent of around 5%, and an increase in mean annual sea-ice thickness of around 12%.

Coupled ocean/atmosphere models of transient climate change due to greenhouse warming predict an increase in both surface air temperature and P–E over the Southern Ocean sea-ice zone (Manabe and Stouffer, 1994; Hirst, 1999). Since the sensitivity of the sea-ice extent and volume, and of the oceanic heat flux, to increasing surface air temperature is opposite to that of increasing SFWF, it can be expected that these effects will partially offset each other. Consequently it is conjectured that sea-ice will maintain it's marginally stable role in the Southern Ocean for some time to come.

6. CONCLUSIONS

Before outlining the conclusions of this study it is pertinent to point out some of it's main limitations. One such limitation is that the large-scale feedback of the deep ocean has not been addressed. Regionality does not make this possible for the case of the East Antarctic model. In the Southern Hemisphere model it is the short time-scale of the integrations that preclude consideration of this. The short integration time is a trade off between the available computing resources and the number of sensitivity studies that could be performed. However, it is to be expected that the occurrence of massive oceanic convection in polar seas on longer time-scales would have considerable impact on the thermohaline characteristics of the deep water, through cooling and freshening. What feedback this may have on the sensitivity of the buoyancy stratification to the surface fresh water flux cannot be ascertained from this study, but requires consideration of much longer time-scale integrations, and ideally a global rather than hemispheric model domain.

A second limitation is the use of mean monthly rather than daily surface forcing data. As shown for example by Stössel *et al.* (1998), the use of synoptic time-scale atmospheric forcing data has a large impact on the simulation of the coupled ocean/sea-ice system in the Southern Ocean. They showed that the greater variability in winds led to higher rates of Antarctic Bottom Water formation and strengthening of the Southern Ocean meridional overturning cell, via the associated increase in the turbulent heat fluxes from ocean to atmosphere. Such a result suggests that the ocean/sea-ice

sensitivity to the surface fresh water flux may well be underestimated in the current study. However, it is also likely that convection is somewhat greater in primitive equation model's of polar seas than in the real world, which would act to offset any bias introduced into the current study by ignoring synoptic wind variability.

One final point is to clarify the decision on how to maintain the mean model salinity when making the massflux correction (due to net positive precipitation minus evaporation) in the East Antarctic model. How the salt lost when removing mass from the model domain should be added back into the model is not at all clear. In the real world precipitative mass is rapidly dispersed by gravity waves, and so does not affect the dynamics of the ocean via sea surface elevation, while the surface layer freshening remains to affect the thermohaline circulation. A simple approach would be to add the salt uniformly over the entire model domain. This approach was not used firstly because the ocean's density structure is highly nonlinear leading to difficulty in determining what the effect of this would be, and secondly because experimentation showed that this resulted in excessive salinification of the deep waters within the model. The addition of salt back to the upper 7 model layers, only in a sponge layer at the northern boundary, was found to avoid this problem, and is partly justified by simulating the meridional introduction of salt in the real world via the inflow of intermediate water at these depths. Perhaps a more realistic approach would also involve the extraction of salt at the northern wall in the deeper layers, in an attempt to simulate the meridional flow of mode and deep waters out of the model domain, but this is difficult without accurate knowledge of realistic rates of meridional salt transport for the model domain.

The main conclusions from this study are as follows:

Conclusion 1: *The magnitude of oceanic heat flux to the base of the sea-ice in the Southern Ocean exhibits considerable seasonal variability*

and spatial inhomogeneity. During the winter months this heat flux is dominated by oceanic convection.

The oceanic heat flux to the base of the sea-ice is important in determining the sea-ice thickness, and is also an indicator of both the strength of overturning of the thermohaline circulation and the subsequent water mass exchange rates in the Southern Ocean. For the high-resolution model, oceanic heat flux was found to have a spatially and temporally averaged mean of around 8 W m^{-2} in the East Antarctic region. The areal average oceanic heat flux was found to exhibit considerable seasonal variability. It's value approaches 20 W m^{-2} in winter and falls below 5 W m^{-2} in summer. Convection was found to be the dominant physical process in determining the magnitude of the oceanic heat flux throughout the winter, with advection and diffusion both playing some role in the summer. Also, the oceanic heat flux displayed considerable spatial variability. The greatest *in situ* oceanic fluxes of heat were found in the marginal sea-ice zone, due to convection in the winter months when new sea-ice forms over the deep ocean, and due to advection in the summer when the atmosphere warms the upper ocean through leads or in grid cells adjacent to the marginal ice zone. A local maximum in oceanic heat flux also occurs in the coastal polynya, with values up to 50 W m^{-2}.

While the seasonality of oceanic heat flux in the Southern Ocean Sector Model is very similar to that in the high-resolution model, the magnitude was found to be considerably greater. The space and time mean oceanic heat flux for the Southern Ocean was found to be around 25 W m^{-2}. The wintertime heat flux was around 35 W m^{-2} which is in reasonable agreement with limited observations of around 40 W m^{-2} (Gordon and Huber, 1990) for the Weddell Sea.

Conclusion 2: *The magnitude of oceanic heat flux to the base of East Antarctic sea-ice is robust for a range of P–E values that encompass*

what is estimated to be the actual P–E value to this region. However, when the P–E falls below a critical value, a thermal mode ocean with very little sea-ice cover results.

It was found in the East Antarctic model that the annual mean net oceanic heat flux, it's seasonal cycle and spatial variability are similar for constant precipitation minus evaporation rates in the range 25–100 cm a^{-1}. Compared to other regions at the same latitude, the East Antarctic region has a relatively high P–E, that falls within this range. For large values of constant P–E considered, increased vertical stability led to an increase in the diffusive flux of heat to the sea-ice, which significantly dampened the effect of less convection on the net oceanic heat flux. In some sense the ocean model has a certain amount of heat that is available to the sea-ice or atmosphere, determined by the vertical profile of the thermohaline fields, and in the model this heat will usually be transported to the sea-ice via convection. However, when convection is reduced due to increased stability, a vertical heat transport will nethertheless occur via diffusion, which results in a near equivalent net heat flux (a characteristic also pointed out by Martinson and Iannuzzi, 1998, for the Weddell Sea). This result was also found in the experiments considering changes in sea-ice salinity.

Only for a critical value of P–E below 25 cm a^{-1} will a thermal mode ocean state be induced. This is characterized by large-scale deep convection resulting in homogenization of the thermohaline properties of the water column and a complete breakdown of the oceanic mixed layer. Sea surface temperature rises above the freezing temperature due to the very large heat storage within the deep waters, and the seasonal sea-ice cover does not form. Cold surface air temperatures act to enhance the deep convection via cooling, leading to further mixing with relatively warm abyssal waters, but not to sea-ice formation.

Conclusion 3: *The Weddell Sea region was found to be the most marginally*

stably stratified region of the modelled Southern Ocean. The weak stability in this region results in the formation of a polynya similar to that observed via remote sensing satellite in the early 1970's, when the surface fresh water flux falls below a critical value that is similar in magnitude to the estimated P–E to this region.

It was found that a low anomaly in P–E during the early 1970's is a sufficient cause for the observed Weddell Polynya. Also it is noted that available climatologies do not generally provide sufficient P–E for the observed sea-ice cover that exists (apart from in the mid-1970's) in the Weddell Sea, and hence that the component of surface fresh water flux provided by glacial meltwater is an important component of the Southern Ocean's thermohaline stability. The physical process responsible for the polynya formation was the switching of the ocean state from a stable to a thermal mode (Gordon, 1991). This is a manifestation within the framework of a sophisticated numerical primitive equation model of earlier findings from observational work (Gordon and Huber, 1990) and analytical reasoning (Martinson, 1990). Also it was found that the critical value of SFWF for the Weddell Sea sector is around 35 cm a^{-1}. Two previous convective model studies have attempted to relate a critical value of surface fresh water flux to the onset of temperature-driven deep convection in the Weddell Polynya. The results from this study (Section 5.3) suggest that the 40 cm a^{-1} value of Motoi *et al.* (1987) is probably more accurate than the 78 cm a^{-1} found by Martinson *et al.* (1981).

Conclusion 4: *The sensitivity of oceanic heat flux, and of sea-ice thickness and extent in the Southern Ocean, to increasing P–E is opposite in sign to the sensitivity to increasing surface air temperature. These two sensitivities are expected to at least partially offset each other under an enhanced greenhouse effect global warming scenario.*

Surface exchanges of salt and fresh water in the Southern Ocean were

found to have a significant impact on the buoyancy of the underlying waters, and consequently to have a strong influence on the flux of oceanic heat to the base of the sea-ice, mainly via convection. When this sensitivity was compared to the sensitivity of the coupled ocean/sea-ice system to changes in the surface air temperature, it was found that increasing the air temperature and increasing the surface fresh water flux results in sensitivities of similar magnitude, but opposite sign, in terms of the ocean's response (vertical heat flux) and hence also in terms of the time mean behaviour of the sea-ice pack (extent and concentration). Quantitatively it was found that for oceanic heat flux a decrease in surface fresh water flux of 10 cm a^{-1} is roughly equivalent to an increase in the surface air temperature of 2°C. Both of these changes result in a 10% increase in the oceanic heat flux. For the 2°C warming this was accompanied by a 20% decrease in mean annual sea-ice extent and volume, implying that the change in air temperature affects the sea-ice concentration but not the thickness. For the 10 cm a^{-1} decrease in fresh water flux the sea-ice extent reduces by approximately 5% and the sea-ice concentration decreases by approximately 12%, implying that this change also affects the thickness of the sea-ice layer. As it is expected that both the surface air temperature and the surface fresh water flux over the Southern Ocean will increase in response to greenhouse induced global climate change, these two competing sensitivities will at least partially offset each other.

APPENDIX

A. SURFACE FORCING FOR THE HIGH-RESOLUTION MODEL

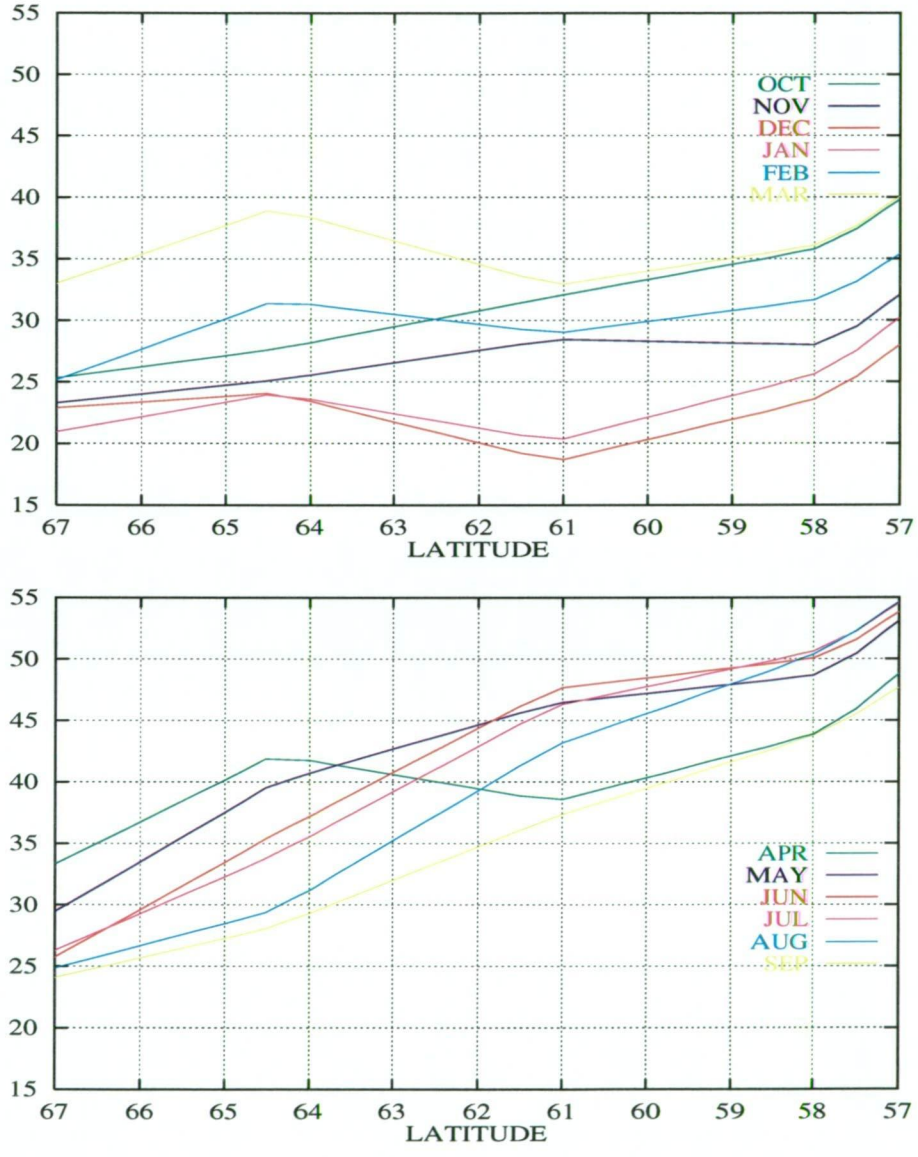

Fig. A.1: Mean monthly latent heat flux forcing (W m^{-2}) for the high-resolution model derived from output of the CSIRO 9 model.

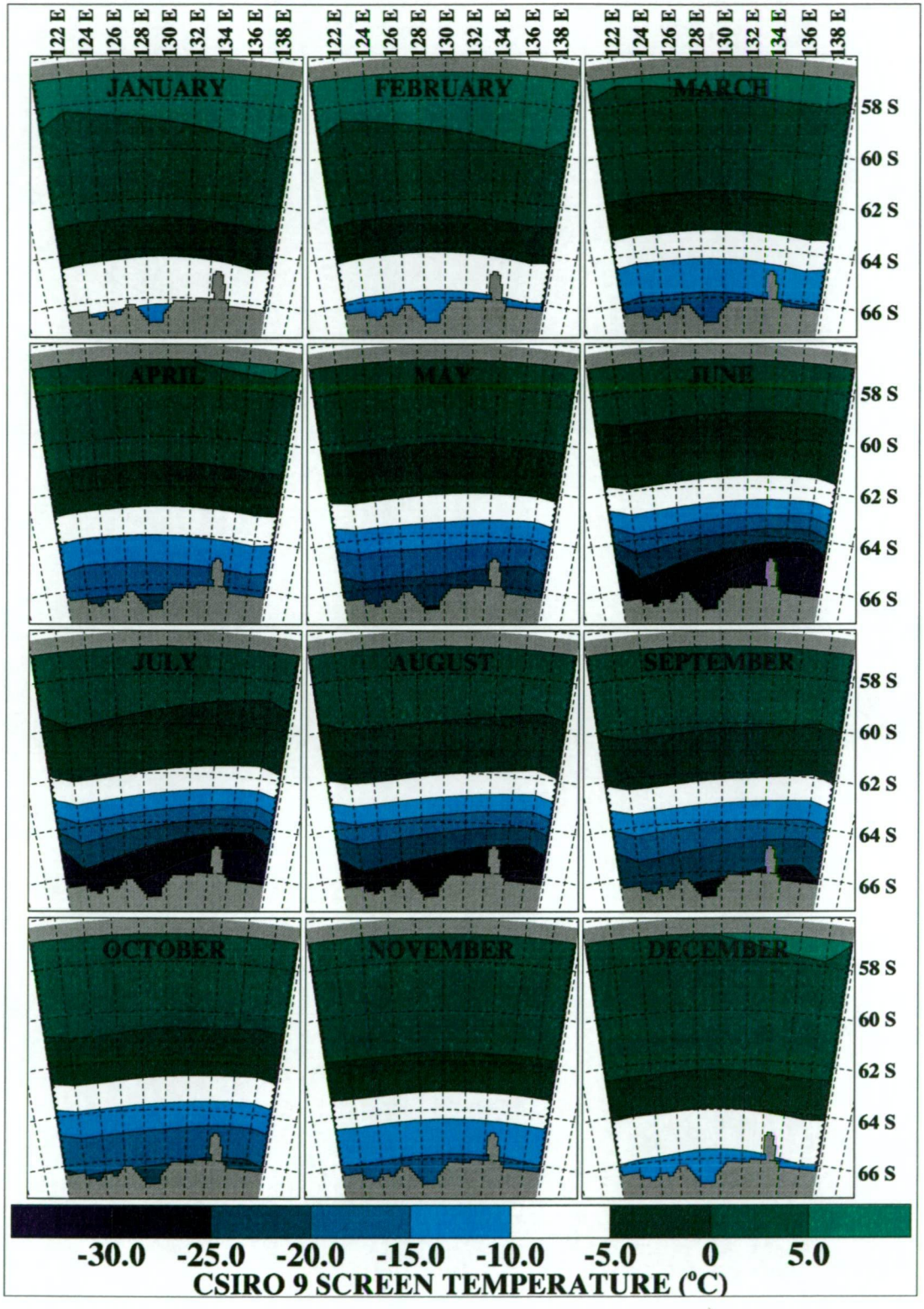

Fig. A.2: Mean monthly surface air temperature forcing (°C) for the high-resolution model derived from output (2 m screen temperature) of the CSIRO 9 model.

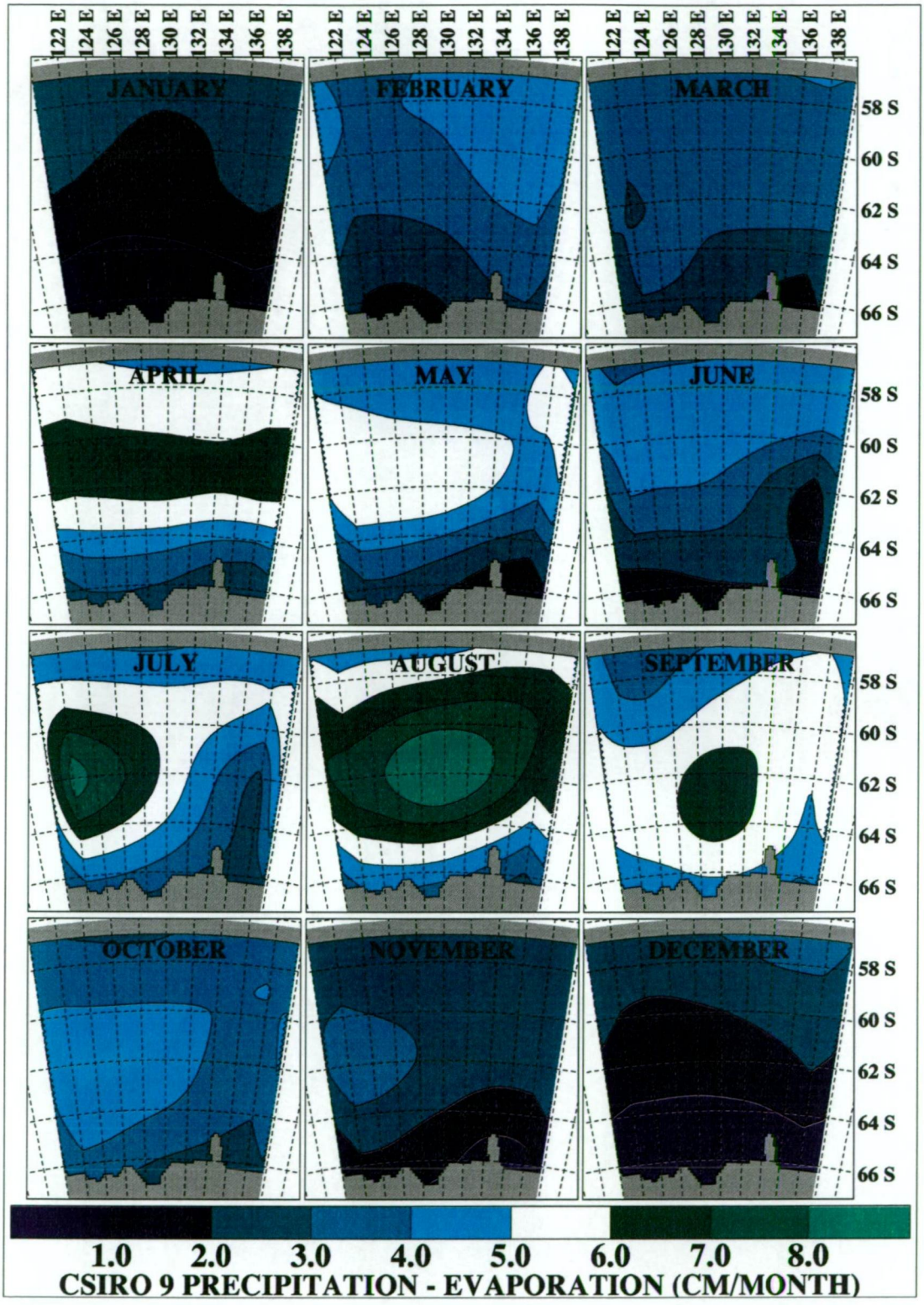

Fig. A.3: Mean monthly precipitation minus evaporation (cm month^{-1}) forcing for the high-resolution model derived from output of the CSIRO 9 model.

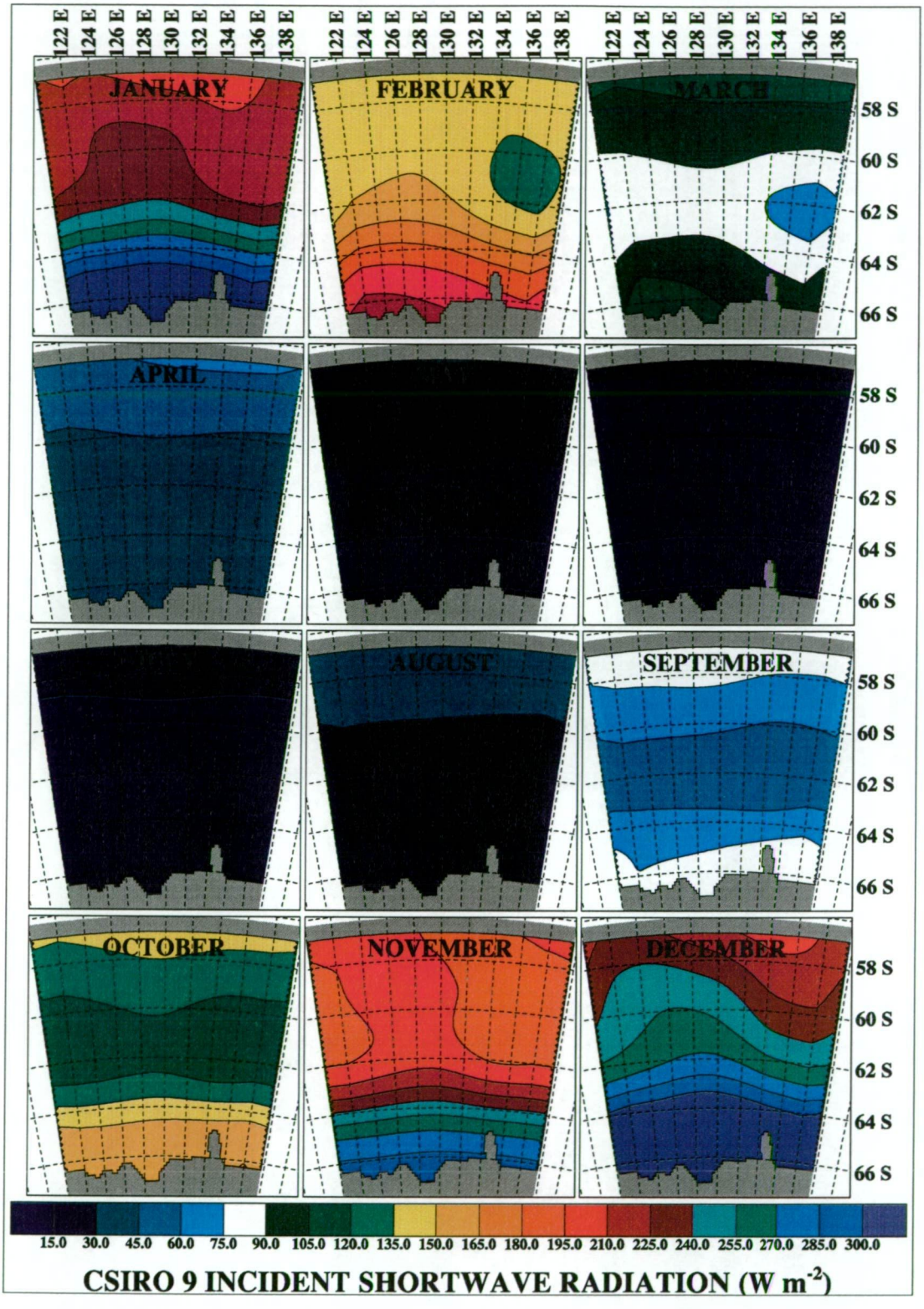

Fig. A.4: Mean monthly incident shortwave radiation (W m^{-2}) forcing for the high-resolution model derived from output of the CSIRO 9 model. Contour interval is 15 W m^{-2}.

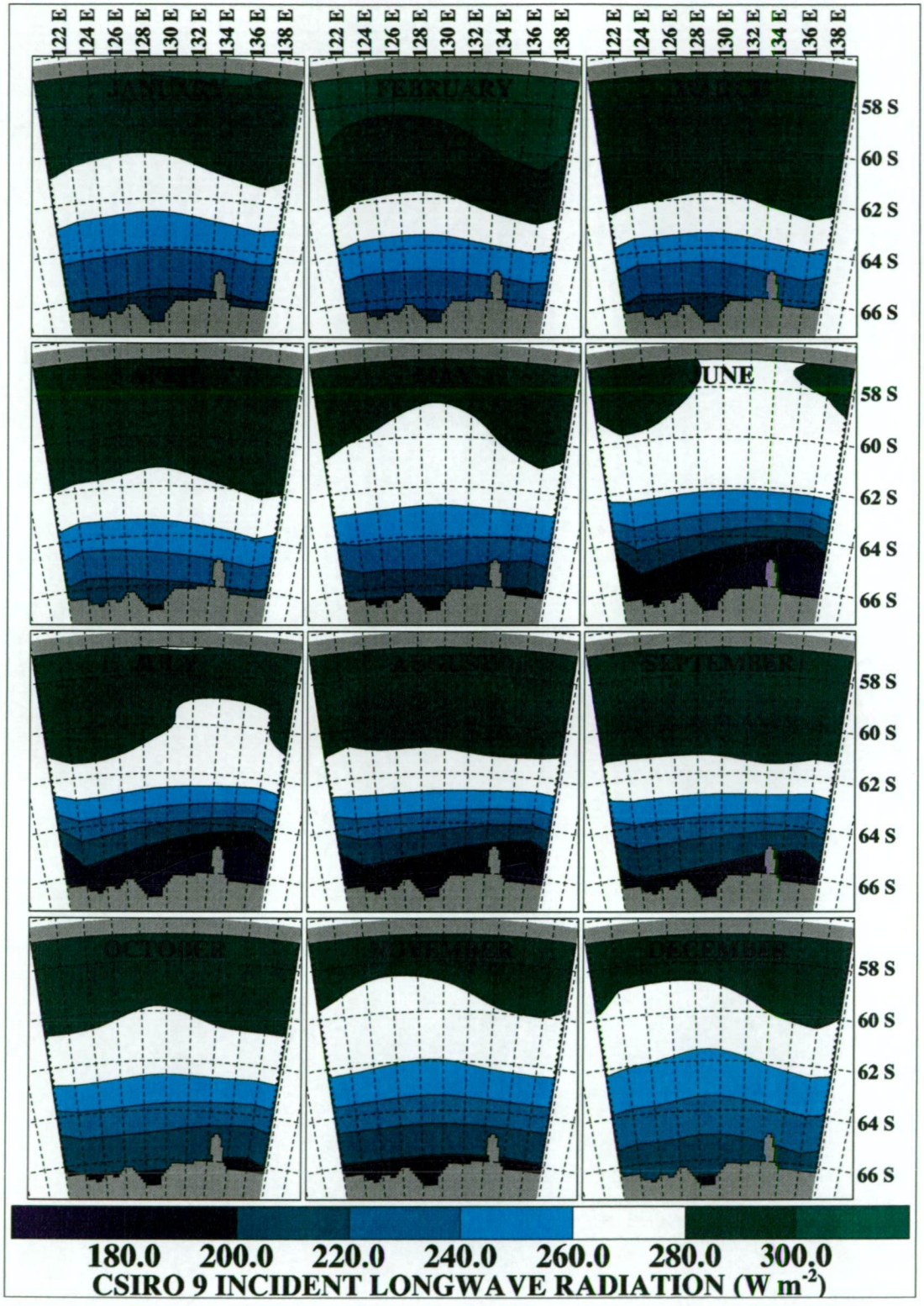

Fig. A.5: Mean monthly incident longwave radiation (W m^{-2}) forcing for the high-resolution model derived from output of the CSIRO 9 model.

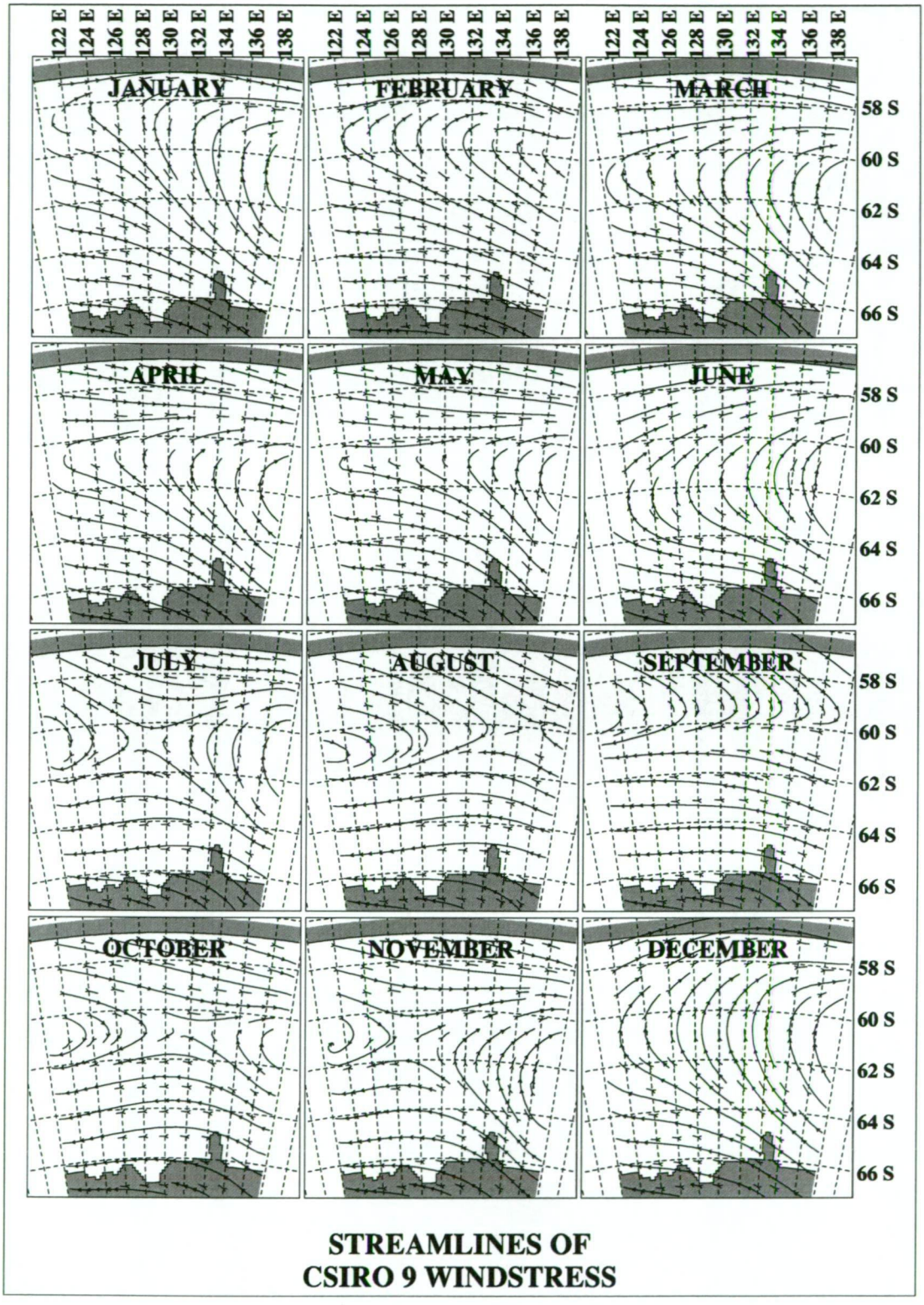

Fig. A.6: Streamlines of mean monthly wind stress forcing for the high-resolution model derived from output of the CSIRO 9 model.

B. SURFACE FORCING FOR THE SOUTHERN OCEAN SECTOR MODEL

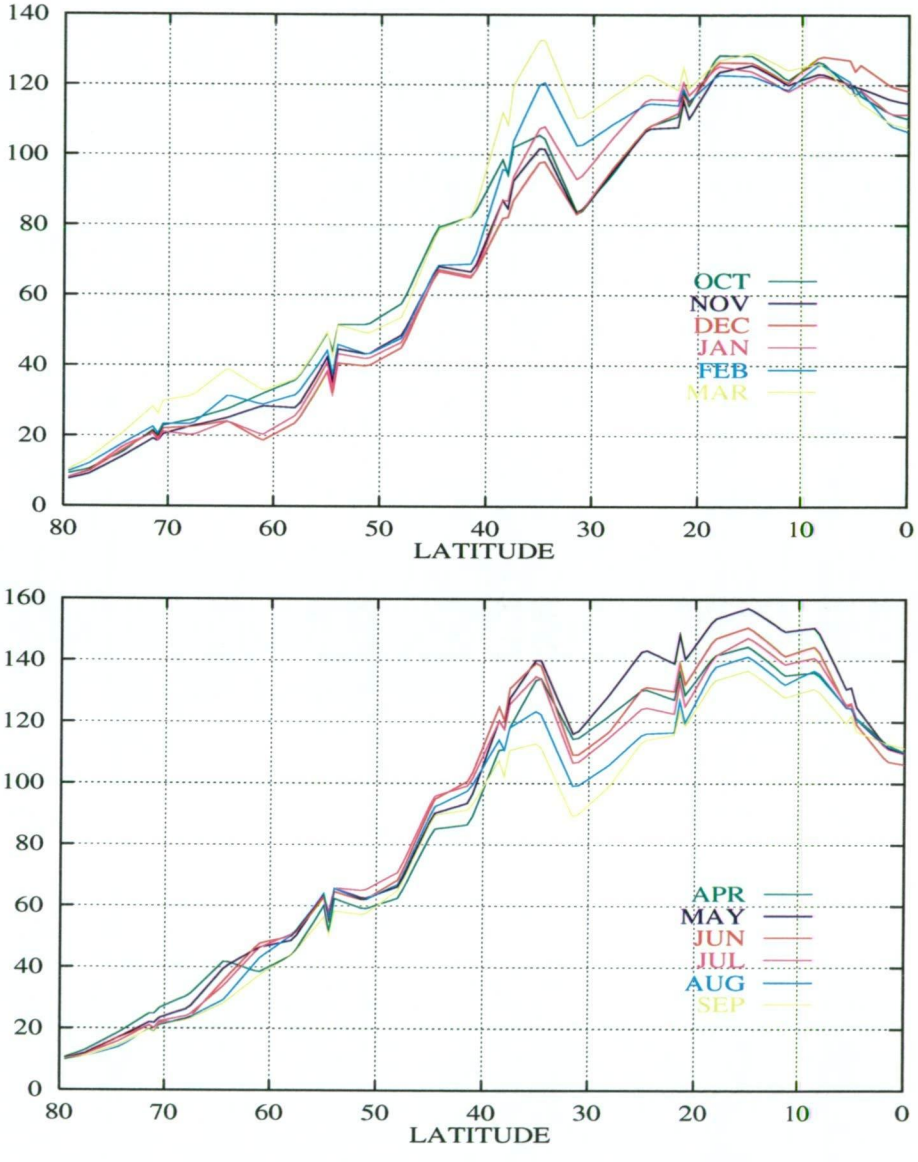

Fig. B.1: Mean monthly latent heat flux forcing (W m^{-2}) for the Southern Ocean Sector Model derived from output of the CSIRO 9 model.

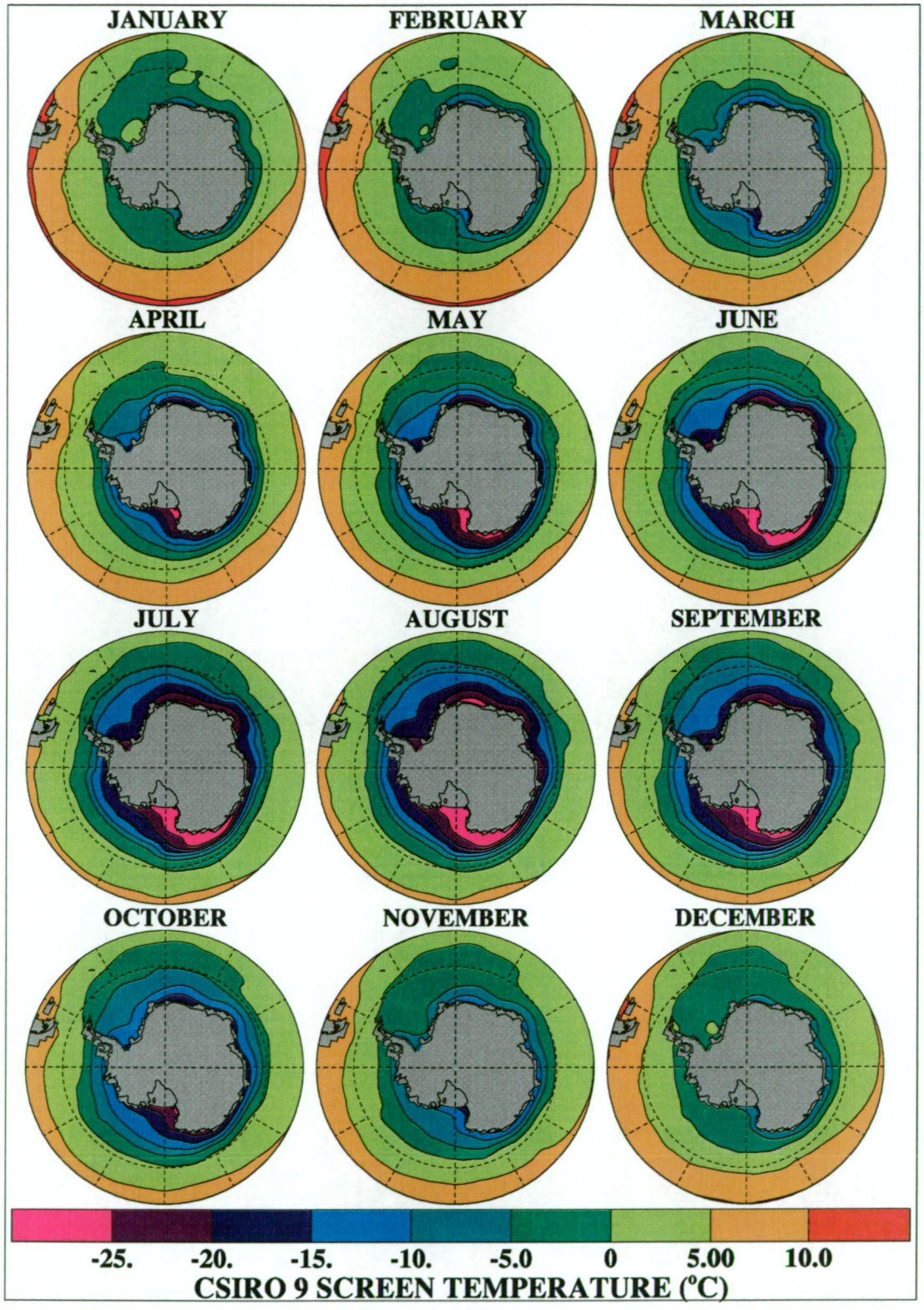

Fig. B.2: Mean monthly surface air temperature forcing (°C) for the Southern Ocean Sector Model derived from output (2 m screen temperature) of the CSIRO 9 model. Only the region south of 50°S is shown.

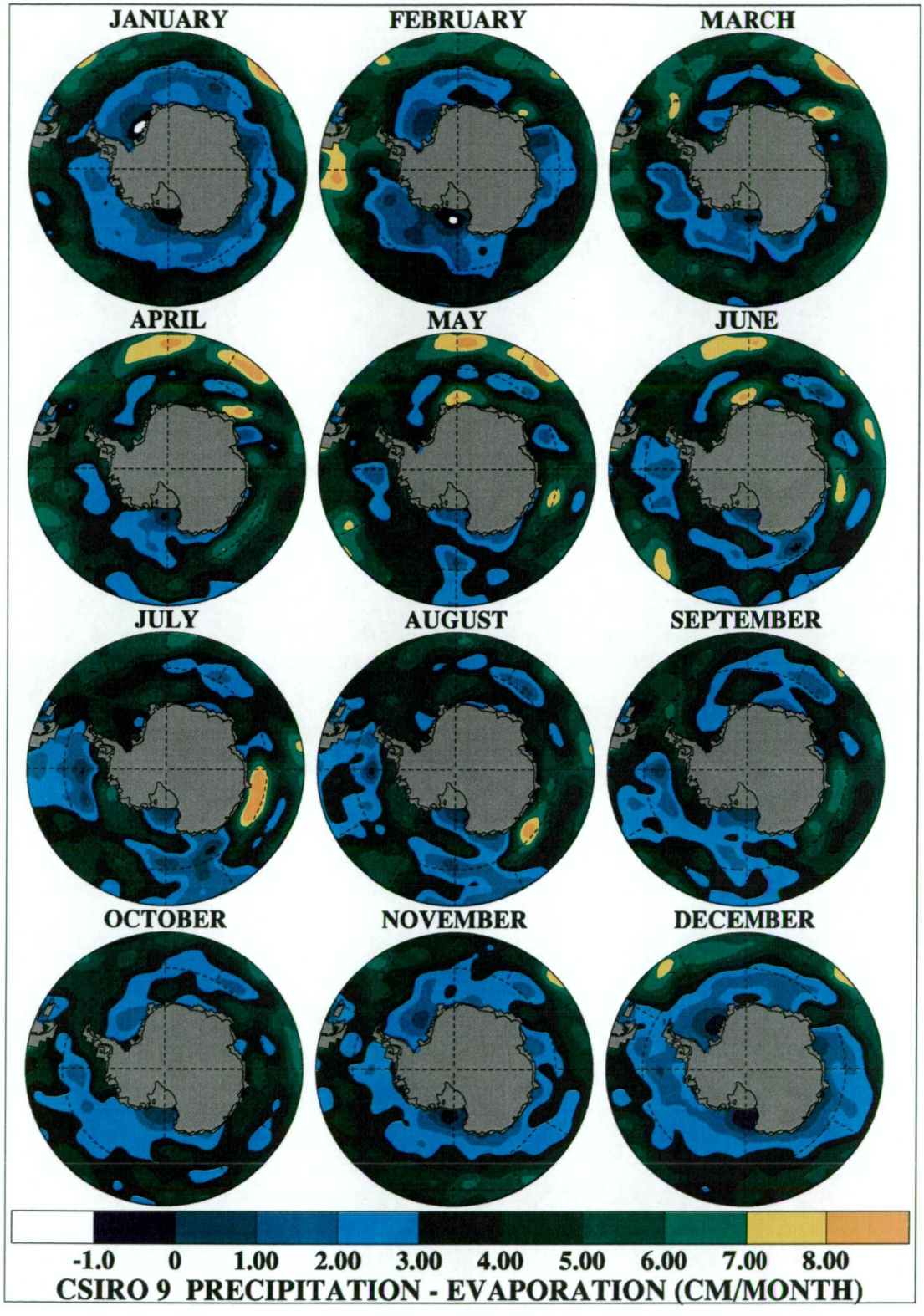

Fig. B.3: Mean monthly precipitation minus evaporation (cm month^{-1}) forcing for the Southern Ocean Sector Model derived from output of the CSIRO 9 model. Only the region south of 50°S is shown.

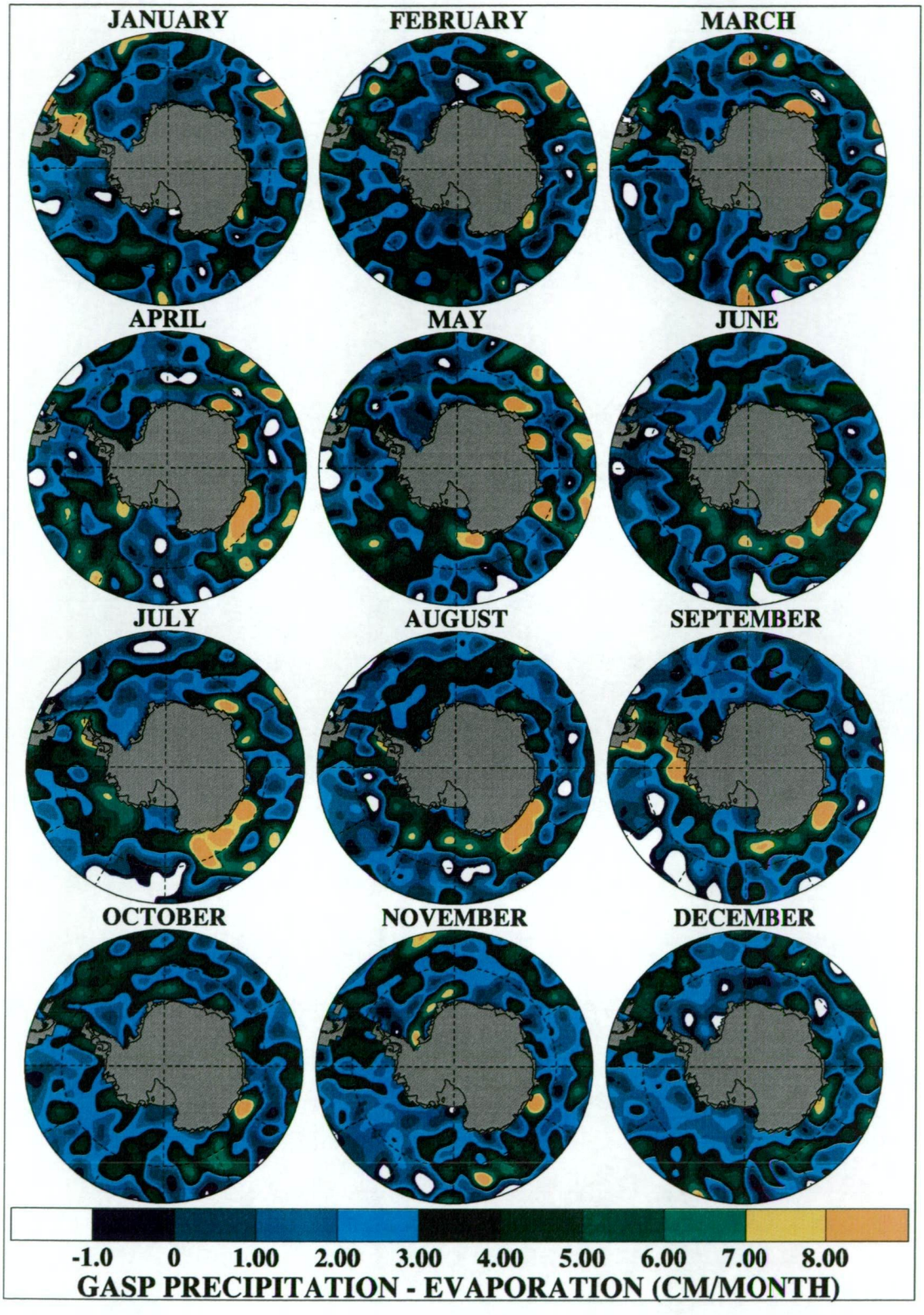

Fig. B.4: Mean monthly precipitation minus evaporation (cm month^{-1}) forcing for the Southern Ocean Sector Model derived from the GASP analyses. Only the region south of 50°S is shown.

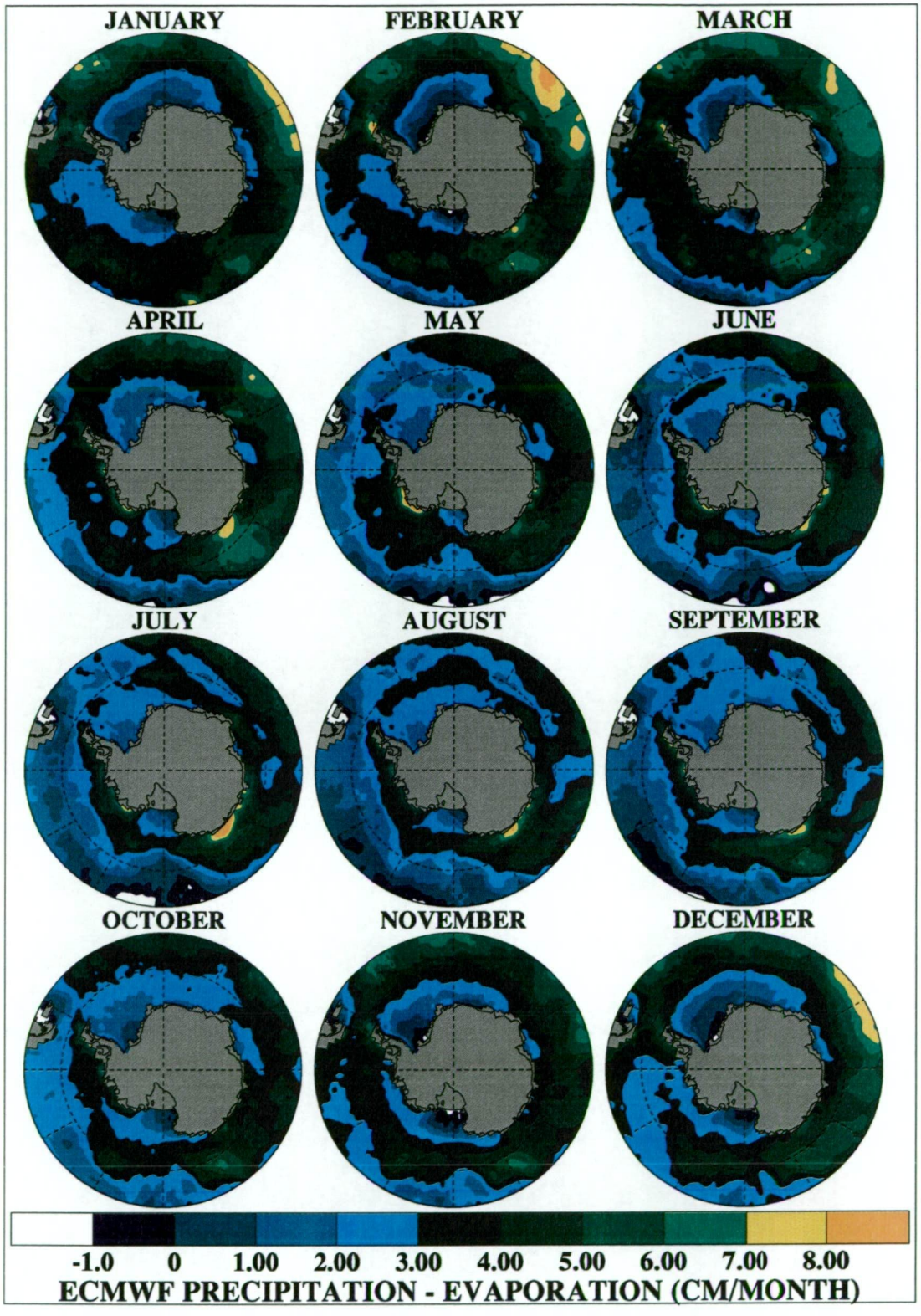

Fig. B.5: Mean monthly precipitation minus evaporation (cm month^{-1}) forcing for the Southern Ocean Sector Model derived from the ECMWF re-analysis. Only the region south of 50°S is shown.

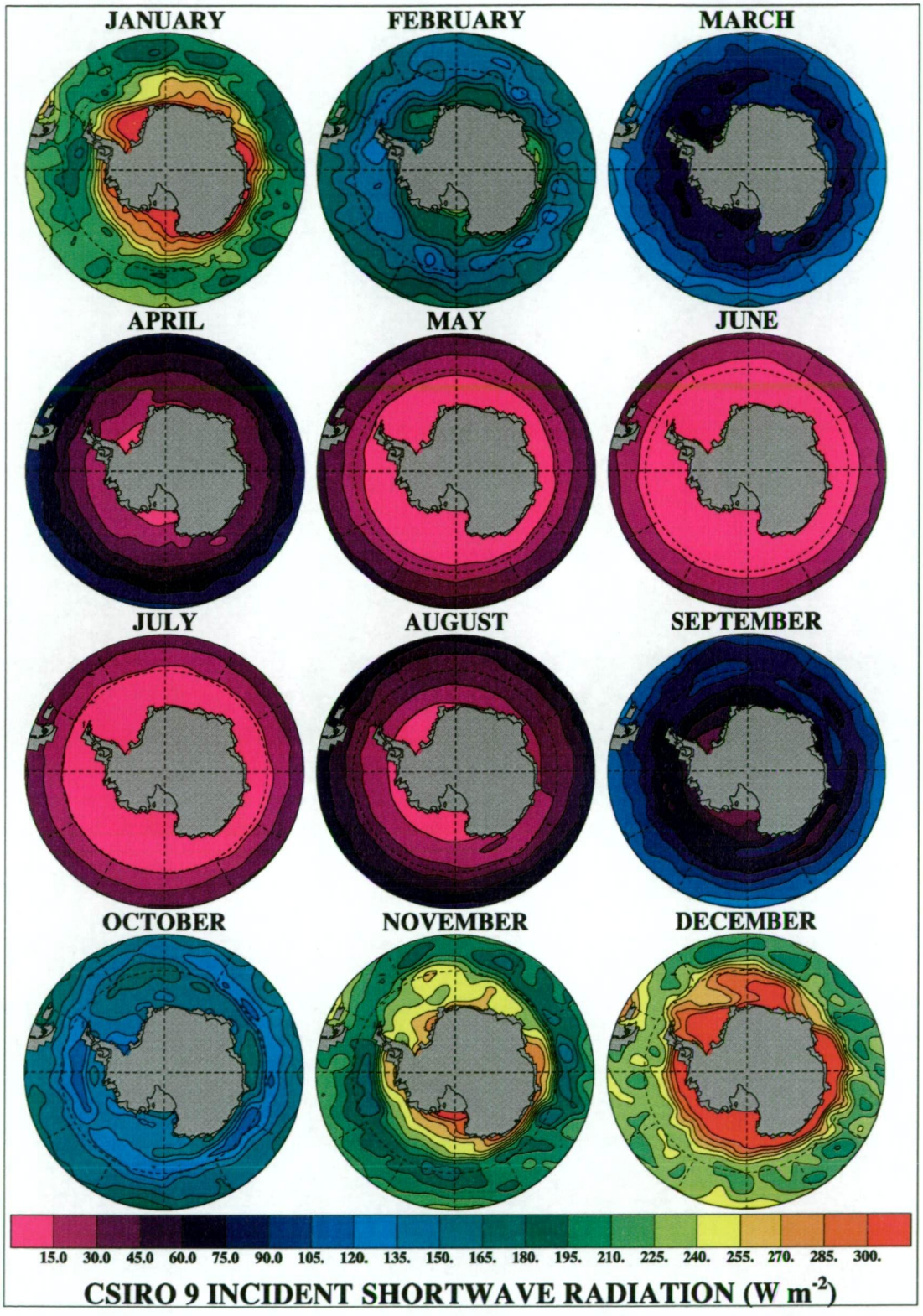

Fig. B.6: Mean monthly incident shortwave radiation (W m^{-2}) for the Southern Ocean Sector Model derived from output of the CSIRO 9 model. Only the region south of 50°S is shown. Contour interval is 15 W m^{-2}.

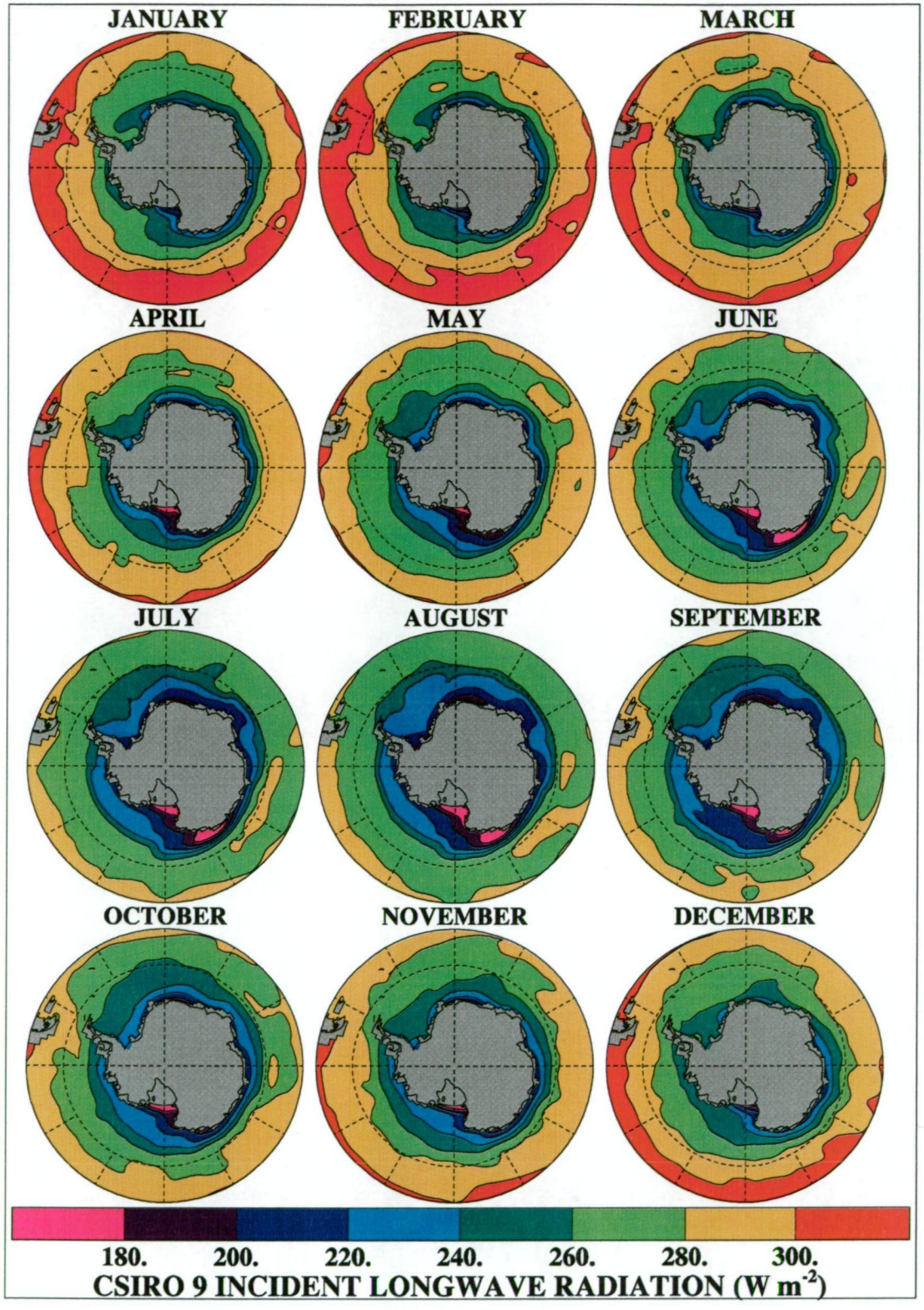

Fig. B.7: Mean monthly incident longwave radiation (W m^{-2}) for the Southern Ocean Sector Model derived from output of the CSIRO 9 model. Only the region south of 50°S is shown.

REFERENCES

Ackley, S. F., M. A. Lange and P. Wadhams, 1990. Snow cover effects on Antarctic sea ice thickness. In *Sea Ice Properties and Processes, CRREL Monogr. 90–1* (edited by S. F. Ackley and W. F. Weeks), pp. 16–21. U.S. Army Corps of Eng., Hanover, N. H.

Arakawa, A. and V. R. Lamb, 1977. Computational design of the basic dynamical processes of the UCLA general circulation model. *Meth. Comp. Physics*, **17**, 173–265.

Bindoff, N. L. and C. Wunsch, 1992. Comparison of synoptic and climatologically mapped sections in the South Pacific Ocean. *J. Climate*, **5**(6), 631–645.

Böning, C. W., R. Döscher and R. G. Budich, 1991. Seasonal transport variations in the western subtropical North Atlantic: Experiments with an eddy-resolving model. *J. Phys. Oceanogr.*, **21**, 1271–1289.

Bourke, W., T. Hart, R. Seaman, L. Rikus, P. Steinle, M. Naughton, P. Mullenmeister and G. Emberg, 1991. Operational global assimilation and prediction in the Australian Bureau of Meteorology. *BMRC Research Report*, **27**, 54–72.

Broecker, W. S., 1987. The biggest chill. *Nat. Hist. Mag.*, **97**, 74–82.

Bryan, F. O. and W. R. Holland, 1989. A high resolution simulation of the wind- and thermohaline-driven circulation in the North Atlantic Ocean. In *Parameterization of Small-Scale Processes, Proceedings of the 'Aha Huliko'a Hawaiian Winter Workshop* (edited by P. Muller and D. Henderson), pp. 99–115. University of Hawaii, Honolulu.

Bryan, K., 1969. A numerical method for the study of the circulation of the world ocean. *J. Computational Phys.*, **4**, 347–376.

Bryan, K. and M. D. Cox, 1972. The circulation of the world ocean: A numerical study. Part 1, A homogeneous model. *J. Phys. Oceanogr.*, **2**, 319–335.

Bryan, K. and L. J. Lewis, 1979. A water mass model of the world ocean. *J. Geophys. Res.*, **84**, 2503–2517.

Bryden, H. L., 1983. The Southern Ocean. In *Eddies in Marine Science* (edited by A. R. Robinson), pp. 265–277. Springer–Verlag.

Budd, W. F., 1991. Antarctica and global change. *Clim. Change*, **18**, 271–299.

Budyko, M. I., 1969. The effect of solar radiation variations on the climate of the earth. *Tellus*, **21**, 611–619.

Carmack, E. C., 1986. Circulation and mixing in ice-covered waters. In *The Geophysics of Sea Ice* (edited by N. Untersteiner), Volume 146 of *NATO ASI Series*, pp. 641–712. Plenum Press.

Carsey, F. D., 1980. Microwave observation of the Weddell Polynya. *Mon. Weather Rev.*, **108**, 2032–2044.

Cavalieri, D. J. and S. Martin, 1985. A passive microwave study of polynyas along the Antarctic Wilkes Land coast. In *Oceanology of the Antarctic Continental Shelf* (edited by S. Jacobs), Volume 43 of *Antarct. Res. Ser.*, pp. 227–252. AGU, Washington, D. C.

Colony, R. and R. S. Pritchard, 1975. Integration of elastic-plastic constitutive laws. *AIDJEX Bull.*, **30**, 55–80.

Comiso, J. and A. L. Gordon, 1987. Recurring polynyas over the Cosmonaut Sea and the Maud Rise. *J. Geophys. Res.*, **92**, 2819–2833.

Comiso, J. C., D. J. Cavalieri, C. L. Parkinson and P. Gloersen, 1997. Passive microwave algorithms for sea ice concentration: a comparison of two techniques. *Remote Sens. Environ.*, **60**, 357–384.

Coon, M. D., 1980. A review of AIDJEX modeling. In *Sea Ice Processes*

and Models: Proceedings of the Arctic Ice Dynamics Joint Experiment International Commission on Snow and Ice Symposium (edited by R. S. Pritchard), pp. 12–27. University of Washington Press, Seattle, WA.

Cox, M. D., 1970. A mathematical model of the Indian Ocean. *Deep Sea Res.*, **17**, 47–75.

Cox, M. D., 1989. An idealized model of the world ocean. Part i: The global-scale water masses. *J. Phys. Oceanogr.*, **19**, 1730–1752.

Cubasch, U., K. Hasselmann, H. Höck, E. Maier-Reimer, U. Mikolajewicz, B. D. Santer and R. Sausen, 1992. Time-dependent greenhouse warming computaions with a coupled ocean-atmosphere model. *Climate Dyn.*, **8**, 55–69.

Cubasch, U., A. Santer, A. Hellach, G. Hegerl, H. Höck, E. Maier-Reimer, U. Mikolajewicz and A. Stössel, 1994. Monte Carlo climate change forecasts with a global coupled ocean-atmosphere model. *Climate Dyn.*, **10**, 1–20.

Darby, M. S., A. J. Willmott and T. A. Somerville, 1995. On the influence of coastline orientation on the steady state width of a latent heat polynya. *J. Geophys. Res.*, **100**(C7), 13625–13633.

Deacon, G. E. R., 1937. The hydrography of the Southern Ocean. *'Discovery' Reports*, **15**, 124 pp.

Dickinson, R. E., V. Meleshko, D. Randall, E. Sarachik, P. Silva-Dias and A. Slingo, 1996. Climate processes. In *Climate change 1995. The science of climate change* (edited by J. T. Houghton, L. G. Meira Filho, B. A. Callander, N. Harris, A. Kattenberg and K. Maskell), pp. 193–227. Cambridge University Press.

Drijfhout, S., C. Heinze, M. Latif and E. Maier-Reimer, 1996. Mean circulation and internal variability in an ocean primitive equation model. *J. Phys. Oceanogr.*, **26**, 559–580.

Eicken, H., M. A. Lange, H.-W. Hubberton and P. Wadhams, 1994. Characteristics and distribution patterns of snow and meteoric ice in the

Weddell Sea and their contribution to the mass balance of sea ice. *Ann. Geophys.*, **12**, 80–93.

England, M. H., 1992. On the formation of Antarctic intermediate and bottom water in ocean general circulation models. *J. Phys. Oceanogr.*, **22**, 918–926.

England, M. H., 1993. Representing the global-scale water masses in ocean general circulation models. *J. Phys. Oceanogr.*, **23**, 1523–1552.

ERA, 1997. ECMWF Re-Analysis, Project Report Series, 1. ERA Description. Technical report. J. K. Gibson, P. Kallberg, S. Uppala, A. Hernandez, A. Nomura, E. Serrano.

Fichefet, T. and P. Gasper, 1988. A model study of upper ocean-sea ice interaction. *J. Phys. Oceanogr.*, **18**, 181–195.

Fichefet, T. and M. A. Morales Maqueda, 1997a. Modelling the influence of snow accumulation and snow-ice formation on the seasonal cycle of the Antarctic sea-ice cover. *subm. to Climate Dyn.*

Fichefet, T. and M. A. Morales Maqueda, 1997b. Sensitivity of a global sea ice model to the treatment of ice thermodynamics and dynamics. *J. Geophys. Res.*, **102**(C6), 12609–12646.

Flato, G. M. and W. D. Hibler, 1992. Modeling pack ice as a cavitating fluid. *J. Phys. Oceanogr.*, **22**, 626–651.

FRAM, 1991. An eddy-resolving model of the Southern Ocean. *EOS*, **72**(15), 169 and 174–175.

Gates, W. L., A. Henderson-Sellers, G. J. Boer, C. K. Folland, A. Kitoh, B. J. McAvaney, F. Semazzi, N. Smith, A. J. Weaver and Q.-C. Zeng, 1996. Climate models – evaluation. In *Climate change 1995. The science of climate change* (edited by J. T. Houghton, L. G. Meira Filho, B. A. Callander, N. Harris, A. Kattenberg and K. Maskell), pp. 229–284. Cambridge University Press.

Gill, A. E., 1973. Circulation and bottom water production in the Weddell Sea. *Deep Sea Res.*, **20**, 111–140.

Gill, A. E. and K. Bryan, 1971. Effects of geometry on the circulation of a three-dimensional southern-hemisphere ocean model. *Deep Sea Res.*, **18**, 685–721.

Gloerson, P., W. J. Campbell, D. J. Cavalieri, J. C. Comiso, C. L. Parkinson and H. J. Zwally, 1992. Arctic and Antarctic sea ice, 1978–1987: Satellite passive-microwave observations and analysis. Special Publication SP–511, NASA, Washington, DC. 290 pp.

Goosse, H., J. M. Campin, T. Fichefet and E. Deleersnijder, 1997. The impact of sea-ice formation on the properties of Antarctic bottom water. *Annals of Glaciol.*, **25**, 276–281.

Gordon, A. L., 1978. Deep Antarctic convection west of Maud Rise. *J. Phys. Oceanogr.*, **8**, 600–612.

Gordon, A. L., 1981. Seasonality of Southern Ocean sea ice. *J. Geophys. Res.*, **86**(C5), 4193–4197.

Gordon, A. L., 1986. Interocean exchange of thermocline water. *J. Geophys. Res.*, **91**, 5037–5046.

Gordon, A. L., 1988. The Southern Ocean and global climate. *Oceanus*, **31**(2), 39–46.

Gordon, A. L., 1991. Two stable modes of Southern Ocean winter stratification. In *Deep Convection and Deep Water Formation in the Oceans* (edited by Chu and Gascard), pp. 17–35. Elsevier Science Publishers.

Gordon, A. L., 1998. Are we ready for a full Southern Ocean extended climate study? In *U. S. WOCE Implementation Report Number 10*, pp. 48–49. WOCE Office, College Station, TX.

Gordon, A. L. and J. C. Comiso, 1988. Polynyas in the Southern Ocean. *Scientific American*, **256**, 90–97.

Gordon, A. L. and B. A. Huber, 1984. Thermohaline stratification below the Southern Ocean sea ice. *J. Geophys. Res.*, **89**(C1), 641–648.

Gordon, A. L. and B. A. Huber, 1990. Southern Ocean winter mixed layer. *J. Geophys. Res.*, **95**(C7), 11655–11672.

Gordon, H. B. and S. P. O'Farrell, 1997. Transient climate change in the CSIRO coupled model with dynamic sea ice. *Mon. Weather Rev.*, **125**, 875–907.

Häkkinen, S., 1987. A constitutive law for sea-ice and some applications. *Math. Modell.*, **9**, 9469–9478.

Häkkinen, S., 1995. Seasonal simulation of the Southern Ocean coupled ice-ocean system. *J. Geophys. Res.*, **100**(C11), 22733–22748.

Häkkinen, S. and G. L. Mellor, 1992. Modeling the seasonal variability of a coupled Arctic ice-ocean system. *J. Geophys. Res.*, **97**, 20285–20304.

Hasselmann, K., 1982. An ocean model for climate variability studies. *Prog. Oceanogr.*, **11**, 69–92.

Hasselmann, K., L. Bengtsson, U. Cubasch, G. C. Hegerl, H. Rodhe, E. Roeckner, H. von Storch, R. Voss and J. Waszkewitz, 1995. Detection of anthropogenic climate change using a fingerprint method. Technical Report 168, Max-Planck Institute for Meteorology.

Hasselmann, K., R. Sausen, E. Maier-Reimer and R. Voss, 1993. On the cold start problem in transient simulations with coupled ocean-atmosphere models. *Climate Dyn.*, **9**, 53–61.

Heil, P., I. Allison and V. I. Lytle, 1996. Seasonal and interannual variations of the oceanic heat flux under a landfast Antarctic sea ice cover. *J. Geophys. Res.*, **101**(C11), 25741–25752.

Hellerman, S. and M. Rosenstein, 1983. Normal monthly wind stress over the world ocean with error estimates. *J. Phys. Oceanogr.*, **13**, 1093–1104.

Hibler, W. D., 1979. A dynamic thermodynamic sea ice model. *J. Phys. Oceanogr.*, **9**, 815–846.

Hibler, W. D. and S. F. Ackley, 1983. Numerical simulation of the Weddell Sea pack ice. *J. Geophys. Res.*, **88**(C5), 2873–2887.

Hibler, W. D. and K. Bryan, 1987. A diagnostic ice-ocean model. *J. Phys. Oceanogr.*, **17**, 987–1015.

Hibler, W. D. and G. M. Flato, 1992. Sea ice models. In *Climate system*

modelling (edited by K. E. Trenberth), pp. 413–436. Cambridge Uni. Press.

Hirst, A. C., 1999. The Southern Ocean response to global warming in the CSIRO coupled ocean-atmosphere model. *Environmental Modelling and Software (Special Issue on Global Climate Change)*, **14**, 227–241.

Hirst, A. C., S. P. O'Farrell and H. B. Gordon, 1999. Comparison of a coupled ocean–atmosphere model with and without oceanic eddy-induced advection. 1. Ocean spin up and control integrations. *J. Clim., in press.*

Holland, W. R., 1978. The role of mesoscale eddies in the general circulation of the ocean – Numerical experiments using a wind-driven quasi-geostrophic model. *J. Phys. Oceanogr.*, **8**, 363–392.

Holland, W. R. and A. D. Hirschman, 1972. A numerical calculation of the circulation in the North Atlantic Ocean. *J. Phys. Oceanogr.*, **2**, 336–354.

Holland, W. R. and L. B. Lin, 1975a. On the generation of mesoscale eddies and their contribution to the oceanic general circulation. I. A preliminary numerical experiment. *J. Phys. Oceanogr.*, **5**, 642–657.

Holland, W. R. and L. B. Lin, 1975b. On the generation of mesoscale eddies and their contribution to the oceanic general circulation. II. A parameter study. *J. Phys. Oceanogr.*, **5**, 658–669.

Ip, C. F., W. D. Hibler and G. M. Flato, 1991. On the effect of rheology on seasonal sea-ice simulations. *Annals of Glaciol.*, **15**, 17–25.

IPCC, 1996. *Climate change 1995. The science of climate change.* Cambridge University Press, Cambridge, U.K. Houghton, J. T., Meira Filho, L. G., Callander, B. A., Harris, N., Kattenberg, A. and Maskell, K. (eds.), 572 pp.

Jaeger, L., 1976. Monatskarten des Niederschlags für die ganze Erde. Technical Report 139, Ber Deutsch Wetterdienstes.

Killworth, P. D., 1979. On 'chimney' formations in the ocean. *J. Phys. Oceanogr.*, **9**, 531–554.

Killworth, P. D., 1983. Deep convection in the world ocean. *Rev. Geophys.*

Spac. Phys., **21**(1), 1–26.

Ledley, T. S., 1991. Snow on sea ice: Competing effects in shaping climate. *J. Geophys. Res.*, **96**, 17195–17208.

Ledley, T. S., 1993. Variations in snow on sea ice: A mechanism for producing climate variations. *J. Geophys. Res.*, **98**, 10401–10410.

Legates, D. R. and C. J. Willmott, 1990. Mean seasonal and spatial variability in gauge-corrected, global precipitation. *Int. J. Climatol.*, **10**, 111–127.

Legutke, S., E. Maier-Reimer, A. Stössel and A. Hellbach, 1997. Ocean-sea-ice coupling in a global ocean general circulation model. *Annals of Glaciol.*, **25**, 116–120.

Lemke, P., 1987. A coupled one-dimensional sea ice-ocean model. *J. Geophys. Res.*, **92**(C6), 13164–13172.

Lemke, P. and T. O. Manley, 1984. The seasonal variation of the mixed layer and the pycnocline under polar sea ice. *J. Geophys. Res.*, **89**(C4), 6494–6504.

Lemke, P., W. B. Owens and W. D. Hibler, 1990. A coupled sea ice-mixed layer-pycnocline model for the Weddell Sea. *J. Geophys. Res.*, **95**(C6), 9513–9525.

Levitus, S., T. P. Boyer and J. Atonov, 1994a. *World Ocean Atlas 1994, Volume 4: Temperature*. NOAA Atlas NESDIS 4. 129 pp.

Levitus, S., R. Burgett and T. P. Boyer, 1994b. *World Ocean Atlas 1994, Volume 3: Salinity*. NOAA Atlas NESDIS 3. 111 pp.

Lunkeit, F., R. Sausen and J. M. Oberhuber, 1996. Climate simulations with the global coupled atmosphere-ocean model ECHAM2/OPYC, I, Present-day climate and ENSO events. *Clim. Dyn.*, **12**, 195–212.

Lytle, V. I. and S. F. Ackley, 1996. Heat flux through sea ice in the western Weddell Sea: Convective and conductive transfer processes. *J. Geophys. Res.*, **101**(C4), 8853–8868.

Lytle, V. I., R. Massom, N. Bindoff, A. Worby and I. Allison, 1999. The

wintertime heat flux to the underside of East Antarctic pack ice. *J. Geophys. Res., in press.*

Maier-Reimer, E., U. Mikolajewicz and K. Hasselmann, 1993. Mean circulation of the Hamburg LSG OGCM and its sensitivity to the thermohaline surface forcing. *J. Phys. Oceanogr.*, **23**, 731–757.

Manabe, S., M. J. Spelman and R. J. Stouffer, 1992. Transient responses of a coupled ocean-atmosphere model to gradual changes of atmospheric CO_2. Part II: Seasonal response. *J. Climate*, **5**, 105–126.

Manabe, S. and R. J. Stouffer, 1980. Sensitivity of a global climate model to an increase in CO_2 concentration in the atmosphere. *J. Geophys. Res.*, **85**(C10), 5529–5554.

Manabe, S. and R. J. Stouffer, 1994. Multiple-century response of a coupled ocean-atmosphere model to an increase of atmospheric carbon dioxide. *J. Climate*, **7**, 5–23.

Markus, T., C. Kottmeier and E. Fahrbach, 1998. Ice formation in coastal polynyas in the Weddell Sea and their impact on oceanic salinity. In *Antarctic sea ice: Physical processes, interactions and variability* (edited by M. O. Jeffries), Volume 74 of *Antarct. Res. Ser.*, pp. 273–292. AGU, Washington D.C.

Marsland, S. and J.-O. Wolff, 1998. East antarctic seasonal sea-ice and ocean stability: A model study. *Annals of Glaciol.*, **27**, 477–482.

Martinson, D. G., 1990. Evolution of the Southern Ocean winter mixed layer and sea ice: Open ocean deepwater formation and ventilation. *J. Geophys. Res.*, **95**(C7), 11641–11654.

Martinson, D. G., 1993. Ocean heat and seasonal sea ice thickness in the Southern Ocean. In *Ice in the Climate System* (edited by W. R. Peltier), Volume 1(12) of *NATO ASI Series*, pp. 597–609. Springer–Verlag, Berlin.

Martinson, D. G. and R. A. Iannuzzi, 1998. Antarctic ocean-ice interaction: Implications from ocean bulk property distributions. In *Antarctic sea ice:*

Physical processes, interactions and variability (edited by M. O. Jeffries), Volume 74 of *Antarct. Res. Ser.*, pp. 243–272. AGU, Washington D.C.

Martinson, D. G., P. D. Killworth and A. L. Gordon, 1981. A convective model for the Weddell Polynya. *J. Phys. Oceanogr.*, **11**, 466–488.

Massom, R. A., M. R. Drinkwater and C. Haas, 1997. Winter snow cover on sea ice in the Weddell Sea. *J. Geophys. Res.*, **102(C1)**, 1101–1117.

Maykut, G., 1986. The surface heat and mass balance. In *The Geophysics of Sea Ice* (edited by N. Untersteiner), Volume 146 of *NATO ASI Series*, pp. 395–463. Plenum Press.

Maykut, G. A., A. S. Thorndike and N. Untersteiner, 1972. AIDJEX scientific plan. *AIDJEX Bulletin*, **15**, 1–67.

Maykut, G. A. and N. Untersteiner, 1971. Some results from a time-dependent thermodynamic model of sea ice. *J. Geophys. Res.*, **76**, 1550–1575.

McGregor, J. L., H. B. Gordon, I. G. Watterson, M. R. Dix and L. D. Rotstayn, 1993. The CSIRO 9-level atmospheric general circulation model. Technical Report 26, CSIRO, Division of Atmospheric Research, Melbourne, Australia.

McPhee, M. G., S. F. Ackley, P. Guest, B. A. Huber, D. G. Martinson, J. H. Morison, R. D. Muench, L. Padman and T. P. Stanton, 1996. The Antarctic Zone Flux Experiment. *Bull. Amer. Met. Soc.*, **77**, 1221–1232.

McWilliams, J. C. and J. H. S. Chow, 1981. Equilibrium geostrophic turbulence. I: A reference solution in a β-plane channel. *J. Phys. Oceanogr.*, **11**, 921–949.

McWilliams, J. C., W. R. Holland and J. H. S. Chow, 1978. A description of numerical Antarctic Circumpolar Currents. *Dyn. Atmos. Oceans*, **2**, 213–291.

Meehl, G. A. and W. M. Washington, 1990. CO_2 climate sensitivity and snow-sea ice albedo parameterisation in an atmospheric GCM coupled to a mixed layer ocean model. *Clim. Change*, **6**, 283–306.

Meehl, G. A., W. M. Washington and A. J. Semtner, 1982. Experiments with a global ocean model driven by observed atmospheric forcing. *J. Phys. Oceanogr.*, **12**, 301–312.

Mellor, G. L. and L. H. Kantha, 1989. An ice-ocean coupled model. *J. Geophys. Res.*, **94**, 10937–10954.

Mikolajewicz, U. and E. Maier-Reimer, 1990. Internal secular variability in an ocean general circulation model. *Climate Dyn.*, **4**, 145–156.

Motoi, T., N. Ono and M. Wakatsuchi, 1987. A mechanism for the formation of the Weddell Polynya in 1974. *J. Phys. Oceanogr.*, **17**, 2241–2247.

NOAA, 1988. *Data Announcement 88-MGG-02, Digital relief of the Surface of the Earth.* NOAA, National Geophysical Data Center, Boulder, Colorado.

Oberhuber, J. M., 1993a. The OPYC ocean general circulation model. Technical Report 7, German Climate Computer Center (DKRZ).

Oberhuber, J. M., 1993b. Simulation of the Atlantic circulation with a coupled sea ice-mixed layer-isopycnal general circulation model, I, Model description. *J. Phys. Oceanogr.*, **23**, 808–829.

Olbers, D., 1993. Links of the Southern Ocean to the global climate. Berichte aus dem Fachbereich Physik 39, AWI fuer Polar und Meeresforschung.

Owens, W. B. and P. Lemke, 1990. Sensitivity studies with a sea ice-mixed layer-pycnocline model in the Weddell Sea. *J. Geophys. Res.*, **95**(C6), 9527–9538.

Parkinson, C. L., 1983. On the development and cause of the Weddell Polynya in a sea ice simulation. *J. Phys. Oceanogr.*, **13**, 501–511.

Parkinson, C. L. and W. M. Washington, 1979. A large scale numerical model of sea ice. *J. Geophys. Res.*, **84**(C1), 311–337.

Pease, C. H., 1987. The size of wind-driven coastal polynyas. *J. Geophys. Res.*, **92**, 7049–7059.

Press, W. H., B. P. Flannery, S. A. Teukolsky and W. T. Vetterling, 1988.

Numerical Recipes in C. The Art of Scientific Computing. Cambridge University Press.

Pritchard, R. S., 1975. An elastic-plastic constitutive law for sea ice. *J. Appl. Mech.*, **42E**, 379–384.

Rind, D., R. Healy, C. Parkinson and D. Martinson, 1995. The role of sea ice in $2XCO_2$ climate model sensitivity. Part I: The total influence of sea ice thickness and extent. *Amer. Meteorol. Soc.*, pp. 1–15.

Rintoul, S. R., 1998. On the origin and influence of Adélie Land Bottom Water. In *Ocean, Ice and Atmosphere. Interactions at the Antarctic Continental Margin* (edited by S. S. Jacobs and R. F. Weiss), Volume 75 of *Antarct. Res. Ser.*, pp. 151–171. AGU, Washington D.C.

Robinson, A. R., D. E. Harrison, Y. Mintz and A. J. Semtner, 1977. Eddies and the general circulation of an idealized oceanic gyre: A wind and thermally driven primitive equation numerical experiment. *J. Phys. Oceanogr.*, **7**, 182–207.

Santer, B. D., W. Brüggemann, U. Cubasch, K. Hasselmann, E. Maier-Reimer and U. Mikolajewicz, 1994. Signal to noise analysis of time dependent greenhouse warming experiments, Part 1: Pattern analysis. *Climate Dyn.*, **9**, 267–285.

Sellers, W. D., 1969. A global climatic model based on the energy balance of the earth-atmosphere system. *J. Appl. Meteorol.*, **8**, 392–400.

Semtner, A. J., 1974. An oceanic general circulation model with bottom topography. Numerical simulation of weather and climate. Technical report, Department of Meteorology, University of California, Los Angeles.

Semtner, A. J., 1976a. A model for the thermodynamic growth of sea ice in numerical investigations of climate. *J. Phys. Oceanogr.*, **6**, 379–389.

Semtner, A. J., 1976b. A numerical simulation of the Arctic Ocean circulation. *J. Phys. Oceanogr.*, **6**, 409–425.

Semtner, A. J., 1984. On modelling the seasonal thermodynamic cycle of sea ice in studies of climatic change. *Clim. Change*, **6**, 27–37.

Semtner, A. J., 1987. A numerical study of sea ice and ocean circulation in the Arctic. *J. Phys. Oceanogr.*, **17**, 1077–1099.

Semtner, A. J., 1994. Sixth-degree global ocean model. U.S. WOCE Report 1994, U.S. WOCE Office, Texas A&M University, College Station, TX. 34–36.

Semtner, A. J. and R. M. Chervin, 1988. A simulation of the global ocean circulation with resolved eddies. *J. Geophys. Res.*, **93**(C12), 15502–15522.

Semtner, A. J. and R. M. Chervin, 1989. Breakthroughs in ocean and climate modelling made possible by supercomputers of today and tomorrow. In *Supercomputing 88: Volume II Science and Applications* (edited by J. L. Martin and S. F. Lundstrom), pp. 230–239. IEEE Computer Society Press.

Semtner, A. J. and R. M. Chervin, 1992. Ocean general circulation from a global eddy-resolving model. *J. Geophys. Res.*, **97**(C4), 5493–5550.

Semtner, A. J. and Y. Mintz, 1977. Numerical simulation of the Gulf Stream and mid-ocean eddies. *J. Phys. Oceanogr.*, **7**, 208–230.

Stössel, A., 1992. The Hamburg sea-ice model. Technical Report 3, German Climate Computer Center (DKRZ).

Stössel, A., 1997. On the impact of sea ice in a global ocean circulation model. *Annals of Glaciol.*, **25**, 111–115.

Stössel, A., S.-J. Kim and S. S. Drijfhout, 1998. The impact of Southern Ocean sea ice in a global ocean model. *J. Phys. Oceanogr.*, **28**, 1999–2018.

Stössel, A., P. Lemke and W. B. Owens, 1990. Coupled sea ice-mixed layer simulations for the Southern Ocean. *J. Geophys. Res.*, **95**(C6), 9539–9555.

Thorndike, A. S. and R. Colony, 1982. Sea ice motion in response to geostrophic winds. *J. Geophys. Res.*, **87**(C8), 5845–5852.

UNESCO, 1981. Tenth report of the joint panel on oceanographic tables

and standards. UNESCO Technical Papers in Marine Sci. 36, UNESCO, Paris.

Untersteiner, N., 1980. AIDJEX review. In *Sea Ice Processes and Models:Proceedings of the Arctic Ice Dynamics Joint Experiment International Commission on Snow and Ice Symposium* (edited by R. S. Pritchard), pp. 3–11. University of Washington Press, Seattle, WA.

van Ypersele, J.-P., 1990. Modelling sea ice for climate studies. In *Climate-Ocean Interaction* (edited by M. E. Schlesinger), pp. 97–123. Kluwer Academic Publishers.

Veronis, G., 1966a. Wind-driven ocean circulation–Part 1. linear theory and perturbation analysis. *Deep Sea Res.*, **13**, 17–29.

Veronis, G., 1966b. Wind-driven ocean circulation–Part 2. numerical solutions of the non-linear problem. *Deep Sea Res.*, **13**, 31–55.

Washington, W. M., A. J. Semtner, G. A. Meehl, D. J. Knight and T. A. Mayer, 1980. General circulation experiment with a coupled atmosphere, ocean and sea ice model. *J. Phys. Oceanogr.*, **10**, 1887–1908.

Washington, W. M., A. J. Semtner, C. Parkinson and L. Morrison, 1976. On the development of a seasonal change sea-ice model. *J. Phys. Oceanogr.*, **6**, 679–685.

Weatherly, J. W. and J. E. Walsh, 1996. The effects of precipitation and river runoff in a coupled ice-ocean model of the Arctic. *Clim. Dyn.*, **12**, 785–798.

Webb, D. J., B. A. de Cuevas and A. C. Coward, 1998. The first main run of the OCCAM global ocean model. Internal Document 34, Southampton Oceanography Centre.

Whitworth, T. and R. G. Peterson, 1985. Volume transport of the Antarctic Circumpolar Current from bottom pressure measurements. *J. Phys. Oceanogr.*, **15**, 810–816.

Wolff, J.-O., 1994. Ocean modelling efforts in the global climate system. *Aust. Met. Mag.*, **43**, 263–281.

Wolff, J.-O., 1999. Antarctic sea-ice simulations with a coupled ocean/sea-ice model on a telescoped grid. *Annals of Glaciol.*, **27**, in press.

Wolff, J.-O., E. Maier-Reimer and S. Legutke, 1997. The Hamburg Ocean Primitive Equation Model HOPE. Technical Report 13, German Climate Computer Center (DKRZ).

Wolff, J.-O., E. Maier-Reimer and D. J. Olbers, 1991. Wind-driven flow over topography in a zonal β–plane channel: A quasi-geostrophic model of the Antarctic Circumpolar Current. *J. Phys. Oceanogr.*, **21**, 236–264.

Worby, A. P., R. A. Massom, I. Allison, V. I. Lytle and P. Heil, 1998. East Antarctic sea ice: A review of its structure, properties, and drift. In *Antarctic sea ice: Physical processes, interactions and variability* (edited by M. O. Jeffries), Volume 74 of *Antarct. Res. Ser.*, pp. 41–68. AGU, Washington D.C.

Worby, A. P. and X. Wu, 1998. East Antarctic sea ice: observations and modelling. *Annals of Glaciol.*, **27**, 427–432.

Wu, X., W. F. Budd, A. P. Worby and I. Allison, 1998. Sensitivity of the Antarctic sea ice distribution to oceanic heat flux in a coupled atmosphere-sea ice model. *subm. to J. Geophys. Res.*

Wu, X., I. Simmonds and W. F. Budd, 1996. Southern hemisphere climate system recovery from 'instantaneous' sea-ice removal. *Q. J. R. Meteorol. Soc.*, **122**, 1501–1520.

Wu, X., I. Simmonds and W. F. Budd, 1997. Modeling of Antarctic sea ice in a general circulation model. *Journal of Climate*, **10**(4), 593–609.

Zwally, H. J., J. C. Comiso and A. L. Gordon, 1985. Antarctic offshore leads and polynyas and oceanographic effects. In *Oceanology of the Antarctic Continental Shelf* (edited by S. Jacobs), Volume 43 of *Antarct. Res. Ser.*, pp. 203–226. AGU, Washington, D. C.

Zwally, H. J., J. C. Comiso, C. L. Parkinson, W. J. Campbell, F. D. Carsey and P. Gloerson, 1983. Antarctic sea-ice cover 1973–1976: Satellite passive-micro-wave observations. Special Publication SP–459, NASA,

Washington, DC. 206 pp.

Zwally, H. J., C. Parkinson, F. Carsey, P. Gloerson, W. J. Campbell and R. O. Ramseier, 1979. Antarctic sea ice variations 1973–1975. NASA Weather Climate Review, Pap. 56, NASA, Washington, DC. 335–340.